Tampere University

NICOLE ANDERTON

Radial Dynamics of Pickering-stabilised Endoskeletal Antibubbles and Their Components in Pulsed Ultrasound

Tampere University Dissertations 907

Tampere University Dissertations 907

NICOLE ANDERTON

Radial Dynamics of Pickering-stabilised Endoskeletal Antibubbles and Their Components in Pulsed Ultrasound

ACADEMIC DISSERTATION
To be presented, with the permission of
the Faculty of Medicine and Health Technology
of Tampere University,
for public discussion in the auditorium A1
of the Main building, Kalevantie 4, Tampere,
on 1 February 2024, at 12 o'clock.

ACADEMIC DISSERTATION
Tampere University, Faculty of Medicine and Health Technology
Finland

Responsible supervisor and Custos	Professor Michiel Postema Tampere University Finland	
Pre-examiners	Professor Benoit Scheid Université Libre de Bruxelles Belgium	Professor Steven Wrenn Virginia Tech United States of America
Opponent	Professor Paul Campbell University of Dundee Scotland	

Cover design: Roihu Inc.

ISBN 978-952-03-3163-4 (print)
ISBN 978-952-03-3164-1 (pdf)
ISSN 2489-9860 (print)
ISSN 2490-0028 (pdf)
http://urn.fi/URN:ISBN:978-952-03-3164-1

Carbon dioxide emissions from printing Tampere University dissertations have been compensated.

PunaMusta Oy – Yliopistopaino
Joensuu 2023

ACKNOWLEDGEMENTS

I'd like to express my immense gratitude to my supervisor, Prof. Michiel Postema. It goes without saying that I wouldn't have produced this body of work without your supervision. Perhaps more importantly though, your guidance and belief in my potential has afforded me numerous opportunities and experiences during my doctoral journey that have greatly enriched both my academic and personal growth.

I would like to express my deepest appreciation to Prof. Nobuki Kudo for hosting my stay at his high-speed imaging facility at Hokkaido University. The experiments were done together with Mr Ryunosuke Matsumoto, Mr Ri-ichiro Shimizu, Miss Hu Xinyue, Miss Momoka Yamasaku, and Mr Naoyuki Otake, for which I am most grateful.

Special thanks are given to Dr Albert T. Poortinga from Eindhoven University of Technology for manufacturing and supplying the antibubble samples used in this research. Your input, particularly in the explosive antibubble study, was crucial to the success of this research.

Scanning electron microscopy images were captured at the facilities of Prof. Rustem Uzbekov at the University of Tours with funding of Dr Ayache Bouakaz and Prof. Michiel Postema.

I would like to express my deepest gratitude to all coauthors, especially to Prof. David M. Rubin and Prof. Vered Aharonson for their didactic skills in the writing process.

I'd also like to recognise my follow-up group members, Prof. Jari Hyttinen and Dr Kerstin Lenk, for their vital insight and support throughout my doctoral studies.

Of course, this endeavour would not be possible without the Faculty of Medicine and Health Technology steering group, pre-examiners, and opponent. Your readiness to set aside your valuable time to critique my work is greatly appreciated.

I'm extremely thankful to Dr Craig S. Carlson for acting as my sounding board throughout this process. Your support, insight and readiness to listen, not to men-

tion proofread, has been invaluable in my writing process and confidence. Thank you to Dr Anna Sendra too, for lending her support and employing her commendable spelling-mistake-finding talents.

Finally, a heartfelt acknowledgement to my parents, Janet and Steve Smith. You have fiercely supported me through it all, and worked incredibly hard to ensure that I would one day have opportunities such as this doctoral journey. I am so deeply grateful.

The work presented in this dissertation is based on research supported in part by JSPS KAKENHI, Grant Numbers JP17H00864 and JP20H04542, by the National Research Foundation of South Africa, Grant Number 127102, and by the Academy of Finland, Grant Number 340026. Additionally, the work was supported by fixed-term doctoral student positions awarded by the Dean of the Faculty of Medicine and Health Technology at Tampere University.

ABSTRACT

Liquids containing microscopic antibubbles may have theranostic applications in harmonic diagnostic ultrasonic imaging and in ultrasound-assisted drug delivery. Presently there are no known agents available with the acoustic properties required for use in both of these applications. The Pickering-stabilised antibubble may possess the desired acoustic properties to be such a theranostic agent. An antibubble is a gas bubble containing at least one incompressible core. An antibubble is inherently unstable and thus needs to be stabilised to exist for longer than a moment. One such stabilising method, involving the adsorption of nanoparticles to gas–liquid interfaces, is called Pickering stabilisation. A Pickering-stabilised antibubble responds to an incident sound field by means of radial pulsation and other, more complicated, dynamics.

Despite the potential application of microscopic antibubbles in theranostics, their dynamic behaviour and the acoustic regimes in which this behaviour occurs are not known.

The purpose of this research was to predict the dynamic response of Pickering-stabilised antibubbles to pulsed ultrasound, and to identify and quantify the contribution of each of the Pickering-stabilised antibubble components to that behaviour.

Radial excursions of antibubbles and their components during ultrasound exposure were extracted from high-speed footage. The applied ultrasound had a centre frequency of 1 MHz and pressure amplitudes between 0.20 MPa and 1.30 MPa. Moreover, damping coefficients, pulsation phases, and excursions of antibubbles and antibubble components were computed with equations describing a forced mass–spring–dashpot system and an adapted Rayleigh-Plesset equation. Over a range of driving pressure amplitudes, fragmentation thresholds were computed for antibubbles of varying size, core volume, shell stiffness, and driving frequency. In addition, the feasibility of an antibubble component for the disruption of cell walls was tested.

From the experimental data, it was found that antibubble contractions and expansions were symmetrical and predictable at an acoustic amplitude of 0.20 MPa,

whilst the pulsations were asymmetrical and less predictable at an acoustic amplitude of 1.00 MPa. These results show that the presence of the core inside of the antibubble hampers the contraction of a collapsing antibubble and ameliorates its stability. Consequently, Pickering-stabilised antibubbles appear to be feasible candidates for ultrasonic imaging, with greater stability than the agents currently in use.

Micron-sized antibubbles, much smaller than resonant size, were computed to have a pulsation phase difference of up to $\frac{1}{6}^{\text{th}}$ of a cycle with respect to free gas bubbles. The difference in oscillation phase is a result of the increased damping coefficient caused by the friction of the internal components and shell of the antibubble. This indicates that altering the damping of the shell or skeletal material of minute antibubbles can alter the degree to which the particle's oscillation is in phase with the sound field.

The shell stiffness of Pickering-stabilised microbubbles without incompressible contents was measured to be $7.6\,\mathrm{N\,m^{-1}}$ throughout low-amplitude sonication. Under high-amplitude sonication, the maximum expansions of microbubbles, measured from high-speed camera footage, were either agreeing with those computed for Pickering-stabilised microbubbles or corresponding to greater values. The differing oscillation amplitudes for similarly sized microbubbles is attributed to shell disruption of different severity.

For a 3-μm radius antibubble with a 90% core radius, subjected to a pulse of centre frequency 1 MHz, the fragmentation threshold was computed to drastically increase with shell stiffness. At a driving frequency of 13 MHz, the fragmentation threshold was computed to correspond to a mechanical index less than 0.4, irrespective of shell stiffness. Shell stiffness changes the resonance frequency, and thus the fragmentation threshold of antibubbles. This means that the resonance frequency of an extremely low concentration and quantity of homogeneous agent can be determined using microscopy. At driving frequencies above 1 MHz, the fragmentation threshold was computed to correspond to a mechanical index of less than 0.5, irrespective of shell stiffness.

Antibubbles exposed to high-amplitude ultrasound were found to have an exponential fragment size distribution. This brings us closer to understanding and controlling disruption and material release for these particles. If the pressure of the regime is known, the number of antibubble fragments produced can be theoretically determined.

Under low-amplitude ultrasound exposure, hydrophobic particles, a common component of antibubbles, were observed to jet through wood fibre cell walls, without causing visible internal structural damage to these cells. Hydrophobic particles can thus act as inertial cavitation nuclei which collapse asymmetrically close to solid boundaries such as wood pulp fibres. This indicates that hydrophobic particles on their own may be used for applications such as trans-dermal drug delivery.

The dynamic response of Pickering-stabilised antibubbles to ultrasound has been predicted. Furthermore the respective behaviour of Pickering-stabilised antibubble components under theranostic ultrasound conditions has been identified. This work has led to a straightforward way to determine the elasto-mechano properties of small samples of contrast agent.

Whilst possessing some theranostic properties, Pickering-stabilised antibubbles may be more suitable as replacements for current diagnostic agents. Hydrophobic particles, a current constituent of the Pickering-stabilised antibubble, may however, prove to be promising theranostic agents.

CONTENTS

ABBREVIATIONS AND SYMBOLS

A	area [m^2]
C_p	specific heat of gas [$J\,kg^{-1}\,K^{-1}$]
d	diameter [m]
d_1	distribution parameter [m]
d_c	characteristic diameter [m]
E_k	kinetic energy [J]
E_s	surface energy [J]
f_c	centre frequency [Hz]
f_r	resonance frequency [Hz]
K_g	thermal conductivity of the gas [$W\,m^{-1}\,K^{-1}$]
MI	mechanical index [ ]
N	number of fragments [ ]
N_{at}	number of pixels with greyscale value above the threshold value [ ]
N_{bt}	number of pixels with greyscale value below the threshold value [ ]
N_{tot}	total number of pixels [ ]
$P(t)$	ultrasound pressure [Pa]
p_0	ambient pressure [Pa]
p_v	vapour pressure [Pa]
P2P	peak-to-peak pressure [Pa]
PNP	peak-negative pressure [Pa]
PNP_{TH}	threshold peak-negative pressure [Pa]

PPP	peak-positive pressure [Pa]
PRF	pulse repetition frequency [Hz]
PRT	pulse repetition time [s]
R	instantaneous radius [m]
$\dot{R}$	instantaneous radial velocity [$\mathrm{m\,s^{-1}}$]
$\ddot{R}$	instantaneous radial acceleration [$\mathrm{m\,s^{-2}}$]
R_0	initial resting radius [m]
R_c	core radius [m]
R_cr	Blake's threshold radius [m]
R_fin	final resting radius [m]
R_max	maximum radius [m]
R_min	minimum radius [m]
T	period [s]

α	phase difference between the antibubble pulsation and the incident sound field [rad]
γ	polytropic exponent of the gas [ ]
δ	damping coefficient [ ]
η	bulk fluid viscosity [Pa s]
ξ^-	negative first cycle excursion [m]
ξ^+	positive first cycle excursion [m]
$\xi^+ - \xi^-$	oscillation asymmetry [m]
ρ	liquid density [$\mathrm{kg\,m^{-3}}$]
ρ_g	density of the gas [$\mathrm{kg\,m^{-3}}$]
σ	surface tension [$\mathrm{N\,m^{-1}}$]
σ_at	in-class variance of pixels with greyscale value below the threshold [ ]
σ_bt	in-class variance of pixels with greyscale value below the threshold [ ]
σ_icv	in-class variance [ ]
χ	shell stiffness [$\mathrm{N\,m^{-1}}$]
ω	angular centre frequency of ultrasound pulse [$\mathrm{rad\,s^{-1}}$]
ω_r	angular resonance frequency [$\mathrm{rad\,s^{-1}}$]

ORIGINAL PUBLICATIONS

Publication I D. M. Rubin, N. Anderton, C. Smalberger, J. Polliack, M. Nathan, and M. Postema, "On the behaviour of living cells under the influence of ultrasound," *Fluids*, vol. 3, no. 4, 82, 2018. DOI: 10.3390/fluids3040082.

Publication II N. Kudo, R. Uzbekov, R. Matsumoto, R.-i. Shimizu, C. S. Carlson, N. Anderton, A. Deroubaix, C. Penny, A. T. Poortinga, D. M. Rubin, A. Bouakaz, and M. Postema, "Asymmetric oscillations of endoskeletal antibubbles," *Japanese Journal of Applied Physics*, vol. 59, no. SK, SKKE02, 2020. DOI: 10.35848/1347-4065/ab79e7.

Publication III N. Anderton, C. S. Carlson, V. Aharonson, and M. Postema, "Determining the influence of endoskeleton friction on the damping of pulsating antibubbles," *Current Directions in Biomedical Engineering*, vol. 8, no. 2, pp. 781–784, 2022. DOI: 10.1515/cdbme-2022-1199.

Publication IV N. Anderton, C. S. Carlson, R. Matsumoto, R.-i. Shimizu, A. T. Poortinga, N. Kudo, and M. Postema, "On the rigidity of four hundred Pickering-stabilised microbubbles," *Japanese Journal of Applied Physics*, vol. 61, no. SG, SG8001, 2022. DOI: 10.35848/1347-4065/ac4adc.

Publication V N. Anderton, C. S. Carlson, R. Matsumoto, R.-i. Shimizu, A. T. Poortinga, N. Kudo, and M. Postema, "First-cycle oscillation excursions of Pickering-stabilised microbubbles subjected to a high-amplitude ultrasound pulse," *Current Directions in*

Biomedical Engineering, vol. 8, no. 2, pp. 30–32, 2022. DOI: 10.1515/cdbme-2022-1009.

Publication VI N. Anderton and M. Postema, "Fragmentation thresholds simulated for antibubbles with various infinitesimal elastic shells," *Current Directions in Biomedical Engineering*, vol. 8, no. 2, pp. 73–76, 2022. DOI: 10.1515/cdbme-2022-1020.

Publication VII N. Anderton, C. S. Carlson, N. Kudo, A. T. Poortinga, and M. Postema, "The ultrasound-triggered explosion of an endoskeletal antibubble yields a predictable fragment size distribution," *Japanese Journal of Applied Physics*, vol. 60, no. 12, 128001, 2021. DOI: 10.35848/1347-4065/ac3184.

Publication VIII N. Anderton, C. S. Carlson, A. T. Poortinga, H. Xinyue, N. Kudo, and M. Postema, "Sonic disruption of wood pulp fibres aided by hydrophobic cavitation nuclei," *Japanese Journal of Applied Physics*, vol. 62, no. 1, 018001, 2023. DOI: 10.35848/1347-4065/acaadd.

Author's contribution

Publication I	Rubin and Postema conceived the original idea. Anderton and Smalberger sourced and summarised articles. Postema and Rubin drafted the manuscript. Anderton developed and populated the summary table and organised the references. All authors discussed the final order and presentation of summarised information.
Publication II	Kudo and Postema conceived the original idea. Poortinga supplied the antibubble samples. Matsumoto, Shimizu and Kudo supplied the high-speed video footage. Carlson, Deroubaix, and Penny supplied the microscope images. Anderton processed and analysed all the results. Kudo and Postema drafted the manuscript with input from Anderton. All authors discussed and contributed to the final manuscript.
Publication III	Anderton and Postema conceived the original idea. Anderton performed the simulations, analysed the results, and drafted the manuscript with the support of Carlson and Postema. All authors discussed and contributed to the final manuscript.
Publication IV	Anderton, Carlson and Postema conceived the original idea. Poortinga supplied the antibubble samples. Matsumoto, Shimizu and Kudo supplied the high-speed video footage. Anderton analysed the results, and drafted the manuscript with the support of Carlson and Postema. All authors discussed and contributed to the final manuscript.
Publication V	Anderton and Postema conceived the original idea. Poortinga supplied the antibubble samples. Matsumoto, Shimizu and Kudo supplied the high-speed video footage. Anderton developed the simulations, analysed the results, and drafted the manuscript with the support of Postema. All authors discussed and contributed to the final manuscript.

Publication VI Anderton and Postema conceived the original idea. Anderton developed the simulations, analysed the results, and drafted the manuscript with the support of Postema. Both authors discussed and contributed to the final manuscript.

Publication VII Poortinga and Postema conceived the original idea. Poortinga supplied the antibubble sample. Kudo obtained the high-speed video footage. Anderton processed and analysed the results. Anderton, Carlson and Postema drafted the manuscript. All authors discussed and contributed to the final manuscript.

Publication VIII Anderton, Carlson and Postema conceived the original idea. Poortinga supplied the hydrophobic zinc oxide samples. Anderton and Carlson obtained the near-audible control dataset. Hu and Kudo supplied the high-speed video footage. Anderton performed the simulations and analysed the results. Anderton, Carlson, and Postema drafted the manuscript. All authors discussed and contributed to the final manuscript.

1 INTRODUCTION

Diseases such as cancer, where the uncontrolled growth of malignant cells wreaks havoc on the body, are becoming increasingly prevalent [25]. While the cancer mortality relative to the number of new cases has decreased in recent years, the means of treatment are still far from ideal. Treatment methods often involve invasive surgery coupled with, or replaced by, chemotherapy and radiotherapy. The methods and agents used in these therapies are non-selective in their destruction of cells, often leaving the patient undergoing treatment to suffer severe side effects [78], [81]. This is all without considering the escalating costs of these drugs and treatments [45].

In an ideal world, treatment would comprise identifying, targeting and destroying only malignant and unwanted cells, whilst leaving the healthy cells unharmed. Ultrasound is an elegant modality for this application, as it is one of few modalities that can be used for both diagnostic imaging and therapeutic treatment. It is also non-invasive, inexpensive, reliable and safe [93]. Studies investigating the effect that ultrasound has on individual cells are limited and indicate that the technology is not yet advanced enough to differentiate the acoustic footprint of individual cells from one another [I]. Despite this, ultrasound can still be harnessed to improve the efficiency and lessen the overall damage caused by current treatments whilst the technology, and scientific knowledge required, to target specific cells catches up.

Ultrasound has been suggested as a 'theranostic' modality, intended to both diagnostically image, as well as deliver therapeutic drugs to a targeted location in the body [34]. Sonoporation has further fuelled scientific interest in ultrasound's potential therapeutic capabilities. The phenomena is described as the ultrasound induced transient permeation, and resealing of cell membranes has been observed to result in increased drug uptake [48], [70]. The addition of microbubbles has been shown to further enhance this phenomena; with studies including them reporting increased chemotherapeutic uptake during cancer treatment [37], [72].

Microbubbles are gas filled particles, between 1 and 10 μm in radius, that oscillate in the presence of ultrasound and thus make excellent markers for blood in applications such as perfusion imaging [27]. They can be made to translate, coalesce, fragment, jet, cluster and dissolve in a sound field depending on their elastic properties and the environmental and applied ultrasound conditions [70]. Owing to their diverse behaviour, their already common use as clinical ultrasound imaging agents, and their known ability to enhance the sonoporation effect, numerous studies and reviews exploring the potential of microbubbles as drug delivery agents naturally followed [28], [67], [87]. The issue of loading microbubbles with drugs has been a challenging one however, with most attempting to add drugs in one manner or another to the microbubble shell [9], [49], [50], [55]. A number of setbacks have been encountered with these methods including; relatively low drug loading capacity owing to limited shell area, and unstable drug release as the shells become more viscous and less oscillatory, requiring higher and thus less clinically safe ultrasound pressure thresholds to rupture [1], [39].

A proposed alternative to loading the shell of a microbubble is to instead load drugs into one or multiple cores inside of a microbubble [65], [67], [96]. The addition of a core within a microbubble results in what has come to be known as an antibubble. The term originally arose to describe the seemingly opposite nature of a liquid or solid core surrounded by gas, compared to that of a conventional free gas bubble surrounded by liquid [29], [90]. Minute antibubbles naturally form in water and exist for only a few seconds before they are overcome by surrounding pressure forces [19]. Only recently has a Pickering stabilisation method been developed to stabilise micrometer size antibubbles for significantly longer periods of time, making them potentially viable for industrial and medical applications [62], [82]. Pickering-stabilised emulsions have been found to have internal-phase volume fractions of greater than 74%, indicating strong drug loading capacity [20]. It has additionally been shown that, compared to the surfactant-stabilised interfaces of lipid shells, Pickering-stabilised interfaces exhibit far greater stability against coalescence [86]. Much about the dynamics of these Pickering-stabilised antibubbles under sonication still needs to be understood however, with preliminary simulation and *in-vitro* studies focusing on the radial pulsation and subsequently generated harmonics [32], [38], [60], [71].

A significant obstacle limiting research progress of antibubbles for use in medical applications has been the inconsistent size distribution of samples, with some particles larger than 10 μm in size [60]. However, Kotopoulis recently published a study in which 99% of the Pickering-stabilised antibubbles developed were less than 10 μm in size. These antibubbles were further tested as ultrasound drug delivery agents in vitro, with promising proof-of-concept results [39]. The study highlighted the need for further research into the mechanisms of antibubble drug release and the safety parameters of antibubble fragmentation.

This research aims to address this knowledge gap, with the purpose of gaining further insight into the Pickering-stabilised antibubble and its properties by predicting the dynamic response of Pickering-stabilised antibubbles to pulsed ultrasound, and identifying and quantifying the contribution of each of the antibubble components to that behaviour. To address this purpose, analysis of what is currently known about the effect of ultrasound on individual cells and where the limitations are was conducted. The summary is presented in Study I. Chapter 2 details some of the more complex, but necessary, bubble and antibubble dynamics required for this study, along with relevant literature. Chapter 3 details the aims of this research in relation to each study. Chapters 4 and 5 describe the materials and methods used and present a summary of results from Studies II-VIII. Studies II and III explore the effect of the antibubble's core on antibubble oscillation behaviour during sonication. Studies IV and V explore the effect of the Picking-stabilised outer shell on antibubble oscillation behaviour during sonication. Studies VI and VII explore the fragmentation conditions and phenomena of antibubbles. Finally, Study VIII investigates the behaviour of hydrophobic zinc oxide particles, which are used to form the endoskeletal structure of antibubbles, in the presence of cells. Chapter 6 presents a discussion of the results observed in the previous chapter and concludes this body of research.

2 BACKGROUND

This chapter details the theoretical background and literature related to this research. A summary of the relevant medical ultrasound principles and terms used throughout this research is first given, followed by the relevant theory on bubble dynamics and models thereof developed thus far. Finally, relevant literature on ultrasound, ultrasound contrast agents, and cells is discussed.

Ultrasound waves are mechanical vibrations that propagate through matter at frequencies higher than 20 kHz [64]. In medical settings frequencies below 500 kHz are rarely used, and frequencies upwards of 10 MHz are exclusively used for biomicroscopy and the non-destructive evaluation of cells [12], [79]. For a given location, an ultrasound wave is characterised by a number of parameters. The first described here, being centre frequency f_c, is defined as the number of cycles per second. The period T is the reciprocal of the centre frequency. The peak-negative pressure PNP and peak-positive pressure PPP refer to the minimum and maximum pressure amplitudes of the wave, respectively, with the peak-to-peak pressure P2P being the sum of their absolute values. The pulse length describes the total duration of the wave sequence. Duty cycle, given as a percentage, denotes the transmission time per each pulse. Pulse repetition time PRT is the time lapsed between the start of two consecutive pulses, and pulse repetition frequency PRF is its reciprocal [64], [1]. Figure 2.1 depicts a visual representation of two ultrasound pulses, of three cycles each, with many of the above described parameters presented visually.

For medical applications, the PNP and f_c are used to calculate the mechanical index MI,

$$\mathrm{MI} = \frac{\mathrm{PNP}}{\sqrt{f_c}} \,, \tag{2.1}$$

where PNP is given in MPa and normalised by 1 MPa and f_c is given in MHz and normalised by 1 MHz [64]. The term gives an indication of the relative safety of exposed tissue from inertial cavitation, which has been known to cause free-radical

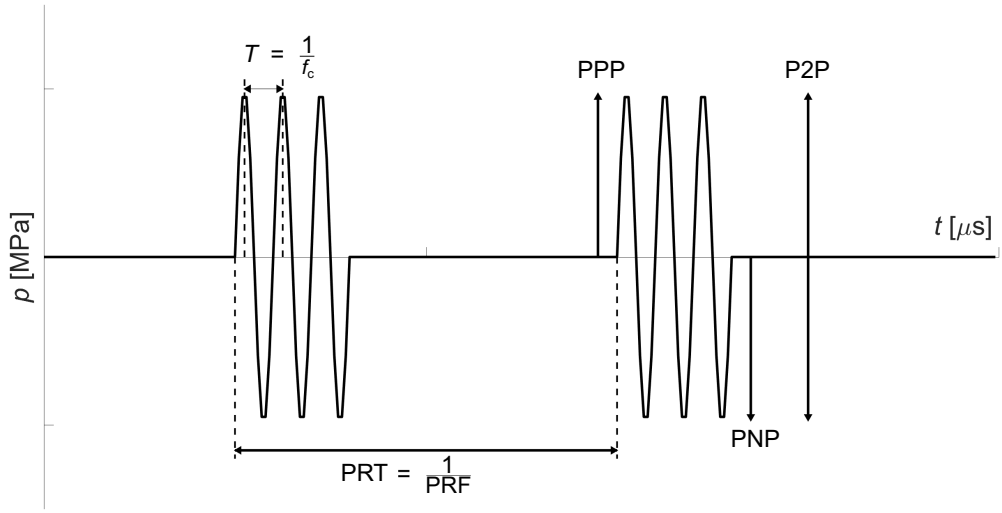

Figure 2.1 Visual representation of two ultrasound pulses, each consisting of three cycles with the same centre frequency f_c. The dominant period T, peak-positive pressure PPP, peak-negative pressure PNP, pulse repetition period PRT, and pulse repetition frequency PRF are clearly shown.

formation and biological damage [6], [10], [77]. MI is derived from the proportional relationship between the threshold peak-negative pressure $\mathrm{PNP_{TH}}$, at which cavitation takes place, and the frequency of the applied ultrasound, which is described by: $\mathrm{PNP_{TH}^{2.10}} \propto f_c$ in water [1], [3]. An MI of less than 0.3 is deemed safe for medical diagnostic purposes, whilst a higher MI, below 0.7, has been shown to cause minor damage to neonatal soft tissues [26], [64]. An MI of greater than 0.7 indicates a considerable risk of cavitation and is thus not safe for clinical application [68]. Commercial medical imaging scanners have an absolute MI limit of 1.9 [4].

While inertial cavitation can indeed be dangerous, cavitation has been noted to occur under less powerful ultrasound conditions when microbubbles or cavitation nuclei are present in or near cells. This form of cavitation has been associated with sonoporation and the movement and permeation of cultured cells [1], [23], [80], [94].

When bubbles are exposed to ultrasound, they begin to oscillate in response to the forces acting on them [51]. These forces can also cause them to translocate and attract or repel other nearby bubbles [46]. The mechanical properties of the bubble, the properties of the applied sound wave, and the environmental conditions all play a role in exactly how the bubble responds when exposed to ultrasound. An under-

standing of the physics behind this behaviour is vital in realising and computationally modelling the dynamics of any bubble under sonication.

A bubble must first however, be defined. A free gas bubble is exactly that, a spherical pocket of gas contained in a liquid medium. For the purpose of this investigation, the definition of encapsulated and stabilised microbubbles and antibubbles are also included. Microbubbles and antibubbles are both gas containing entities, surrounded by an outer shell. The shell of microbubbles typically used as ultrasound contrast agents are made of lipids and are either elastic or viscoelastic in nature [7], [95]. The antibubbles investigated in this study incorporated a shell of hydrophobised silica nanoparticles, which was stabilised using a Pickering-stabilisation process [62], [63]. An antibubble further contains a core of some liquid or solid material. Illustrations of a free gas bubble, a simplified encapsulated microbubble and a simplified encapsulated antibubble are shown in Figure 2.2.

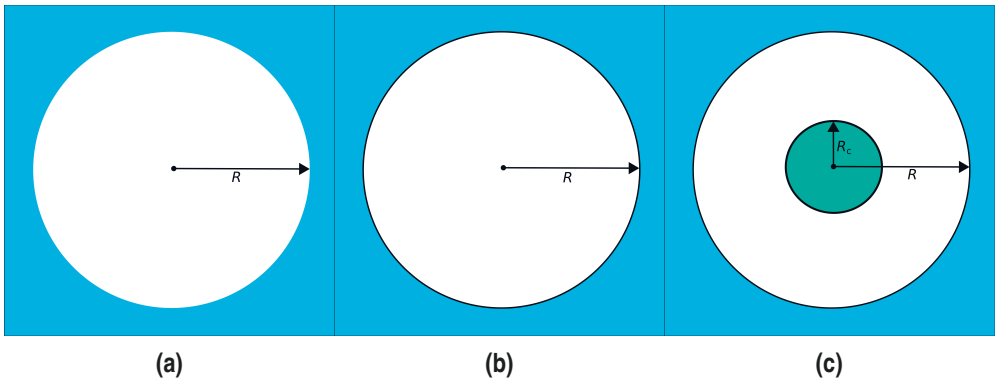

Figure 2.2 Side-by-side simplified schematics of a free gas bubble (a), an encapsulated microbubble (b), and an encapsulated antibubble (c). Gas is shown in white, liquid in blue, core material in turquoise, and shell material in black.

When exposed to ultrasound at low acoustic amplitudes, with an MI less than 0.1, bubbles expand and contract linearly. At higher acoustic amplitudes, bubble oscillation becomes non-linear, often resulting in bubble collapse when the MI is greater than 0.6 [64]. The derivation of the equations used to describe the non-linear bubble motion under sonication can be traced back to Lord Rayleigh's first model of the collapse of an empty cavity in a liquid [22], [76]. Following the model's development, researchers considered adding gas and vapour to the cavity, an external driving pressure, surface tension and viscosity terms [57], [58], [61]. This ultimately lead to the development of the Rayleigh-Plesset equation. The equation describes the non-

linear behaviour of bubble dynamics and has formed the base upon which all free gas bubble models, and many contrast agent models, are based [16], [46].

To eliminate repetition, an adapted form of the equations from [31] and [33] that accounts for the presence of an incompressible core and a stiff shell is presented:

$$R\ddot{R} + \tfrac{3}{2}\dot{R}^2 = \frac{1}{\rho}\left[\left(p_0 - p_v + \frac{2\sigma R_0}{R_0^2 - R_c^2}\right)\left(\frac{R_0^3 - R_c^3}{R^3 - R_c^3}\right)^{\gamma} + p_v - \frac{2\sigma R}{R^2 - R_c^2} - 2\chi\left(\frac{1}{R_0} - \frac{1}{R}\right) - \frac{4\eta\dot{R}}{R} - p_0 - P(t)\right], \tag{2.2}$$

where $P(t)$ is the driving pressure as a function of time t, p_0 is the ambient pressure, p_v is the vapour pressure, R is the instantaneous radius of the bubble, $\dot{R}$ is its first time-derivative, $\ddot{R}$ is its second time-derivative, R_0 is the resting radius of the bubble, R_c is the incompressible core radius, γ is the polytropic exponent of the gas, η is the viscosity of the surrounding fluid, ρ is the density of the surrounding fluid, σ is the surface tension, and χ is the outer shell stiffness.

In this state, (2.2) represents the pulsation of a simplified, perfectly spherical, antibubble in an infinite incompressible fluid depicted in Figure 2.2c. If R_c is set to zero, (2.2) represents the pulsation of the simplified microbubble depicted in Figure 2.2b. If both R_c and χ are set to zero, the equation becomes the original Rayleigh-Plesset equation and a representation of the pulsation of a free gas bubble depicted in Figure 2.2a.

It should be noted that the validity of (2.2) relies on a number of assumptions. These assumptions include that the gas inside of a bubble is polytropic, that the shell is of negligible thickness, and that buoyancy is negligible owing to the small bubble dimensions [64]. As (2.2) treats a bubble as a one-dimensional entity, it does not hold for larger bubbles, for which three-dimensional adaptations are required to account for pressure gradients owing to gravity.

A number of updates and variations of the Rayleigh-Plesset equation followed its initial development, with some of the most notable being the adaptations for the changes in surface tension owing to surface buckling, shells with varying properties, and the presence of an additional nearby oscillator [8], [15], [17], [24], [52], [88]. Many, more recent, models contain additional parameters and terms that cannot be physically measured, even with high-speed photography. Numerous reviews describe and compare the models [22], [54], [89], [91]. Despite the growth of the field,

a model that fits the reality of shelled-bubble oscillation in varying conditions has yet to be developed. Two of the biggest reoccurring limitations of the models are the seeming dependence of the material properties on the initial size of the bubbles, and the asymmetric oscillation to seemingly require the shell to possess different physical properties during expansion and contraction [16]. The basic Rayleigh-Plesset equation should still provide a sufficiently accurate representation of the radial dynamics of a bubble, provided that the pulsation velocity is less than the speed of sound and only the first few pulsation cycles are considered, before viscoelastic shell effects and interactions with other entities in the finite fluid influence the pulsation.

Apart from oscillating, a bubble can also translocate within a sound field owing to primary and secondary radiation forces. Primary radiation forces are a result of the pressure gradient across the surface of a bubble. In a travelling wave, the forces will cause the bubble to move in the direction of the sound field. In a standing wave, bubbles will move to a location which corresponds to the nodes or antinodes of the standing pressure wave. The angular frequency of the transmitted wave and the resonance frequency of the bubble determine which of the nodes the bubble will move to [51], [64]. Secondary radiation forces are the result of other bubbles oscillating nearby. Bubbles oscillating in phase with the sound field move toward one another, whilst bubbles oscillating out of phase repel one another [1], [40], [46], [72]. These bubble dynamics are termed higher-order effects, the impact of which on bubble dynamics has been studied and reviewed [36], [89].

Adapting for core and shell presence as in (2.2), the resonance frequency f_r of an antibubble can be computed as follows [38], [72]:

$$f_r = \left(\frac{1}{2\pi R_0\sqrt{\rho}}\right)\sqrt{3\gamma\frac{\left(p_0 - p_v + \frac{2\sigma R_0}{R_0^2 - R_c^2}\right)}{1-\left(\frac{R_c}{R_0}\right)^3} + \frac{2\sigma R_0}{R_0^2 - R_c^2} - \frac{4\eta^2}{\rho R_0^2} - \frac{2\chi}{R_0}}\,. \tag{2.3}$$

By setting R_c to zero, (2.3) can be used to calculate the resonance frequency of a simplified microbubble as depicted in Figure 2.2b. By setting both R_c and χ to zero, (2.3) can be used to calculate the resonance frequency of a free gas bubble. It should be clear from (2.3), that the addition of the core results in antibubbles having a higher resonance frequency than microbubbles. Bubble models which have included the more complex viscoelastic nature of surrounding biological tissue, have noted a considerable change in bubble resonance frequency with varying the elastic modulus surrounding the bubble [18], [56]. Shell material properties have been shown to

influence the resonance frequency of microbubble contrast agents [14].

When exposed to high-amplitude ultrasound, with an MI of over 0.6 and a frequency much less than the resonance frequency of a given bubble, a bubble may experience explosive growth as it reaches a critical threshold radius at which no stable equilibrium radius exists. This is known as Blake's threshold radius R_{cr}, and has been approximated as twice the size of the initial radius of the bubble. This results in a phenomenon known as cavitation, the violent collapse of the bubble during the contraction phase of oscillation [72]. During its collapse, a bubble can fragment into a number of smaller bubbles. Fragmentation occurs when the kinetic energy E_{k} of the bubble,

$$E_{\mathrm{k}} \approx 2\pi\rho\dot{R}^2R^3\,, \tag{2.4}$$

surpasses the difference in surface energy E_{s} of the single bubble and the combined surface energy of the number of fragments the bubble could break into,

$$\Delta E_{\mathrm{s}} \approx (N^{\frac{1}{3}} - 1)\cdot 4\pi R^2\sigma\,, \tag{2.5}$$

where N is the number of fragments [73]. The number of fragments is proportional to the dominant spherical oscillation mode, with relationship $N \approx n^3$. Thin shell-encapsulated microbubbles have been associated with mode 2 oscillations, yielding eight fragments [64]. Understanding the fragmentation threshold of any drug carrier is vital for controlling payload release. Another disruption mechanism of interest is sonic cracking, in which the gaseous content of the bubble is released during the bubble expansion phase [74].

All of the bubble dynamics discussed thus-far may play a role in the increased drug uptake observed of cells during the sonoporation phenomena already discussed. Whilst the interaction of acoustically active bubbles near cells has been investigated, the exact mechanisms of enhanced sonoporation are not yet understood [43], [49], [85]. However, some theories include; the push mechanism, in which a microbubble may cause localised cell disruption as it pushes against a cell membrane during microbubble expansion. There is also the pull mechanism, in which the membrane might be pulled and ruptured as an attached microbubble contracts. Additionally, there is the streaming mechanism, in which the movement of fluid around the oscillating microbubble causes shear stress and eventual rupture of any cell membrane the

microbubble is attached to [53], [70]. Still, none of these mechanisms are likely to contribute significantly toward sonoporation if the walls of both the cell and the microbubble are not in contact prior to sonication. Another potential mechanism is translation owing to radiation forces. The final mechanism denominated here is jetting, which only occurs under high-amplitude sonication and is the result of a funnel-shaped protrusion through a microbubble towards its boundary formed as the microbubble collapses asymmetrically. As cells generally do not survive being jetted through, this mechanism is unlikely to play a dominant role, if any, in sonoporation [69], [75].

The preponderance of literature describing the investigation of the effect of ultrasound on cells has involved the presence of bubbles. Despite this, the interaction of cells alone in the presence of ultrasound has been modelled previously, with adaptations of the Rayleigh-Plesset described in (2.2) and derived one-dimensional translation equations [32], [41], [51]. The resulting studies showed no cell destruction at low acoustic amplitudes, and limited cell translation [11], [46], [83]. Johansen suggested that, given the incompressible nature of the red blood cell's internal monolayer, they could be modelled using the same equations used for antibubble oscillation modelling [30], [38]. Proliferation, translation, apoptosis, lysis, transient membrane permeation, oscillation, cytoskeletal changes and internal structural changes have all been noted in preliminary experimental investigations, an overview of which is presented in table format in [I].

3 OBJECTIVES

The purpose of this research is to predict the dynamic response of Pickering-stabilised antibubbles and their components to pulsed ultrasound, and to identify and quantify the contribution of each of those components to this behaviour.

The specific study objectives were to:

1. understand limitations of ultrasound's effect on individual cells (Study I);
2. determine effect of antibubble core content on antibubble oscillation and stability (Study II);
3. determine influence of endoskeletal friction on pulsation phase (Study III);
4. determine Pickering-stabilised shell stiffness (Study IV);
5. determine influence of high-amplitude sonication on Pickering-stabilised shell integrity (Study V);
6. predict fragmentation threshold of antibubbles (Study VI);
7. determine antibubble fragment size distribution (Study VII);
8. observe antibubble core content in the presence of biological cells during sonication (Study VIII).

4 MATERIALS AND METHODS

This dissertation is the summation of a review and a number of experimental and simulation studies. The review was used to gain insight into the limitations in the field, with the experimental and simulation studies aimed at extending these limits. A description of the materials and methods used during this research is presented in this chapter. The materials and sample preparation procedures for all of the studies are described in Section 4.1. Following this, the experimental setups and experimental procedures are described, along with the computational ones in Section 4.2. Section 4.3 gives a breakdown of how each of the materials, methods, setups and computational methods are used to achieve each study's objective.

4.1 Sample preparation

4.1.1 Antibubbles

Two types of Pickering-stabilised antibubble media were used in Studies II, IV, V and VII for this investigation. One contained cores with 2 vol% endoskeletal content whilst the other contained no core content [44]. The core-less antibubbles are referred to as reference (REF) bubbles in Publication II and Pickering-stabilised microbubbles in Publications IV and V.

A schematic representation of an antibubble and a core-less shell-stabilised antibubble is depicted in Figure 4.1. Although from a conceptual point of view, free bubbles and antibubbles would be desirable study objects, such entities cannot be created in a stable from. Therefore, in this study, only stabilised microbubbles and antibubbles are considered.

The antibubbles were prepared using a water-in-oil-in-water double emulsification process described in detail in [63]. The outer antibubble shells were stabilised using Aerosil® R972 hydrophobised fumed silica particles (Evonik Industries AG,

Essen, Germany). The silica particles were all below 30 nm in diameter and were observed to form a single elastic layer around the surface of the antibubbles after dispersion with an ultrasound probe. Hydrophobically modified Zano 10 Plus zinc oxide (ZnO) nanoparticles (Umicore, Brussels) were used to create the stabilising endoskeletal core content of the antibubbles. These ZnO particles averaged 50 nm in diameter and were observed to form a tightly packed layered structure on the surface of the antibubbles [71]. A freeze-drying process was then followed to remove the water and hexane oil used in the emulsification process [63].

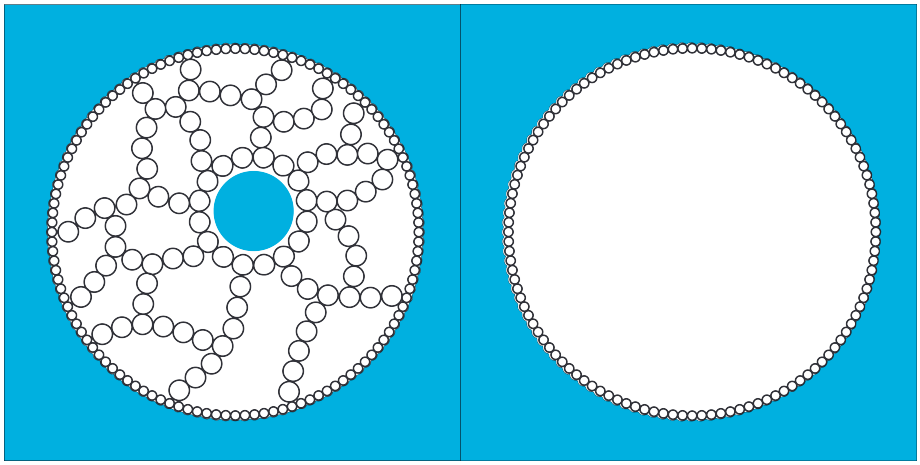

(a) Antibubble **(b)** Core-less antibubble

Figure 4.1 Side by side schematics of a Pickering-stabilised antibubble with (a), and without (b) core content. The core, depicted as a blue circle, is surrounded by endoskeletal ZnO particles inside the antibubble to the left, whilst the silica particles surrounding both antibubbles is seen in both figures. Re-drawn from [III].

To prepare the antibubble samples for experiments, 5 mg of the then freeze-dried antibubbles were diluted with 5 mL of 049-16797 distilled water (FUJIFILM Wako Pure Chemical Corporation, Chuo-Ku, Osaka, Japan) in a 15 mg FALCON® high quality polypropylene conical tube. Each sample was then gently shaken for one minute. Finally, a pipette was used to move 0.2 mL of the sample from the tube into the experimental observation chamber [1], [63]. The resulting antibubbles contain air and one or more water droplets [60]. Throughout this study, the skeleton and droplets have been considered as one incompressible volume with an equivalent core radius R_c. Droplet vaporisation and asymmetry of antibubble geometry have not been taken into account.

For illustrative purposes, Figure 4.2 presents a scanning electron microscope micrograph of a ruptured antibubble. In the figure, the endoskeletal structure can be seen beneath the outer silica membrane.

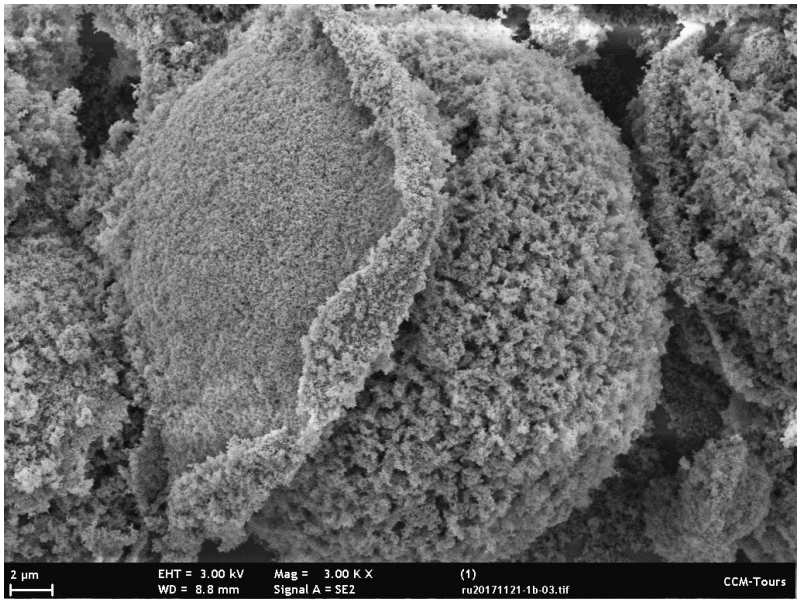

Figure 4.2 Scanning electron micrograph of a ruptured antibubble. The outer silica membrane has shrunk and ruptured allowing for the ZnO endoskeletal structure underneath to be seen. Reprinted from with permission from [44].

4.1.2 Cells and hydrophobic zinc oxide particles

For Study VIII's observation of hydrophobic particles in the presence of cells, both wood pulp and ZnO media were sourced, prepared and then combined. Wood pulp fibre cells were chosen as they were biological cells that were large enough for first viewing, and did not require rigorous ethics clearance procedures necessary for human or animal cells. To prepare the wood pulp, never dried unbleached softwood kraft pulp from a Scandinavian paper mill with a κ number of 85 was washed in water until a neutral pH was reached and then stored at 7 °C. A micrograph of the resulting wood fibre cells is presented in Figure 4.3.

Ready prepared Zano 10 Plus ZnO, coated with octyl triethoxy silane (Umicore, Brussel, Belgium), with particle diameters of less than than 50 nm were sourced. The same Zano 10 Plus ZnO particles were used to form the endoskeleton core of the antibubbles studied throughout this investigation. The octyl triethoxy silane coating

was added in order to hydophobise the ZnO. A scanning electron micrograph of a conglomerate of ZnO particles is presented in Figure 4.4.

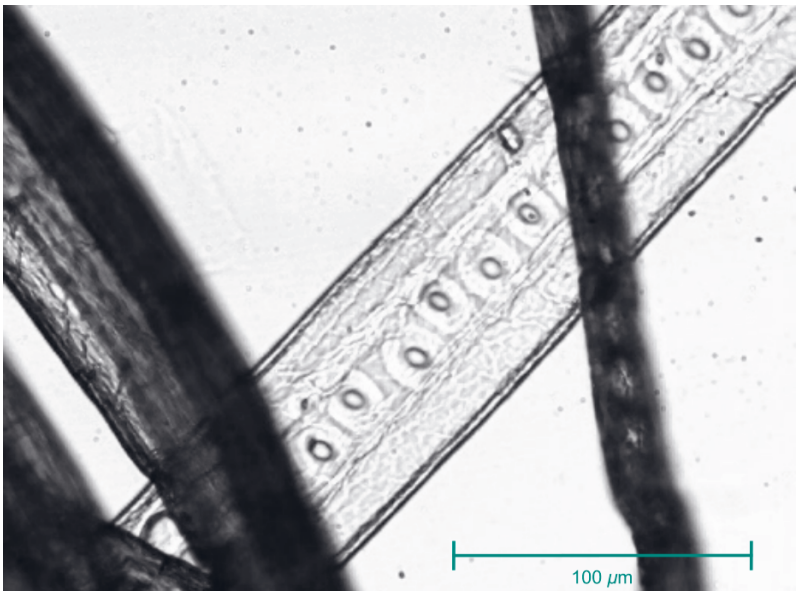

Figure 4.3 Micrograph of wood fibre cells.

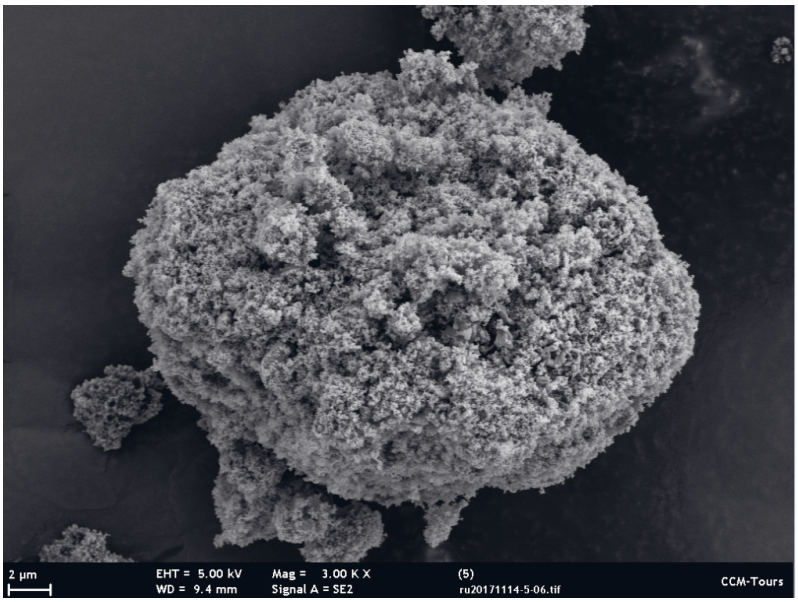

Figure 4.4 Scanning electron micrograph of a conglomerate of ZnO particles. Image acquired from the University of Tours, France: Uzbekov R, Bouakaz A, Postema M.

The wood pulp and ZnO particles used in experiments were prepared in 15 mL Sterile, Polypropylene Disposable Centrifuge Tubes (Thermo Fisher Scientific, Waltham, MA, USA). The preparation process commenced with 5 mL of reverse-osmosis ultrapure (Type 1) water being pipetted into each tube. Next, 5 mg of the ZnO particles was added to half the tubes, so as to have ZnO-free control samples. Finally, 100 mg of wood pulp was added to each tube. Each tube was then gently shaken for 1 minute.

4.2 Experimental setup and procedures

This research involved the analysis of high-speed footage of antibubbles, their components and cells under sonication, as well as computational analysis and simulation of that behaviour. This section details the experimental equipment setup and procedures used in collecting and analysing the footage, as well as the computational methods used in the simulation of antibubble and antibubble component dynamics.

4.2.1 High-speed photography

Studies II, IV, V, VII and VIII required an experimental setup that allowed for the observation and recording of the prepared samples whilst under sonication. A high-speed photography setup developed for a similar purposes, described here and in greater detail in [42], was used to obtain this footage. A labelled sketch of the setup is also given in Figure 4.5.

An AFG320 signal generator (Sony-Tektronicx, Shinagawa, Tokyo, Japan) was connected to a UOD-WB-1000 wide-band power amplifier (TOKIN Coporation, Shiroishi, Miyagi, Japan) that was connected to a laboratory-assembled single-element transducer with a 50-mm aperture, a 1-MHz centre frequency, and a 70-mm focal distance. The transducer produced a single 1 MHz pulse of three cycles each time the signal generator was triggered. A sonication frequency of 1 MHz was selected for the experiments, as a compromise between signal attenuation and tissue penetration depth [1], [84]. The transducer head was submerged in degassed water in a perspex water tank.

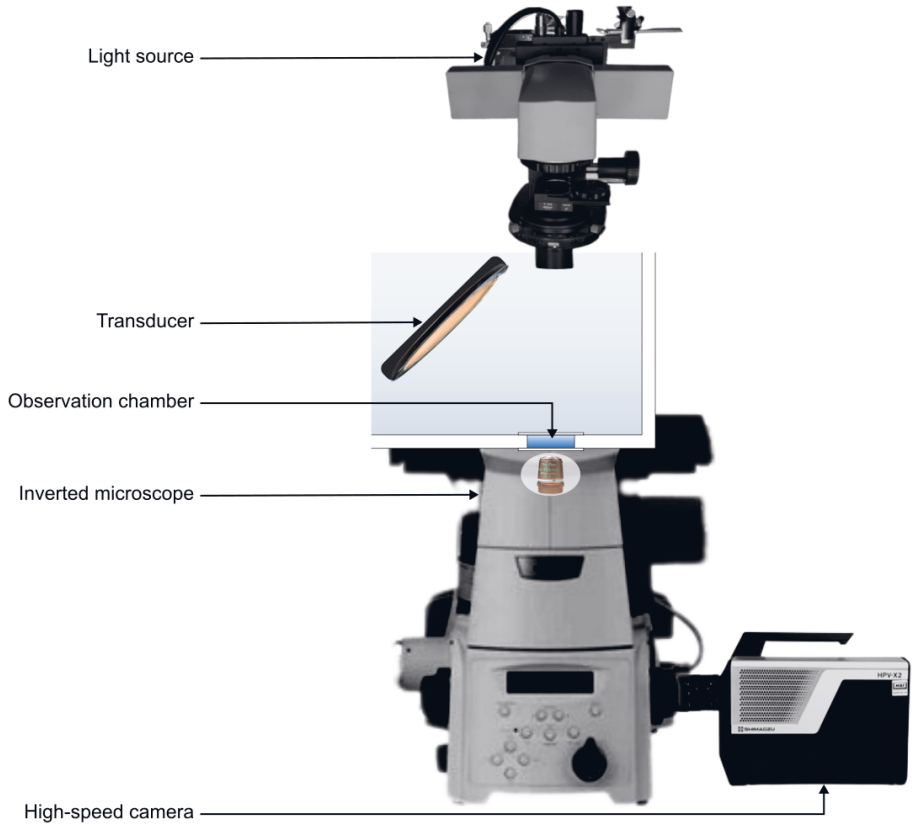

Figure 4.5 Labelled drawing of high-speed photography experimental setup.

An 8 mm diameter cutout, sandwiched between two glass cover slips at the bottom of the water tank, functioned as the sample observation chamber. The chamber was positioned above the Plan Apo LWD 40x WI (N.A. 0.8) objective lens attached to the Eclipse Ti inverted microscope (Nikon Corporation, Minatto-ku, Tokyo, Japan). This high numerical aperture ensured a depth of focus of less than 0.5 μm. A xenon short-arc power flash provided the necessary illumination of the observation chamber during high-speed photography. A HPV-X2 high-speed camera (Shimadzu, Nakagyo-ku, Kyoto, Japan), with a 10 million frames per second shutter speed, was attached to the microscope to record the experiments, providing a total horizontal field of view of 145 μm [42]. A close-up schematic of the observation chamber within the experimental setup is presented in Figure 4.6.

Once the experimental setup was in place, sample observation during sonication could commence. For each experiment, the sample was added to the observation

chamber by removing the water tank from the setup and placing it upside-down on a nearby workbench, with the bottom cover slip removed. A pipette was then used to transfer 0.20 mL of the given sample from the prepared tube into the observation chamber. A new cover-slip was then placed over the observation chamber and taped securely in place. The tank was rotated back into the upright position, placed onto the microscope tray and filled with degassed water, with the transducer head fully submerged in a fixed location.

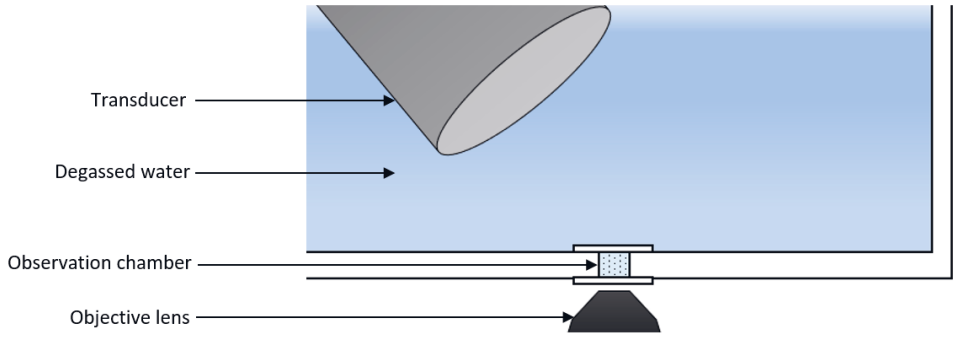

Figure 4.6 Close-up schematic of the observation chamber within the experimental setup. Reprinted with permission from [1].

The signal generator was set to output the desired signal to the transducer upon the trigger button being pressed. The desired output was a sinusoidal wave of three pulses, with an amplitude of either 1 V or 5 V, corresponding to transducer with acoustic amplitude output of 200 kPa or 1 MPa respectively, and MI values of 0.2 and 1 respectively. The power amplifier was turned on, signal generator output channel set to "On" and the high-speed camera switched to the recording state. Once ready to record the experiment, the trigger button was pressed, activating the transducer to produce the single pulse pressure wave. At the same time, the high-speed camera began the 25.5-μs recording. The recording was then saved for later processing. Before changing the sample in the observation chamber, the amplifier and the signal generator output channel were turned off. The tank was then removed from the setup, emptied of water and turned upside-down again to access the observation chamber. The bottom cover-slip was once again removed, the observation chamber cleaned, and the process of pipetting the new sample was repeated as described above.

4.2.2 Experimental setup for control experiment

A control experiment was used in Study VIII to observe the effect of near-audible sonication on the wood pulp and ZnO sample. A diagram of the setup used for control experiment is shown in Figure 4.7.

A FB4417 2-mm microtip (Thermo Fisher Scientific, Waltham, MA, USA) attached to a CL-334 ultrasound converter (Thermo Fisher Scientific) of an FB705 Sonic Dismembrator (Thermo Fisher Scientific) was used to produce the continuous 20 kHz sound wave for these experiments. A clamp stand positioned below the microtip was used to hold the conical sample tube in a fixed position. A Leica DMIL LED inverted microscope (Leica Microsystems, Wetzlar, Germany) with an N PLAN 20× (NA 0.40, WD 0.39 mm) objective lens (Leica) was located nearby for sample observation pre- and post-sonication.

Before sonication, a small sample of wood pulp was removed from each sample vial using tweezers, placed on a microscope slide and preserved with cover slips. This was repeated twice for each sample. The remainder of each prepared sample, still contained in its resepctive preparation vial, was then in turn clamped into position, 12 mm below the end of the microtip. The sample was sonicated for 5 minutes on the 700 W power setting. Following this, a small sample was removed from each sonicated sample vial using tweezers, placed on a microscope slide and preserved with cover slips. This was also repeated twice for each sample. All preserved samples were then placed on the microscope in turn, with five images or regions of interest on the slide recorded for each slide.

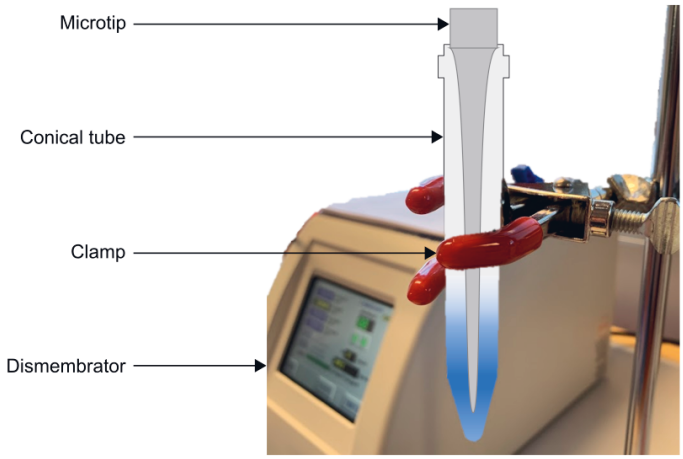

Figure 4.7 Labelled schematic of control experiment setup.

4.2.3 Image processing

Image processing was necessary to quantify the observed changes in antibubble behaviour for Studies II, IV, V, VII and VIII. The footage captured during the high-speed photography experiments were converted to greyscale images and used to observe and quantify the behaviours of antibubble, antibubble components or fragments and cells during sonication. MATLAB® (The MathWorks, In., Natick, MA, USA) software was used to create a partially-automated method of extracting the pixel size of given particles within each frame of the experiment's footage.

The initial step of this process involved the manual identification and labelling of each antibubble, antibubble component or fragment to be measured. Only particles that were fully in the field of view for at least the first cycle of sonication were considered for further processing.

Each frame had dimensions of 400 pixels in width and 250 pixels in height, with a micrometer to pixel ratio of 0.36:1. Before measurement of each particle commenced, the frames for a given experiment were cropped using the pixel coordinates around the given particle to reduce possible confusion of measurement values read in and to more easily identify the particle in question.

To segment the particle in each image from the background, the image was binarised, so that all pixels above a threshold value were made white, and all pixels below the threshold value were made black [66]. Otsu's method, a MATLAB® automatic

adaptive thresholding technique, was used to obtain the threshold value that would then be applied in the conversion of each image from greyscale to binary [59]. The grey-level window slicing technique is more robust and consistent than manually selecting the threshold value or measure the pixel size in each image by hand.

Otsu's method is a comprehensive one, as for a given image, the weight of the background and foreground distribution is calculated for each greyscale value. This is achieved by first counting the number of pixels above and below each given threshold value. The respective greyscale variance values and the weighted number of pixels in each range are then used to calculate the in-class variance

$$\sigma_{\mathrm{icv}} = \sqrt{{\sigma_{\mathrm{at}}}^2 \frac{N_{\mathrm{at}}}{N_{\mathrm{tot}}} + {\sigma_{\mathrm{bt}}}^2 \frac{N_{\mathrm{bt}}}{N_{\mathrm{tot}}}}\,, \tag{4.1}$$

where N_{at} is the number of pixels above threshold, N_{bt} is the number of pixels below threshold, N_{tot} is the total number of pixels in an image, σ_{at} is the variance above threshold, σ_{bt} is the variance below threshold, and σ_{icv} is the in-class variance. The threshold value with the least in-class variance is then selected as the final image threshold value [1], [59]. As the centre of the particles often contained darker pixels that were below the threshold and would thus be converted to black pixels, any black pixels that were completely surrounded by white pixels were converted to white pixels. Groups of white particles in contact with the border of the image were made black as at to be removed from the binary image. The BWLABEL MATLAB® function was then used to automatically identify and label groups of white connected pixels as numbered objects. Figure 4.8 depicts each step of the binarisation and labelling process for an example antibubble.

The area A of each particle was measured as the summation of white pixels within each identified object. From the area, the radius was calculated using the standard equation of a circle $R = \sqrt{\frac{A}{\pi}}$. The ratio of micrometer to pixel size was then used to calculate the radius of the particle in micrometers.

In instances where automatic thresholding did not work effectively, owing to a non-ideal weighted balance of pixels on either side of the greyscale value or non-uniform illumination across the frame, a threshold value was manually chosen. In stances were this too was not effective, the particle was measured manually across frames using the ruler measuring tool associated with the MATLAB® Image Processing Toolbox®. An example of such an instance would be the measurement of antibub-

ble fragments, where the fragments are too close to one another for the thresholding software to separate, but could still be visibly identified as separate particles.

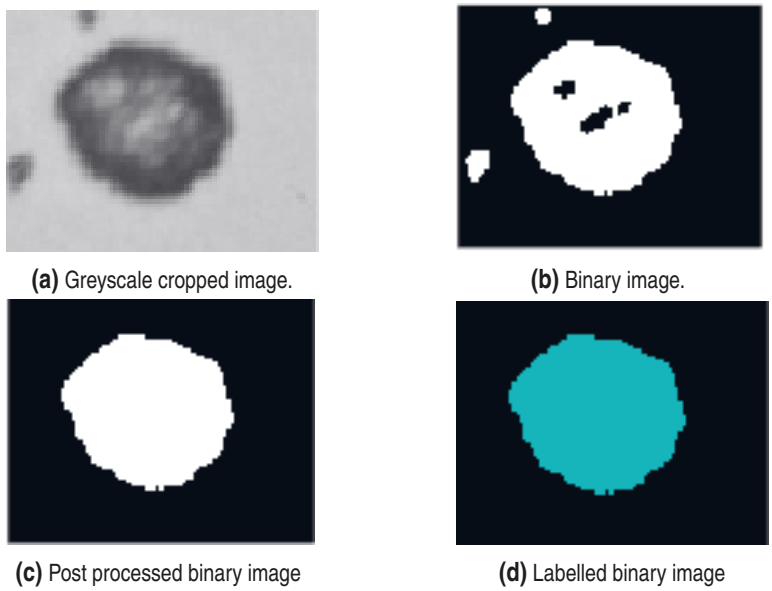

(a) Greyscale cropped image. **(b)** Binary image.

(c) Post processed binary image **(d)** Labelled binary image

Figure 4.8 Automated binarisation and labelling process for a given example antibubble. Re-drawn from [1].

A structured array was created containing the properties of each measured particle. The array fields included the particle name, its radius measured in each frame, particle type, ultrasound amplitude exposed to, the number of times the particle had been exposed to ultrasound, and the equilibrium, maximum, minimum and final radii. From these curves, more specific points of interest could be extracted. These included the initial resting radius R_0, maximum radius during first cycle $R_{\max}$, first minimum radius after transient phase $R_{\min}$ and the radius in the final frame R_{fin}.

4.2.4 Numerical computations and simulations

Studies III, IV, V, VI and VIII all involved simulation studies, for which a basic Rayleigh-Plesset with three additional parameters was used. These parameters were shell stiffness, antibubble-core radius, and a damping term. Additional terms discussed in literature that cannot be experimentally measured were excluded.

For computational purposes, a number of assumptions were made. The first being that the fluid surrounding the antibubble or antibubble component was considered to be an infinite viscous fluid. Additionally, the antibubble or antibubble component was assumed to be perfectly spherical with a homogeneous, elastic shell of infinitesimal thickness. Further, the following parameters were assumed constant in line with previous simulations in antibubble literature: $c = 1480\,\mathrm{m\,s^{-1}}$, equivalent to that of a saline solution [5], $C_\mathrm{p} = 1000\,\mathrm{J\,kg^{-1}\,K^{-1}}$, $K_\mathrm{g} = 0.025\,\mathrm{W\,m^{-1}\,K^{-1}}$, $p_0 = 1\,\mathrm{atm}$, $p_\mathrm{v} = 2.33\,\mathrm{kPa}$, $\gamma = 1.4$, $\eta = 1.00\,\mathrm{mPa\,s}$, $\rho = 998\,\mathrm{kg\,m^{-3}}$, $\rho_\mathrm{g} = 1.00\,\mathrm{kg\,m^{-3}}$, $\sigma = 0.072\,\mathrm{N\,m^{-1}}$, $\omega = 2\pi \times 1.0 \times 10^6\,\mathrm{rad\,s^{-1}}$.

Numerical solutions of (2.2) were computed using the `ode45` differential equation solver of MATLAB® (The MathWorks, Inc., Natick, MA, USA).

4.3 Study specific methods

4.3.1 Study II

To investigate the effect of the core on antibubble oscillation and stability, the ultrasound induced radial expansion and contraction of antibubbles, with and without core content, was compared. Antibubbles with and without core content were prepared as discussed in Section 4.1.1. They were then observed under sonication using the setup and procedure described in Section 4.2.1. A low acoustic amplitude of 200 kPa, and high acoustic amplitude of 1 MPa were used. The radii as a function of time were then extracted from experimental footage using the image processing technique presented in Section 4.2.3. From these curves, R_0, R_max and R_min during the first cycle were extracted and used to calculate the oscillation asymmetry ($\xi^+ - \xi^-$),

$$\xi^+ - \xi^- = R_\mathrm{max} + R_\mathrm{min} - 2R_0\,, \tag{4.2}$$

where ξ^+ and ξ^- represent positive and negative first cycle excursion respectively. The resulting asymmetry was then compared for antibubbles with and without cores. For the stability study, R_fin and R_0 of the antibubble with and without cores under only low-amplitude sonication were compared, as fragmentation was a common occurrence for those exposed to high-amplitude ultrasound.

4.3.2 Study III

Study III's purpose was to investigate the influence of endoskeletal friction on antibubble pulsation phase, relative to the sound wave. Numerical computations and simulations were performed to compute the damping coefficient terms and, from these, the pulsation phases for a range of antibubbles with resting radii between 0.5 and 12 μm and core radius ratios of 0.3 R_0 and 0.9 R_0. Assumed constants and parameter properties were in line with those presented in Section 4.2.4.

Thermal, viscous and re-radiation damping coefficient terms were computed using standard equations for shell-encapsulated microbubbles [13], [21], [47]. A summation of these terms was used to calculate the pulsation phase of a free gas bubble relative to a sound field. Damping owing to shell friction was calculated, with a friction assumed to be similar to that of lipid shells of 0.27 $\mu\mathrm{N\,s\,m^{-1}}$. A summation of the three above mentioned terms, with the addition of shell friction damping, was used to calculate the pulsation phase of a core-less antibubble relative to a sound field. Finally, the addition of the endoskeletal friction damping coefficient term was calculated and applied for the simulations of pulsation phase of antibubbles with cores, relative to a sound field. As the friction parameter of the endoskeletal damping term is directly proportional to the endoskeletal friction damping coefficient, and because little is known about the damping properties of the endoskeletal content, the whole endoskeletal damping term was made equal to the shell friction damping coefficient multiplied by a scalar value. From this, the effect of changing the endoskeletal friction damping coefficient relative to the shell friction damping coefficient could be understood. The scalar values used for this comparison were 0.3, 0.6, 0.9 and 2.

The phase difference α was calculated from the damping terms using [72]:

$$\alpha = \pi + \arctan\left(\frac{\left(\frac{\omega}{\omega_\mathrm{r}}\right)\delta}{1-\left(\frac{\omega}{\omega_\mathrm{r}}\right)^2}\right), \tag{4.3}$$

where ω_r is the angular resonance frequency of the respective bubble in radians, calculated from (2.3), ω is the angular centre frequency of the applied ultrasound in radians, and δ is the summation of the relevant damping coefficient terms.

4.3.3 Study IV

Study IV's purpose was to determine the shell stiffness of the Pickering-stabilised antibubble shell, which has, in first approach, been simplified by the χ parameter in (2.2). The shell stiffness parameter χ is considered both size and frequency independent. Only core-less antibubbles were considered in this study, so as to remove the influence of the antibubble core on the shell behaviour. Experimental data was compared to simulated data to find the shell stiffness. For the experimental data, antibubbles without core content were prepared as discussed in Section 4.1.1. These core-less antibubbles were then observed under sonication using the setup and procedure described in Section 4.2.1. A pressure pulse with a PNP of 200 kPa was used for this sample set. The radii as a function of time were then extracted from experimental footage using the image processing technique presented in Section 4.2.3. The R_0 and $R_{\max}$ during the first cycle for each $R(t)$ curve were then extracted. A least-squares fit through the measured $R_{\max}(R_0)$ scattered points was then done for later comparison to simulated data.

The Rayleigh-Plesset equation given in (2.2) was then used to simulate $R(t)$ curves for a single cycle of sonication for a range of initial radii and a range of χ values, from which R_0 and $R_{\max}$ were then extracted. The same pressure amplitude of 200 kPa was used for the simulations. For the computations, R_c was set to zero, with the addition of a damping term of $\delta\omega\rho R\dot{R}$. Damping owing to friction was not included in this study, as during the expansion phase a Pickering-stabilised interface can be regarded as frictionless, with constant surface tension [92]. A least-squares fit through the measured $R_{\max}(R_0)$ points for each χ was then done. The χ value of the fit with the closest match to that generated from the experimental data was selected. The $R_{\max}(R_0)$ scatter plot from the experimental data was then compared to $R_{\max}(R_0)$ simulated $R_{\max}(R_0)$ curve with the selected χ. For comparison purposes, the $R_{\max}(R_0)$ curve for a free gas bubble, with no shell stiffness was also included. Additionally, $R(t)$ curves extracted from experimental footage were compared to simulated $R(t)$ curves.

4.3.4 Study V

To determine the influence of high-amplitude sonication on Pickering-stabilised shell integrity, the radial pulsations of core-less antibubbles were extracted from experimental footage and numerical simulations. Antibubbles without core content were prepared as discussed in Section 4.1.1. These core-less antibubbles were then observed under sonication using the setup and procedure described in Section 4.2.1. A pressure pulse with a PNP of 1 MPa was used for this sample set. The radii as a function of time were then extracted from experimental footage using the image processing technique presented in Section 4.2.3. The R_0 and $R_{\max}$ during the first cycle for each $R(t)$ curve was then extracted. The Rayleigh-Plesset equation given in (2.2) was used to simulate $R(t)$ curves for a single cycle of sonication for a range of initial radii and χ values of 0 and 7.6 N m^{-1}, from which R_0 and $R_{\max}$ were then extracted. The same pressure amplitude of 1 MPa was used for the simulations. For the computations, R_c was set to zero, with the addition of a damping term of $\delta\omega\rho R\dot{R}$. Similarly to study IV, damping owing to friction was not included in this study, as during the expansion phase a Pickering-stabilised interface can be regarded as frictionless, with constant surface tension [92]. A scatter plot of the experimental $R_{\max}(R_0)$ points was compared to simulated $R_{\max}(R_0)$ curves.

4.3.5 Study VI

To predict the fragmentation threshold of antibubbles, numerical simulations of antibubble radial pulsation over time were computed for antibubbles with radii of 3 μm and core radius ratios of $0.3R_0$ and $0.9R_0$. The driving pressure amplitudes were varied to achieve a range of MI's of between 0 and 1, the frequencies of sonication were varied for a range between 0.5 and 15 MHz, and the shell stiffness (χ) was varied using values of 0 N m^{-1}, 1.1 N m^{-1}, 7.6 N m^{-1} and 15 N m^{-1}. A higher χ value might correspond to a greater amount of Pickering-stabilising material. From these computations, the time-variant kinetic energy of the shell and surface energy deficit was calculated. The fragmentation threshold for a given frequency was determined to be the MI at which the kinetic energy of the antibubble surpassed the surface energy of at least eight fragments ($\Delta E_k > \Delta E_s$). For the energy deficit calculations, (2.4) and (2.5) were used, assuming mode two oscillations.

4.3.6 Study VII

To determine antibubble fragment size distribution, high-speed video footage of antibubbles that had undergone explosive growth and then collapse during sonication were analysed as described in Section 4.2.3, and the resulting antibubble fragments counted. The fragment count and size distribution thereof was compared to a related study by Kooij *et al.* in which a larger sample of silica particles were found to have a predictable fragmentation size distribution [35].

4.3.7 Study VIII

To observe antibubbles in the presence of biological cells during sonication, high-speed footage of hydrophobic ZnO particles in the presence of wood cells during sonication were captured and analysed. The samples were prepared as described in Section 4.1.2, with experiments being conducted as described in Section 4.2 at a PNP of 1.3 MPa. To ensure that the wood cells and ZnO used could be compared to those used in previous studies, a control experiment at near audible range was also done. For the control experiment, the experimental setup and procedure described in Section 4.2.2 was followed.

5 RESULTS

A representative summary of the results across all studies in this body of research is given in this chapter.

Figures 5.1 and 5.2 summarise the results of Study II. The oscillation asymmetry of antibubbles, with and without core content, during the first cycle of ultrasound at pressure amplitudes of 200 kPa and 1 MPa is presented in Figure 5.1. The lasting impact of exposure to a single ultrasound pulse with a pressure amplitude of 200 kPa, on antibubbles with and without core content is shown in Figure 5.2.

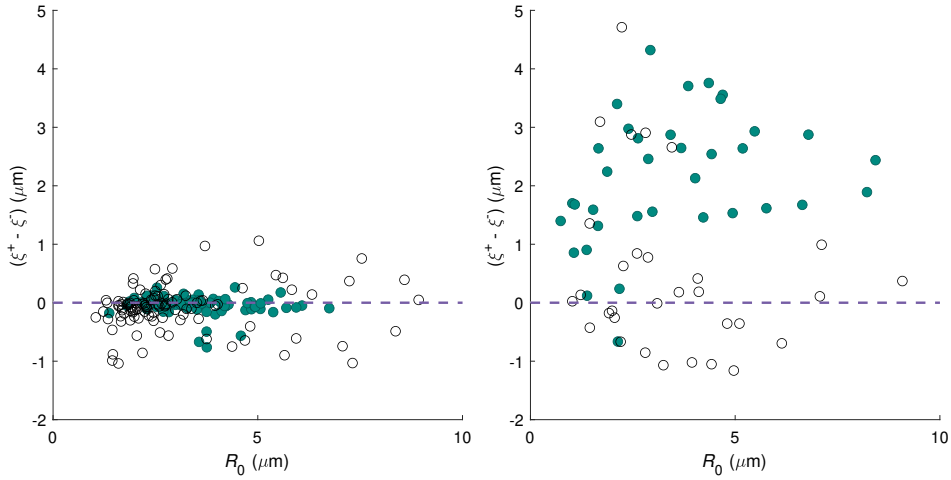

(a) 200 kPa **(b)** 1 MPa

Figure 5.1 Scatter plot of initial resting radius (R_0) versus oscillation asymmetry ($\xi^+ - \xi^-$) as a result of a single cycle of ultrasound at pulse pressure amplitudes of 200 kPa (a) and 1 MPa (b) for antibubbles with cores (●) and without (○). The dotted purple line (- -) represents perfectly symmetrical excursion, where ($\xi^+ - \xi^-$) = 0. Re-drawn from [II].

The distribution of antibubbles both with and without core content in Figure 5.1a appears to be evenly spread across the line of symmetry when exposed to low-amplitude sonication. Average oscillation asymmetry values of −0.0 and −0.1 were calculated for antibubbles with and without cores respectively. Figure 5.1b demon-

strates that under sonication at a higher amplitude of 1 MPa, core-containing antibubbles oscillate significantly less evenly across the line of symmetry than core-less antibubbles, with measured average oscillation asymmetry values of 2.2 and 0.9 respectively. Figure 5.2 shows that $R_{\mathrm{fin}}(R_0)$ data points for antibubbles with cores deviate less from the $R_{\mathrm{fin}} = R_0$ line than antibubbles without cores.

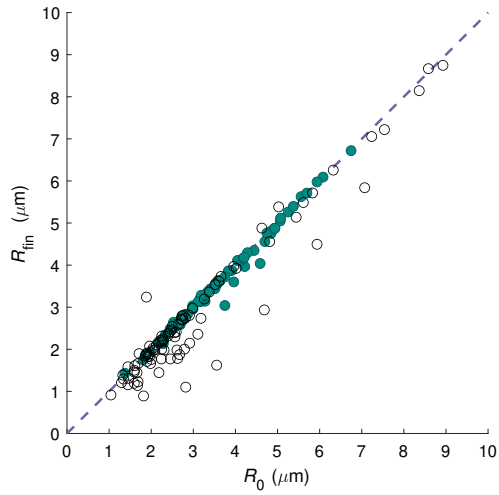

Figure 5.2 Scatter plot of final radius (R_{fin}) as a function of initial resting radius (R_0) of antibubbles with (●) and without cores (○) after a single ultrasound pulse with a pressure amplitude of 200 kPa. The dotted purple line (- -) represents $R_{\mathrm{fin}} = R_0$. Re-drawn from [2].

The simulated results of Study III's pulsation phase relative to the incident sound wave of antibubbles of varying sizes, with core radius ratios of $0.3R_0$ and $0.9R_0$, are presented in Figures 5.3a and 5.3b respectively. The pulsation phase of the free gas bubble and core-less antibubble are identical across both graphs as they contain no cores and thus are unaffected by the change in core radius ratio. If only antibubbles containing cores are considered, it is clear that, as the damping owing to endoskeletal friction is increased, so too is the pulsation phase relative the sound field, irrespective of the core radius ratio. When comparing the respective phase differences of the simulated curves for antibubbles with core radius ratios of $0.3R_0$ to that of a free gas bubble, only antibubbles with a resting radius of less than 3 μm can be easily differentiated from free gas bubbles. When the core radius ratio is increased to $0.9R_0$, antibubbles with a resting radius of less than 1.5 μm as well as those with a resting radius of between 3 and 8 μm can be easily differentiated from free gas bubbles.

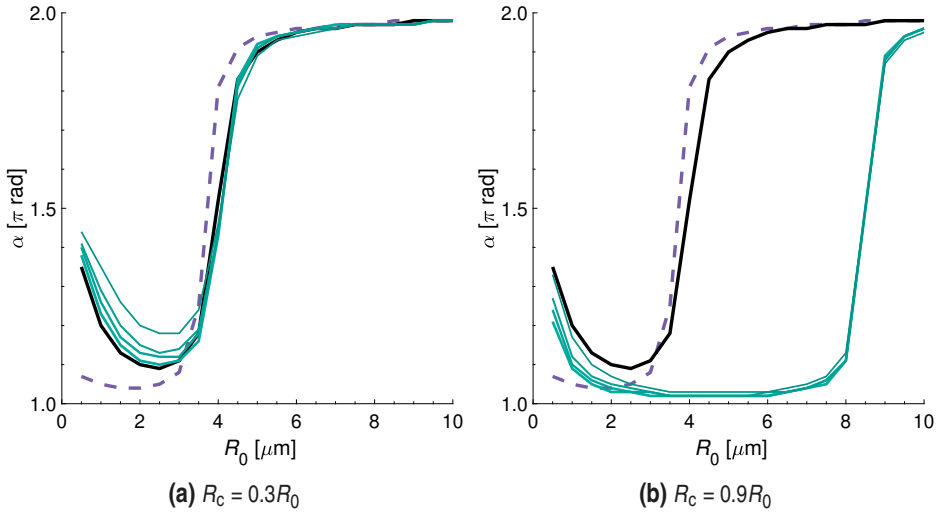

Figure 5.3 Pulsation phase with respect to incident sound field as a function of R_0 for a free gas bubble (- -), an antibubble with no core (–), and antibubbles with core content having endoskeletal damping coefficients equal to 0.3 (–), 0.6 (–), 0.9 (–) and 2 (–). Re-drawn from [III].

The results of Studies IV and V, which centre around the properties and effects of the antibubble shell, are presented in Figure 5.4. Through the iterative curve fitting methods described in Section 4.3.3, a shell stiffness of $7.6\,\mathrm{N\,m^{-1}}$ was found for core-less antibubbles. Figure 5.4a shows the simulated $R_{\max}(R_0)$ curve for a core-less antibubble with this given shell stiffness, as well as that of a free gas bubble with no shell stiffness, against the scattered $R_{\max}(R_0)$ points obtained from experimental footage of core-less antibubbles under sonication at a pressure amplitude of 200 kPa. Figure 5.4b shows the same comparison curves and data points, for bubbles exposed to ultrasound with a pressure amplitude of 1 MPa.

Under the 200-kPa regime, more than 90% of the $R_{\max}(R_0)$ experimental points fit the $R_{\max}(R_0)$ simulated curve of a core-less antibubble with a shell stiffness of $7.6\,\mathrm{Nm^{-1}}$ plotted in Figure 5.4a. Under the 1-MPa regime, 40% of the $R_{\max}(R_0)$ experimental points plotted fit the $R_{\max}(R_0)$ simulated curve of a core-less antibubble shown in Figure 5.4b, with the remainder experiencing considerably larger expansion. Three core-less antibubbles appeared to expand similarly to free gas bubbles of the same size.

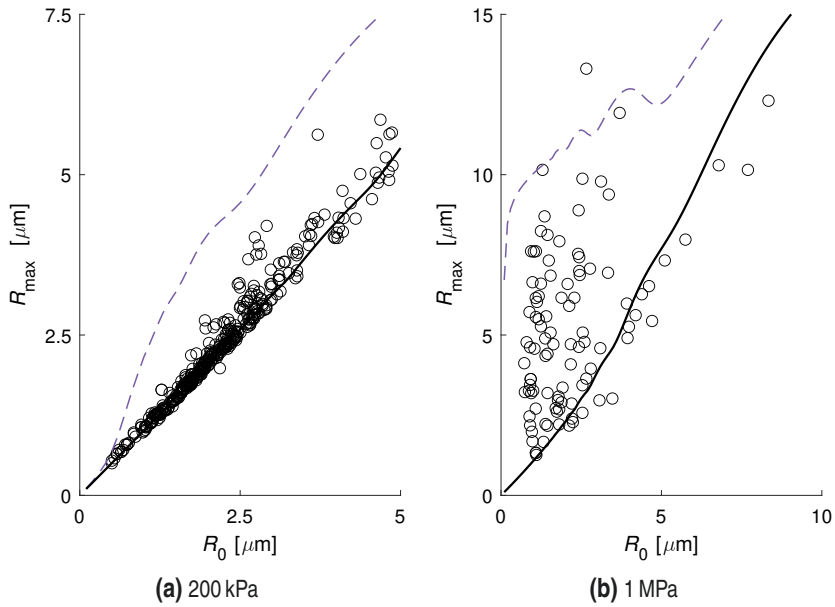

Figure 5.4 Scatter plot of R_0 vs R_{max} (○) for a core-less antibubble during the first cycle of sonication at sonication amplitudes of (a) 200 kPa and (b) 1 MPa. Simulated $R_{max}(R_0)$ curves of a core-less antibubble (–) and a free gas bubble (- -) are overlain. Re-drawn from [IV],[V].

Figure 5.5 illustrates the findings of Study VI, in which the effect of varying material properties of antibubble components on the fragmentation threshold of antibubbles is investigated. Regardless of the core radius ratio, Figure 5.5 demonstrates that increasing shell stiffness increases the frequency at which the fragmentation threshold is at a minimum. The frequency at which the minimum fragmentation threshold can be found is lowest for antibubbles with no shell stiffness, and highest for those with the maximum shell stiffness investigated here of $15\,\mathrm{N\,m^{-1}}$. The impact of the internal core size appears to increase with shell stiffness, as demonstrated when comparing curves of the same shell stiffness across Figures 5.5a and 5.5b. When the core radius ratio is increased from 0.3 to $0.9R_0$, the frequency at which the lowest MI is observed shifts from 1 to 2.5 MHz for a χ of $0\,\mathrm{N\,m^{-1}}$, from 1 to 2 MHz for a χ of $1.1\,\mathrm{N\,m^{-1}}$, from 3.5 to 4.5 MHz for a χ of $7.6\,\mathrm{N\,m^{-1}}$, and from 4.5 to 5 MHz for a χ of $15\,\mathrm{N\,m^{-1}}$.

Figure 5.6 shows the size distribution of a 20 μm antibubble, 1 minute after sonication determined for Study VII. The fragmentation size distribution was found to fit an exponential curve. This is in line with the predictable fragment size distribution of larger silica particles [35].

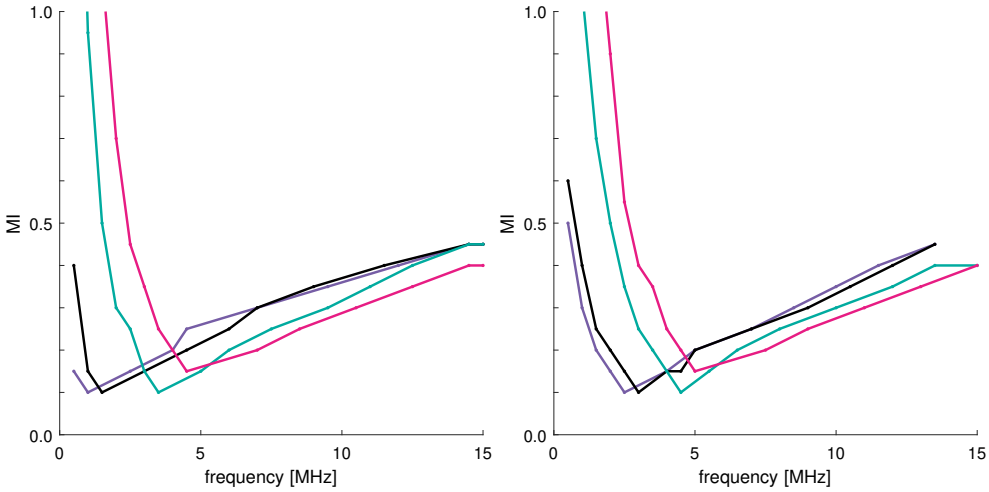

(a) $R_c = 0.3R_0$ **(b)** $R_c = 0.9R_0$

Figure 5.5 Simulated fragmentation threshold, expressed in MI, as a function of frequency for a 3 μm antibubble with χ = 0 N m^{-1} (–), χ = 1.1 Nm^{-1} (–), χ = 7.6 N m^{-1} (–), and χ = 15 N m^{-1} (–), with core radius ratios of $R_c = 0.3R_0$ (a) and $R_c = 0.9R_0$ (b). Re-drawn from [VI].

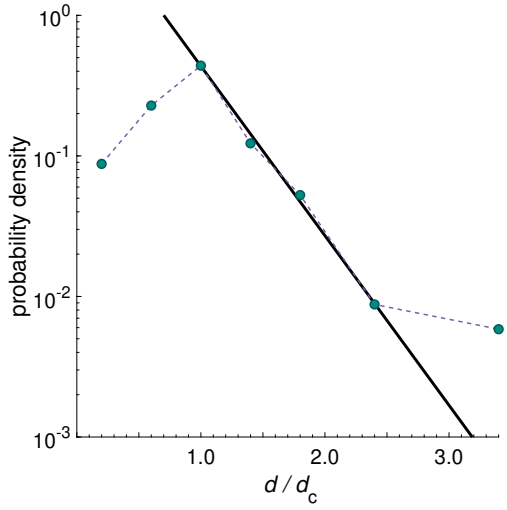

Figure 5.6 Fragment size distribution of a 20 μm antibubble 1 minute after sonication, normalised by the characteristic fragmentation diameter of d_c = 2.5 μm (- -), with an exponential distribution fit, $P(d) = Ce^{d/d_1}$, overlain (–). Re-drawn from [VII].

Figure 5.7 shows the behaviour of a cluster of hydrophobic ZnO particles in the vicinity of wood cells, observed during the investigation of Study VIII. The ZnO cluster was observed to nucleate, and subsequently collapse near a wood fibre cell wall while forming a liquid jet. This jet passed through the wall of the wood fibre cell, without visibly destroying the internal cellular structure. Whilst not shown here, the results of the control experiment confirmed that cell destruction occurred at the near-audible 20 kHz.

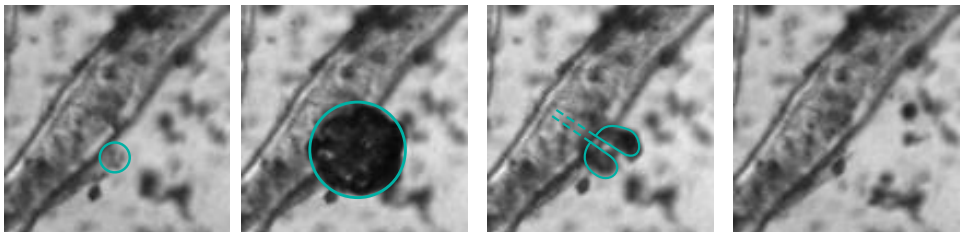

Figure 5.7 Image sequence of hydrophobic ZnO particles and wood cells under sonication, in which the response of a hydrophobic ZnO cluster (circled ○) subjected to a pressure pulse with a PNP of 1.3 MPa can be observed in the presence of wood cells. The images show the ZnO cluster before nucleation (a), at maximum radius size (b), at collapse during the formation of a liquid jet (c), and the intact wood fibre cells after being jetted through (d). Re-drawn from [VIII].

6 DISCUSSION

This research comprised a number of studies with the unified aim of better defining the dynamic response of Pickering-stabilised antibubbles to pulsed ultrasound, and furthering what is known about the role that each component plays in that behaviour. The aims, methods used to achieve them, results, learnings, and implications thereof are discussed in this Chapter.

The aim of Study I was to identify and understand the limitations of the effect of ultrasound on cell behaviour, and how this work adds value to the field of medical ultrasonics. A literature study resulted in the publication of a review article, [I], as well as the introduction and background of this dissertation. The majority of the studies in which the direct effect of ultrasound on cells is observed are done well above the cavitation threshold, with little response noted at safer MIs. This confirms that currently clinically safe ultrasound cannot be used alone to manipulate or destroy specifically targeted cells, and that a catalyst, such as an antibubble, is required to amplify the destructive effect of ultrasound on cells.

Studies II - VIII involved the experimental observation and simulation of antibubbles with and without cores, free gas bubbles, ZnO and wood fibre cells. It should be noted that core-less antibubbles mentioned throughout this dissertation are referred to as reference (REF) bubbles in publication II and Pickering-stabilised microbubbles in publications IV and V. This naming convention allowed for these studies to be better understood independently, as Pickering-stabilised microbubbles may have applications other than in theranostics. However, as the aim of this dissertation, involved understanding the effect of the antibubble core as a component of a Pickering-stabilised antibubble on its oscillation dynamics, the term "core-less antibubbles" made for simpler comparison throughout this dissertation.

The second aim was to determine the effect of the antibubble core on its oscillation dynamics. Figure 5.1 shows that first-cycle core-containing antibubble contractions and expansions were spherically symmetrical and predictable at an acoustic amplitude of 200 kPa. Core-containing antibubble pulsations were more asymmetrical than that of their core-less counterparts at an acoustic amplitude of 1 MPa. Figure 5.2 shows that after sonication at an acoustic amplitude of 200 kPa, core-containing antibubbles shrank less than those without cores. These results indicate that the presence of the core inside of the antibubble hampers the contraction of a collapsing antibubble and ameliorates its stability. A premature explanation for the shrinking observed would be the rearranging or packing of particles within the solid shell, since this process takes only three microseconds, whereas dissolution would take milliseconds. Desorption of particles from the shell would not differ between microbubbles and antibubbles, and is therefor not thought to be the dominant mechanism in shrinking. This spherically asymmetric behaviour of antibubbles under sonication at an acoustic amplitude of 1 MPa indicates that Pickering-stabilised antibubbles may be more feasible candidates for ultrasonic imaging than the agents currently in use, with greater stability and longer maximum exposure times. The acoustic regime, with an MI of 1, at which this asymmetry was noted however, is not in the ideal safety range and further studies closer to a threshold pressure for asymmetry would be needed. Understanding the effect of various component material properties on the overall oscillation dynamics of antibubbles could allow for the creation of an antibubble that exhibits this dynamic spherical asymmetry when exposed to ultrasound with a lower MI. The differing size disruption of antibubbles with and without cores is another point to note. Further studies with a larger and more evenly distributed population of antibubbles with and without core content should follow to confirm the results obtained here. The effect of the antibubble core on its oscillation dynamics was met through observing and quantifying the oscillation of antibubbles with and without core content.

The third aim was to determine the influence of endoskeletal friction on antibubble pulsation phase relative to the applied sound field. This was achieved by observing the effect of different shell and endoskeletal damping coefficient ratios on the phase difference relative to the incident sound field in simulation. The initial radius at which the sharp gradient of the curves in Figure 5.3 occurs coincides with the resonance size of the given antibubble or free gas bubble. As the damping coefficient

is increased, so too is the resonance size for a given frequency. It can also be said that increasing the damping coefficient will increase the resonance frequency of an antibubble. Studying the curves for a free gas bubble and a core-less antibubble in Figure 5.3 reveals the impact of shell friction on pulsation phase. Of the antibubbles with an initial radius of less than 3μm investigated, a pulsation phase difference of up to $\frac{1}{6}^{\text{th}}$ of a cycle with respect to free gas bubbles was found. The shell damping term appears to dominate the pulsation phase when the initial radii is below $3\,\mu$m, followed by the viscous damping term. When the core-containing antibubbles with a core radius ratio of $0.3R_0$ are included in the comparison to free gas bubbles, the same shell damping component dominance is clear for bubbles smaller than $3\,\mu$m. This changes when the core-containing antibubbles with a core radius ratio of $0.9R_0$, are considered. The shell damping component only dominates the pulsation phase difference for antibubbles with initial radii of below $1.5\,\mu$m, and the endoskeletal friction component dominates for antibubbles with initial radii between 4 and $8\,\mu$m. These differences can be attributed not only to the effect of differing frictional damping components, but also to the effect of core size on the thermal damping coefficient. As the core size changes, so too does the volume of gas in the antibubble. Since this dissertation is primarily focused on antibubbles for their use in medical applications, the results for antibubbles with initial resting radii less than $3\,\mu$m are more relevant, as larger entities cannot be safely injected into the blood stream, given that the lowest capillary radius is $3\,\mu$m. However, the pulsation phase difference for antibubbles with larger initial radii could prove useful in other applications. The findings would also prove useful in particle sizing applications and identifying whether there is core content present.

These results indicate that altering the damping of the shell or skeletal material of minute antibubbles can alter the degree to which a particle oscillates in phase with the sound field. An additional implication of these results is that, when given a wide range of antibubbles of varying sizes, the resonance frequency of the antibubbles can be determined. It can also be inferred that, if the antibubble concentration is too high, the oscillation of bubbles near one another may cancel out the applied ultrasound. These results clearly provide valuable insight into the effect of the damping owing to the friction of the shell and endoskeletal material used. To further this research, these simulated results should be compared to experimental data. Experiments involving antibubbles with known differing material properties could also be

used to further confirm the relationships observed in simulation. A limitation of this study is that the differing shell and endoskeletal content dynamics are not considered here, as they are not known. Further analysis of experimental results and a more complex model may be required to take these dynamics into account. The effect of additional properties such as shell thickness should also be addressed in future investigations.

The main aim of Study IV was to determine the shell stiffness of an antibubble. The shell stiffness of Pickering-stabilised antibubbles without incompressible contents was determined to be $7.6\,\mathrm{N\,m^{-1}}$ throughout low-amplitude sonication. Figure 5.4a presents a curve where over 90% of maximal radial expansions experimentally observed agree with those predicted in simulation for a core-less antibubble with a shell stiffness of $7.6\,\mathrm{N\,m^{-1}}$. This is a high shell stiffness, which further supports the stability and oscillation symmetry at low amplitudes observed experimentally during Study II. This shell stiffness is similar to that of albumin shelled microbubbles, which are commonly used as ultrasound contrast agents. It is thus reasonable to expect other similar phenomenal observed in albumin contrast agents, such as sonic cracking, to occur.

Only core-less antibubbles were considered for this study, to remove the influence of the antibubble core on the shell behaviour. This is a limiting factor, as Study III indicated that the effect of the core on the shell behaviour cannot be completely ignored. Additionally, only results during the first cycle of ultrasound were considered, so that the higher-order effects, such as the viscoelasticity of surrounding antibubbles, could be ignored in simulation. Studying these effects experimentally would enable them to be incorporated into a model, allowing the effects of longer periods of sonication to be predicted. Owing to the fact that this work required the analysis of 2D footage of 3D phenomena, a relatively simple Rayleigh-Plesset equation was used for the simulations. Comparisons of the radius-time curves for simulated and experimental data, an example of which is provided in [IV], indicate the validity of the shell stiffness approximation, as well as the choice of equations used in the simulation.

The aim of Study V was to determine the influence of high-amplitude sonication on Pickering-stabilised shell integrity. Under high-amplitude sonication, Figure 5.4b shows that the maximum expansions of core-less antibubbles, measured from high-

speed camera footage, were either agreeing with those computed for Pickering-stabilised core-less antibubbles or corresponding to greater values. Two example comparisons of the radius-time curves for simulated and experimental data are provided in [V]. In the first, the experimentally observed radius-time curve matches that of a core-less antibubble with a shell stiffness of $7.6\,\mathrm{N\,m^{-1}}$. The second radius-time curve follows that of a simulated free gas bubble, suggesting that the shells may have cracked. However, gas release was not observed for either bubble. This may indicate that the difference in expansion could be the result of the Picking-stabilising nanoparticles being non-uniformly distributed. These findings indicate that a change in behaviour of the shell did occur during high-amplitude sonication. This is a promising result when considering antibubbles for targeted drug release. The fact that less of the experimental data points fit the simulated antibubble curve when exposed to high amplitude ultrasound than low amplitude ultrasound, may indicate limitations in the simulation's ability to predict oscillation at higher amplitudes. Another limiting factor of this study is that only antibubbles without cores were considered, and that the core may influence the expansion of the antibubble shell.

The aim of Study VI was to predict the fragmentation threshold of antibubbles. To do this, the fragmentation threshold of a 3μm radius antibubble with varying component properties was simulated. Four shell stiffness values were considered in this study; $0\,\mathrm{N\,m^{-1}}$ for comparison to a shell-less antibubble, $1.1\,\mathrm{N\,m^{-1}}$ for comparison to a lipid-shelled antibubble, $7.6\,\mathrm{N\,m^{-1}}$ for comparison to the previously computed antibubble shell stiffness and $15\,\mathrm{N\,m^{-1}}$ for comparison to an, unlikely, very stiff-shelled antibubble. The wide range allowed for the observation of the trends in threshold change with stiffness. Figure 5.5 shows that the frequency at which the MI of fragmentation is at a minimum for an antibubble increases with increasing shell stiffness. The frequency at which the MI of fragmentation is at a minimum corresponds to the resonance frequency of the given antibubble. It follows that shell stiffness influences the resonance frequency of an antibubble, which in turn influences its fragmentation threshold. Figure 5.5 also shows that the frequency at which the fragmentation threshold is lowest for a given antibubble appears to increase as the core radius ratio is increased. These findings indicate that, as the rigidity of the antibubble is increased, either through the addition of core content or through a stiffer shell, the instantaneous velocity of the bubble-liquid interface during excursion decreases, reducing the kinetic energy of the shell. Figure 5.5 additionally shows

that, when exposed to driving frequencies above 1 MHz, the antibubble fragmentation threshold was computed to correspond to a mechanical index of less than 0.5, irrespective of shell stiffness. This indicates that antibubble fragmentation for the purposes of drug release at medically safe ultrasound amplitudes is feasible. It was noted that larger excursions were only observed for bubbles of initial radii less than resonant radius of a free gas bubble.

An antibubble with initial resting radius of 3 μm was chosen for this study, as this would be an ideal size for drug delivery. Additionally this was the mean antibubble size observed in a previous study [60]. Repeating the study for antibubbles of different initial resting radii would be of great value. The effect of additional parameters, such as damping, could yield information of significant value too. To further this research, the results presented should be compared to those experimentally observed during antibubble fragmentation. The implementation of a machine learning model with variability of all parameters discussed, and experimental fragmentation data functioning as training data, would be an exciting and efficient way to first validate and then optimise the Rayleigh-Plesset equation model used.

The aim of Study VII was to determine antibubble fragment size distribution. An exponential fragment size distribution was found for an antibubble with initial radius of 20 μm. This indicates that the sound field creates an exponential distribution for antibubbles, and not a power one. Whilst this does match the results for larger particle populations previously published, a greater sample size should be considered to further validate the results. The result gives insight into antibubble disruption and moves us closer to controlling the material release for these particles. If the pressure of the regime is known, the number of antibubble fragments produced can be theoretically determined. The reverse could also be true, where the fragmentation size distribution, post sonication, could be used to determine the pressure at time of fragmentation.

The aim of Study VIII was to observe antibubble core content in the presence of biological cells during sonication. Under high-amplitude ultrasound exposure, a cluster of hydrophobic ZnO particles, a common component of antibubble cores, were observed to jet through a wood fibre cell wall without causing visible damage to the internal cellular structure. Prior to disruption, the hydrophobic particles near the cell wall behaved similarly to a Pickering-stabilised antibubble under sonica-

tion. Thus, hydrophobic particles can act as inertial cavitation nuclei, which collapse asymmetrically close to solid boundaries such as wood pulp fibres. This indicates that hydrophobic particles, on their own, can be used to create holes though cell walls. While formation of the jet through the fibre wall was noted, no re-sealing of the wall could be identified and thus the sonoporation potential of ZnO hydrophobic particles cannot be confirmed. The ability to create pores in solid boundaries such as wood fibre cell walls indicates that the hydrophobised particles may have a role to play in trans-dermal drug delivery. Drugs encapsulated by a layer of hydrophobised particles may prove to be promising theranostic agent alternatives.

7 CONCLUSION

The summation of these studies served the common purpose of predicting the dynamic behaviour of Pickering-stabilised antibubbles. The effect of shell stiffness, core volume ratio and the damping coefficient of these components on Pickering-stabilised antibubble dynamics under theranostic ultrasound conditions has been identified and quantified. This work brings us a step forward in determining the elasto-mechano properties of small samples of contrast agent and gives insight into the theranostic potential of antibubbles. Whilst possessing some theranostic properties, Pickering-stabilised antibubbles may be more suitable as replacements for current diagnostic agents. Hydrophobising drugs themselves may be a more apposite and simple theranostic alternative. The potential to adapt certain properties of the respective antibubble components may still make them suitable candidates for theranostic drug delivery.

REFERENCES

[1] N. Anderton, "Acoustic properties of antibubbles," MSc Dissertation, University of the Witwatersrand, Johannesburg, 2020.

[2] N. Anderton, C. S. Carlson, R. Matsumoto, R. Shimizu, A. T. Poortinga, N. Kudo, and M. Postema, "Sonic shrinking of Pickering-stabilised ultrasound contrast agent at a low acoustic amplitude," *Proceedings of the 42nd Symposium on UltraSonic Electronics*, 2E4–4, 2021.

[3] R. E. Apfel and C. K. Holland, "Gauging the likelihood of cavitation from short-pulse, low-duty cycle diagnostic ultrasound," *Ultrasound in Medicine & Biology*, vol. 17, no. 2, pp. 179–185, 1991.

[4] British Medical Ultrasound Society, "Guidelines for the safe use of diagnostic ultrasound equipment," *Ultrasound*, vol. 18, no. 2, pp. 52–59, 2010.

[5] C. S. Carlson, A. Deroubaix, C. Penny, and M. Postema, "On the attenuation of ultrasound by pure black tattoo ink," *SAIEE Africa Research Journal*, vol. 112, no. 1, pp. 24–31, 2021.

[6] E. L. Carstensen, P. Kelly, C. C. Church, A. A. Brayman, S. Z. Child, C. H. Raeman, and L. Schery, "Lysis of erythrocytes by exposure to CW ultrasound," *Ultrasound in Medicine & Biology*, vol. 19, no. 2, pp. 147–165, 1993.

[7] M. Chan and K. Soetanto, "Study on contrast effect of microbubbles as ultrasound contrast agents," *Japanese Journal of Applied Physics*, vol. 37, no. 5B, pp. 3078–3081, 1998.

[8] C. C. Church, "The effects of an elastic solid surface layer on the radial pulsations of gas bubbles," *The Journal of the Acoustical Society of America*, vol. 97, no. 3, pp. 1510–1521, 1995.

[9] A. H. Churchman, V. Mico, J. G. de Pablo, S. A. Peyman, S. Freear, and S. D. Evans, "Combined flow-focus and self-assembly routes for the formation of lipid stabilized oil-shelled microbubbles," *Microsystems & Nanoengineering*, vol. 4, 17087, 2018.

[10] D. Dalecki, "Mechanical bioeffects of ultrasound," *Annual Review of Biomedical Engineering*, vol. 6, pp. 229–248, 2004.

[11] P. A. Dayton, K. E. Morgan, A. L. Klibanov, G. Brandenburger, K. R. Nightingale, and K. W. Ferrara, "A preliminary evaluation of the effects of primary and secondary radiation forces on acoustic contrast agents," *IEEE Transactions on Ultrasonics, Ferroelectrics, and Frequency Control*, vol. 44, no. 6, pp. 1264–1277, 1997.

[12] T. Dehoux, M. A. Ghanem, O. F. Zouani, J.-M. Rampnoux, Y. Guillet, S. Dilhaire, M.-C. Durrieu, and B. Audoin, "All-optical broadband ultrasonography of single cells," *Scientific Reports*, vol. 5, 8650, 2015.

[13] C. Devin Jr., "Survey of thermal, radiation, and viscous damping of pulsating air bubbles in water," *The Journal of the Acoustical Society of America*, vol. 31, no. 12, pp. 1654–1667, 1959.

[14] S. Dicker, M. Mleczko, M. Siepmann, N. Wallace, Y. Sunny, C. R. Bawiec, G. Schmitz, P. Lewin, and S. P. Wrenn, "Influence of shell composition on the resonance frequency of microbubble contrast agents," *Ultrasound in Medicine & Biology*, vol. 39, no. 7, pp. 1292–1302, 2013.

[15] A. A. Doinikov, "Equations of coupled radial and translational motions of a bubble in a weakly compressible liquid," *Physics of Fluids*, vol. 17, no. 12, 128101, 2005.

[16] A. A. Doinikov and A. Bouakaz, "Review of shell models for contrast agent microbubbles," *IEEE Transactions on Ultrasonics, Ferroelectrics, and Frequency Control*, vol. 58, no. 5, pp. 981–993, 2011.

[17] A. A. Doinikov and P. A. Dayton, "Maxwell rheological model for lipid-shelled ultrasound microbubble contrast agents," *The Journal of the Acoustical Society of America*, vol. 121, no. 6, pp. 3331–3340, 2007.

[18] B. Dollet, P. Marmottant, and V. Garbin, "Bubble dynamics in soft and biological matter," *Annual Review of Fluid Mechanics*, vol. 51, pp. 331–355, 2019.

[19] S. Dorbolo, H. Caps, and N. Vandewalle, "Fluid instabilities in the birth and death of antibubbles," *New Journal of Physics*, vol. 5, no. 1, 161, 2003.

[20] V. R. Dugyala, S. V. Daware, and M. G. Basavaraj, "Shape anisotropic colloids: synthesis, packing behavior, evaporation driven assembly, and their application in emulsion stabilization," *Soft Matter*, vol. 9, no. 29, pp. 6711–6725, 2013.

[21] A. I. Eller, "Damping constants of pulsating bubbles," *The Journal of the Acoustical Society of America*, vol. 47, no. 5B, pp. 1469–1470, 1970.

[22] T. Faez, M. Emmer, K. Kooiman, M. Versluis, A. F. W. van der Steen, and N. de Jong, "20 years of ultrasound contrast agent modeling," *IEEE Transactions on Ultrasonics, Ferroelectrics, and Frequency Control*, vol. 60, no. 1, pp. 7–20, 2013.

[23] L. B. Feril Jr., T. Kondo, Y. Tabuchi, R. Ogawa, Q.-L. Zhao, T. Nozaki, T. Yoshida, N. Kudo, and K. Tachibana, "Biomolecular effects of low-intensity ultrasound: apoptosis, sonotransfection, and gene expression," *Japanese Journal of Applied Physics*, vol. 46, no. 7S, pp. 4435–4440, 2007.

[24] P. J. A. Frinking, N. de Jong, and E. I. Céspedes, "Scattering properties of encapsulated gas bubbles at high ultrasound pressures," *The Journal of the Acoustical Society of America*, vol. 105, no. 3, pp. 1989–1996, 1999.

[25] Global Burden of Disease 2019 Cancer Collaboration, "Cancer incidence, mortality, years of life lost, years lived with disability, and disability-adjusted life years for 29 cancer groups from 2010 to 2019: a systematic analysis for the global burden of disease study 2019," *JAMA Oncology*, vol. 8, no. 3, pp. 420–444, 2022.

[26] G. ter Haar, "HIFU tissue ablation: concept and devices," *Advances in Experimental Medicine and Biology*, vol. 880, pp. 3–20, 2016.

[27] P. Heppner and J. R. Lindner, "Contrast ultrasound assessment of angiogenesis by perfusion and molecular imaging," *Expert Review of Molecular Diagnostics*, vol. 5, no. 3, pp. 447–455, 2005.

[28] S. Hernot and A. L. Klibanov, "Microbubbles in ultrasound-triggered drug and gene delivery," *Advanced Drug Delivery Reviews*, vol. 60, no. 10, pp. 1153–1166, 2008.

[29] W. Hughes and A. R. Hughes, "Liquid drops on the same liquid surface," *Nature*, vol. 129, no. 3245, p. 59, 1932.

[30] K. Johansen, E. Kimmel, and M. Postema, "Theory of red blood cell oscillations in an ultrasound field," *Archives of Acoustics*, vol. 42, no. 1, pp. 121–126, 2017.

[31] K. Johansen, S. Kotopoulis, and M. Postema, "Ultrasonically driven antibubbles encapsulated by Newtonian fluids for active leakage detection," *Lecture Notes in Engineering and Computer Science*, vol. 2216, 2015.

[32] K. Johansen and M. Postema, "Lagrangian formalism for computing oscillations of spherically symmetric encapsulated acoustic antibubbles," *Hydroacoustics*, vol. 19, pp. 197–207, 2016.

[33] N. de Jong, R. Cornet, and C. T. Lancée, "Higher harmonics of vibrating gas-filled microspheres. Part one: simulations," *Ultrasonics*, vol. 32, no. 6, pp. 447–453, 1994.

[34] S. S. Kelkar and T. M. Reineke, "Theranostics: combining imaging and therapy," *Bioconjugate Chemistry*, vol. 22, no. 10, pp. 1879–1903, 2011.

[35] S. Kooij, G. van Dalen, J.-F. Molinari, and D. Bonn, "Explosive fragmentation of Prince Rupert's drops leads to well-defined fragment sizes," *Nature Communications*, vol. 12, 2521, 2021.

[36] K. Kooiman, S. Roovers, S. A. Langeveld, R. T. Kleven, H. Dewitte, M. A. O'Reilly, J.-M. Escoffre, A. Bouakaz, M. D. Verweij, K. Hynynen, I. Lentacker, E. Stride, and C. K. Holland, "Ultrasound-responsive cavitation nuclei for therapy and drug delivery," *Ultrasound in Medicine & Biology*, vol. 46, no. 6, pp. 1296–1325, 2020.

[37] S. Kotopoulis, G. Dimcevski, O. Helge Gilja, D. Hoem, and M. Postema, "Treatment of human pancreatic cancer using combined ultrasound, microbubbles, and gemcitabine: a clinical case study," *Medical Physics*, vol. 40, no. 7, 072902, 2013.

[38] S. Kotopoulis, K. Johansen, O. H. Gilja, A. T. Poortinga, and M. Postema, "Acoustically active antibubbles," *Acta Physica Polonica A*, vol. 127, no. 1, pp. 99–102, 2015.

[39] S. Kotopoulis, C. Lam, R. Haugse, S. Snipstad, E. Murvold, T. Jouleh, S. Berg, R. Hansen, M. Popa, E. Mc Cormack, *et al.*, "Formulation and characterisation of drug-loaded antibubbles for image-guided and ultrasound-triggered drug delivery," *Ultrasonics Sonochemistry*, vol. 85, 105986, 2022.

[40] S. Kotopoulis and M. Postema, "Microfoam formation in a capillary," *Ultrasonics*, vol. 50, no. 4, pp. 260–268, 2010.

[41] B. Krasovitski, V. Frenkel, S. Shoham, and E. Kimmel, "Intramembrane cavitation as a unifying mechanism for ultrasound-induced bioeffects," *Proceedings of the National Academy of Sciences*, vol. 108, no. 8, pp. 3258–3263, 2011.

[42] N. Kudo, "High-speed in situ observation system for sonoporation of cells with size-and position-controlled microbubbles," *IEEE Transactions on Ultrasonics, Ferroelectrics, and Frequency Control*, vol. 64, no. 1, pp. 273–280, 2017.

[43] N. Kudo, K. Okada, and K. Yamamoto, "Sonoporation by single-shot pulsed ultrasound with microbubbles adjacent to cells," *Biophysical Journal*, vol. 96, no. 12, pp. 4866–4876, 2009.

[44] N. Kudo, R. Uzbekov, R. I. Matsumoto, R. Shimizu, C. S. Carlson, N. Anderton, A. Deroubaix, C. Penny, A. T. Poortinga, D. M. Rubin, A. Bouakaz, and M. Postema, "Oscillating endoskeletal antibubbles," in *Proceedings of the 40th Symposium on UltraSonic Electronics*, 2019.

[45] N. B. Leighl, S. Nirmalakumar, D. A. Ezeife, and B. Gyawali, "An arm and a leg: the rising cost of cancer drugs and impact on access," *American Society of Clinical Oncology Educational Book*, vol. 41, pp. e1–e12, 2021.

[46] T. G. Leighton, *The Acoustic Bubble*. London: Academic Press, 1994.

[47] T. G. Leighton, P. R. White, C. L. Morfey, J. W. L. Clarke, G. J. Heald, H. A. Dumbrell, and K. R. Holland, "The effect of reverberation on the damping of bubbles," *The Journal of the Acoustical Society of America*, vol. 112, no. 4, pp. 1366–1376, 2002.

[48] I. Lentacker, I. De Cock, R. Deckers, S. C. De Smedt, and C. T. W. Moonen, "Understanding ultrasound induced sonoporation: definitions and underlying mechanisms," *Advanced Drug Delivery Reviews*, vol. 72, pp. 49–64, 2014.

[49] I. Lentacker, S. C. De Smedt, and N. N. Sanders, "Drug loaded microbubble design for ultrasound triggered delivery," *Soft Matter*, vol. 5, no. 11, pp. 2161–2170, 2009.

[50] Y. Li, X. Zhang, W. Luo, D. Wang, L. Yang, J. Wang, L. Zhang, S. Zhang, S. Luo, and Y. Wang, "Dual-functionalized nanoparticles loaded microbubbles for enhancement of drug uptake," *Ultrasonics*, vol. 87, pp. 82–90, 2018.

[51] N. Mazzawi, M. Postema, and E. Kimmel, "Bubble-like response of living blood cells and microparticles in an ultrasound field," *Acta Physica Polonica A*, vol. 127, no. 1, pp. 103–105, 2015.

[52] P. Marmottant, S. van der Meer, M. Emmer, M. Versluis, N. de Jong, S. Hilgenfeldt, and D. Lohse, "A model for large amplitude oscillations of coated bubbles accounting for buckling and rupture," *The Journal of the Acoustical Society of America*, vol. 118, no. 6, pp. 3499–3505, 2005.

[53] P. Marmottant and S. Hilgenfeldt, "Controlled vesicle deformation and lysis by single oscillating bubbles," *Nature*, vol. 423, pp. 153–156, 2003.

[54] H. Medwin, "Counting bubbles acoustically: a review," *Ultrasonics*, vol. 15, no. 1, pp. 7–13, 1977.

[55] Ý. Mørch, R. Hansen, S. Berg, A. K. O. Åslund, W. R. Glomm, S. Eggen, R. Schmid, H. Johnsen, S. Kubowicz, S. Snipstad, *et al.*, "Nanoparticle-stabilized microbubbles for multimodal imaging and drug delivery," *Contrast Media & Molecular Imaging*, vol. 10, no. 5, pp. 356–366, 2015.

[56] J. Naude and F. Méndez, "Periodic and chaotic acoustic oscillations of a bubble gas immersed in an Upper Convective Maxwell fluid," *Journal of Non-Newtonian Fluid Mechanics*, vol. 155, no. 1–2, pp. 30–38, 2008.

[57] E. A. Neppiras and B. E. Noltingk, "Cavitation produced by ultrasonics: theoretical conditions for the onset of cavitation," *Proceedings of the Physical Society. Section B*, vol. 64, no. 12, pp. 1032–1038, 1951.

[58] B. E. Noltingk and E. A. Neppiras, "Cavitation produced by ultrasonics," *Proceedings of the Physical Society. Section B*, vol. 63, no. 9, pp. 674–685, 1950.

[59] N. Otsu, "A threshold selection method from gray-level histograms," *IEEE Transactions on Systems, Man, and Cybernetics*, vol. 9, no. 1, pp. 62–66, 1979.

[60] A. Panfilova, P. Chen, R. J. G. van Sloun, H. Wijkstra, M. Postema, A. T. Poortinga, and M. Mischi, "Experimental acoustic characterization of an endoskeletal antibubble contrast agent: first results," *Medical Physics*, vol. 48, no. 11, pp. 6765–6780, 2021.

[61] M. S. Plesset, "The dynamics of cavitation bubbles," *Journal of Applied Mechanics*, vol. 16, pp. 277–282, 1949.

[62] A. T. Poortinga, "Long-lived antibubbles: stable antibubbles through Pickering stabilization," *Langmuir*, vol. 27, pp. 2138–2141, 2011.

[63] A. T. Poortinga, "Micron-sized antibubbles with tunable stability," *Colloids and Surfaces A: Physicochemical and Engineering Aspects*, vol. 419, pp. 15–20, 2013.

[64] M. Postema, *Fundamentals of Medical Ultrasonics*. London: Taylor & Francis, 2011.

[65] M. Postema and A. Bouakaz, "Acoustic bubbles in therapy: recent advances with medical microbubbles, clouds, and harmonic antibubbles," *Applied Acoustics*, vol. 140, pp. 150–152, 2018.

[66] M. Postema, A. Bouakaz, C. T. Chin, and N. de Jong, "Simulations and measurements of optical images of insonified ultrasound contrast microbubbles," *IEEE Transactions on Ultrasonics, Ferroelectrics, and Frequency Control*, vol. 50, no. 5, pp. 523–536, 2003.

[67] M. Postema, F. J. ten Cate, G. Schmitz, N. de Jong, and A. van Wamel, "Generation of a droplet inside a microbubble with the aid of an ultrasound contrast agent: first result," *Letters in Drug Design & Discovery*, vol. 4, no. 1, pp. 74–77, 2007.

[68] M. Postema and O. H. Gilja, "Contrast-enhanced and targeted ultrasound," *World Journal of Gastroenterology*, vol. 17, no. 1, pp. 28–41, 2011.

[69] M. Postema and O. H. Gilja, "Jetting does not cause sonoporation," *Biomedical Engineering*, vol. 55, no. Supplement 1, pp. 19–20, 2010.

[70] M. Postema, S. Kotopoulis, A. Delalande, and O. H. Gilja, "Sonoporation: why microbubbles create pores," *Ultraschall in der Medizin*, vol. 33, no. 1, pp. 97–98, 2012.

[71] M. Postema, A. Novell, C. Sennoga, A. T. Poortinga, and A. Bouakaz, "Harmonic response from microscopic antibubbles," *Applied Acoustics*, vol. 137, pp. 148–150, 2018.

[72] M. Postema and G. Schmitz, "Ultrasonic bubbles in medicine: influence of the shell," *Ultrasonics Sonochemistry*, vol. 14, no. 4, pp. 438–444, 2007.

[73] M. Postema and G. Schmitz, "Ultrasonic fragmentation of microbubbles: a theoretical approach of the flash in flash-echo," in *Proceedings of the 2005 IEEE Engineering in Medicine and Biology 27th Annual Conference*, 2006, pp. 4023–4026.

[74] M. Postema, A. van Wamel, C. T. Lancée, and N. de Jong, "Ultrasound-induced encapsulated microbubble phenomena," *Ultrasound in Medicine & Biology*, vol. 30, no. 6, pp. 827–840, 2004.

[75] P. Prentice, A. Cuschieri, K. Dholakia, M. Prausnitz, and P. Campbell, "Membrane disruption by optically controlled microbubble cavitation," *Nature Physics*, vol. 1, no. 2, pp. 107–110, 2005.

[76] Lord Rayleigh, "On the pressure developed in a liquid during the collapse of a spherical cavity," *The London, Edinburgh, and Dublin Philosophical Magazine and Journal of Science*, vol. 34, no. 200, pp. 94–98, 1917.

[77] P. Riesz and T. Kondo, "Free radical formation induced by ultrasound and its biological implications," *Free Radical Biology and Medicine*, vol. 13, no. 3, pp. 247–270, 1992.

[78] S. Roovers, T. Segers, G. Lajoinie, J. Deprez, M. Versluis, S. C. De Smedt, and I. Lentacker, "The role of ultrasound-driven microbubble dynamics in drug delivery: from microbubble fundamentals to clinical translation," *Langmuir*, vol. 35, no. 31, pp. 10 173–10 191, 2019.

[79] J. A. Sebastian, E. M. Strohm, J. Baranger, O. Villemain, M. C. Kolios, and C. A. Simmons, "Assessing engineered tissues and biomaterials using ultrasound imaging: *in vitro* and *in vivo* applications," *Biomaterials*, vol. 296, 122054, 2023.

[80] M. Seki, T. Otsuka, R. Oitate, K. Masuda, J. Unga, R. Suzuki, and K. Maruyama, "Viability validation of therapeutic cells according to surrounded amount

of microbubbles and ultrasound exposure condition," *Japanese Journal of Applied Physics*, vol. 58, no. SG, SGGE13, 2019.

[81] S. Senapati, A. K. Mahanta, S. Kumar, and P. Maiti, "Controlled drug delivery vehicles for cancer treatment and their performance," *Signal Transduction and Targeted Therapy*, vol. 3, 7, 2018.

[82] Y. Shen, L. Hu, W. Chen, H. Xie, and X. Fu, "Drop encapsulated in bubble: a new encapsulation structure," *Physical Review Letters*, vol. 120, no. 5, 054503, 2018.

[83] J. Shi, D. Ahmed, X. Mao, S.-C. S. Lin, A. Lawit, and T. J. Huang, "Acoustic tweezers: patterning cells and microparticles using standing surface acoustic waves (SSAW)," *Lab on a Chip*, vol. 9, no. 20, pp. 2890–2895, 2009.

[84] K. K. Shung, "High frequency ultrasonic imaging," *Journal of Medical Ultrasound*, vol. 17, no. 1, pp. 25–30, 2009.

[85] J. Sundaram, B. R. Mellein, and S. Mitragotri, "An experimental and theoretical analysis of ultrasound-induced permeabilization of cell membranes," *Biophysical Journal*, vol. 84, no. 5, pp. 3087–3101, 2003.

[86] Z. Tai, Y. Huang, Q. Zhu, W. Wu, T. Yi, Z. Chen, and Y. Lu, "Utility of Pickering emulsions in improved oral drug delivery," *Drug Discovery Today*, vol. 25, no. 11, pp. 2038–2045, 2020.

[87] S. Tinkov, R. Bekeredjian, G. Winter, and C. Coester, "Microbubbles as ultrasound triggered drug carriers," *Journal of Pharmaceutical Sciences*, vol. 98, no. 6, pp. 1935–1961, 2009.

[88] K. Tsiglifis and N. A. Pelekasis, "Nonlinear radial oscillations of encapsulated microbubbles subject to ultrasound: the effect of membrane constitutive law," *The Journal of the Acoustical Society of America*, vol. 123, no. 6, pp. 4059–4070, 2008.

[89] M. Versluis, E. Stride, G. Lajoinie, B. Dollet, and T. Segers, "Ultrasound contrast agent modeling: a review," *Ultrasound in Medicine & Biology*, vol. 46, no. 9, pp. 2117–2144, 2020.

[90] Y. Vitry, S. Dorbolo, J. Vermant, and B. Scheid, "Controlling the lifetime of antibubbles," *Advances in Colloid and Interface Science*, vol. 270, pp. 73–86, 2019.

[91] K. Vokurka, "Comparison of Rayleigh's, Herring's, and Gilmore's models of gas bubbles," *Acta Acustica united with Acustica*, vol. 59, no. 3, pp. 214–219, 1986.

[92] H. Wang and P. R. Brito-Parada, "The role of microparticles on the shape and surface tension of static bubbles," *Journal of Colloid and Interface Science*, vol. 587, pp. 14–23, 2021.

[93] S. Wang, J. A. Hossack, and A. L. Klibanov, "From anatomy to functional and molecular biomarker imaging and therapy: ultrasound is safe, ultrafast, portable, and inexpensive," *Investigative Radiology*, vol. 55, no. 9, pp. 559–572, 2020.

[94] Y. Yamakoshi, T. Miwa, N. Yoshizawa, H. Inoguchi, and D. Zhang, "Effect of pretrapping of microbubbles in sonoporation using n-isopropylacrylamide gel flow channel phantom," *Japanese Journal of Applied Physics*, vol. 49, no. 7S, 07HF17, 2010.

[95] K. Yoshida, M. Ebata, C. Kaneko, Y. Zhang, Y. Shibata, K. Saito, T. Toyota, H. Hayashi, and T. Yamaguchi, "Fluorescence intensity changes depending on viscoelasticity of lipid shell coating microbubbles labeled with an indocyanine green derivative," *Japanese Journal of Applied Physics*, vol. 60, no. SD, SDDE10, 2021.

[96] R. Zia, A. Nazir, A. T. Poortinga, and C. F. van Nostrum, "Advances in antibubble formation and potential applications," *Advances in Colloid and Interface Science*, vol. 3, no. 6, 102688, 2022.

PUBLICATIONS

PUBLICATION I

On the behaviour of living cells under the influence of ultrasound

D. M. Rubin, N. Anderton, C. Smalberger, J. Polliack, M. Nathan, and M. Postema

Fluids, vol. 3, no. 4, 82
DOI: 10.3390/fluids3040082

fluids

MDPI

Review

On the Behaviour of Living Cells under the Influence of Ultrasound

David M. Rubin, Nicole Anderton, Charl Smalberger, Jethro Polliack, Malavika Nathan and Michiel Postema *

School of Electrical and Information Engineering, University of the Witwatersrand, Johannesburg, 1 Jan Smuts Laan, 2050 Braamfontein, South Africa; david.rubin@wits.ac.za (D.M.R.); 673663@students.wits.ac.za (N.A.); 2026923@students.wits.ac.za (C.S.); jethro.polliack@students.wits.ac.za (J.P.); malavika.nathan@students.wits.ac.za (M.N.)

* Correspondence: michiel.postema@wits.ac.za; Tel.: +27-11-7177237

Received: 19 September 2018; Accepted: 22 October 2018; Published: 26 October 2018

Abstract: Medical ultrasound technology is available, affordable, and non-invasive. It is used to detect, quantify, and heat tissue structures. This review article gives a concise overview of the types of behaviour that biological cells experience under the influence of ultrasound only, i.e., without the presence of microbubbles. The phenomena are discussed from a physics and engineering perspective. They include proliferation, translation, apoptosis, lysis, transient membrane permeation, and oscillation. The ultimate goal of cellular acoustics is the detection, quantification, manipulation and eradication of individual cells.

Keywords: cellular acoustics; ultrasound-induced lysis; acoustic microparticle manipulation; ultrasound-induced cell translation; micro-acoustics; non-bubble-assisted sonoporation

1. Introduction

Ultrasound technology is available, affordable and non-invasive. Therefore, it finds widespread application in medicine. Ultrasound is well established as an imaging modality in medical diagnostics, and, more recently, its use has been extended to therapy. Ultrasonic therapeutic modalities in current clinical practice are high-intensity focussed ultrasound (HIFU) [1], extracorporeal shockwave lithotrypsy [2], ultrasound contrast agent-assisted drug delivery [3], and combinations of some of these modalities [4]. Acoustic cluster therapy has shown great promise in a mouse study [5]. The aforementioned therapeutic modalities [1–5] are directed at modifying the macro-structural aspects of tissue. Claims have been made about pain relief with the aid of ultrasound equipment, but these are not supported by scientific evidence [6,7]. Several studies have suggested increased tissue repair owing to ultrasound exposure [8,9], which has led to the increased use of ultrasound equipment when treating bone fracture [10]. However, the acoustic setups of these [8–10] and other [11–14] tissue-repair studies have been such that thermal effects could not be ruled out. In fact, heating is the most plausible explanation for the phenomena observed [15]. The emerging field of ultrasonic manipulation at the micro-structural level, i.e., the individual cellular level, holds great promise both in diagnostics and therapeutics, and will constitute the focus of this review article.

The vast majority of scientific publications on the response of biological cells to ultrasound involve bubbles. Reviews on bioeffects typically do not include the situations without ultrasound contrast agents or inertial cavities [16–19]. This article reviews those effects of ultrasound on living cells that do not include inertial cavitation, cellular effects due to the introduction of bubbles, and non-destructive structural evaluation through ultrasonic biomicroscopy.

As an introduction to the topic, a simple model of the cell is assumed, followed by a brief summary of the relevant ultrasound parameters. The paper then covers various studies on the effects of ultrasound on cells. The cell types covered in these studies include plant cells, bacteria, cancer cells, mammalian cells, red blood cells, and platelets.

1.1. Cells

Cells are ubiquitous in living organisms, with the adult human body containing more than 10^{14} of these complex structures [20]. Knowledge of the mechanical properties of cells is essential to appreciate their behaviour in response to ultrasound.

Cells have a wide variety of morphological characteristics, and in mammals they typically range in diameter from 6 μm to 40 μm. While cells are complex structures, for the purpose of understanding cellular acoustics, a simplified model is assumed, shown in Figure 1.

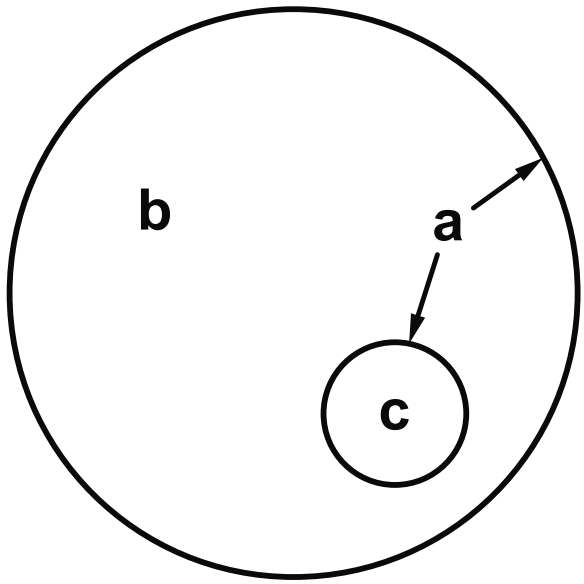

Figure 1. Highly simplified schematic of a standard mammalian cell, with bilayer membranes (**a**) surrounding the cell and the nucleus; cytoplasma (**b**); and a nucleus (**c**).

The external surface of all cells is a semi-permeable lipid-based membrane. This so-called plasma membrane is the cell's elastic surface that separates the cell's gel-like fluid, known as cytoplasm, from its external surroundings. Cell membranes are gelatinous structures which play a role in cellular processes such as growth, movement, division and secretion. The number of double bonds in the organic compounds of the plasma membrane affects the fluidity of the membrane, with more double bonds correlating to increased fluidity [20].

The cytoplasm consists of all the material inside of a living cell, with the exception of the nucleus [20]. With a bulk modulus of 4 TPa, the incompressible cytoplasm facilitates the cell's ability to elongate, but not to shrink [21]. This means that cells deform when subjected to compressive forces. Some cells, particularly plant cells, have an additional rigid, cellulose-based, outer wall for structural support. Located within the cytoplasm are a range of sub-cellular structures known as organelles. While not found in all cells, the nucleus, if present, contains the genetic material which directs cellular function.

Damaged cells contribute towards life-threatening diseases, making it advantageous to remove these cells from human and animal bodies [22]. Damaged cells are naturally separated from healthy cells and then destroyed by the body's internal mechanisms, e.g., apoptosis. Techniques have been developed to separate cells; these techniques are mostly based on adherence, density, and antibody binding [22]. The most common in-vitro density-based method is centrifugation, which is an expensive and tedious method. There is a need for a cost-effective, efficient method to remove damaged cells, not only in vitro, but also in vivo—from the human body.

1.2. Ultrasound

In medical ultrasonics, ultrasound fields are generated with multi-element transducers, called probes [23]. There are many differences in probe geometry and signal output, contributing to a vast number of radiated ultrasound fields [24]. An ultrasound field at a specific location is characterised by its dominant period, centre frequency, pulse length, peak-negative pressure, peak-positive pressure, peak-to-peak pressure, pulse-repetition time, pulse-repetition frequency, and duty cycle [25]. These parameters are schematically shown in Figure 2. The dominant period is the time taken to complete a single sonic cycle. The centre frequency is the inverse of the dominant period. The pulse length is the duration of pulse transmission. The pressure amplitude p_A may vary within a pulse. Consequently, the pulse pressure is typically expressed in its peak-positive, peak-negative, and peak-to-peak pressures. The pulse-repetition period is the duration from the onset of a pulse to the onset of the next pulse. The pulse-repetition frequency is the inverse of the pulse-repetition period. The duty cycle is the percentage of transmission time during a pulse sequence.

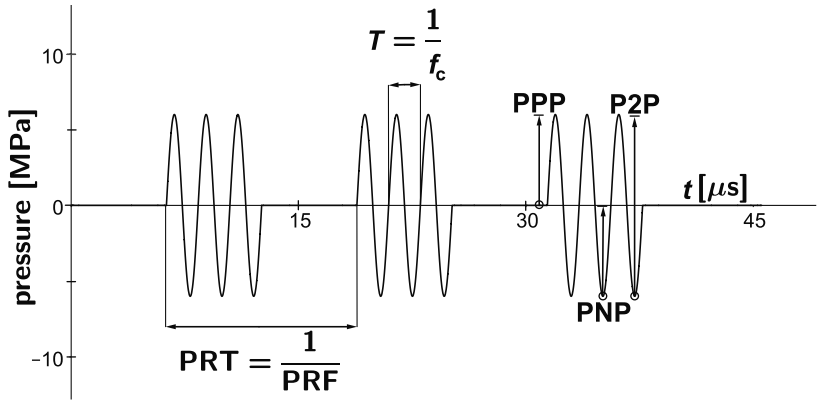

Figure 2. Representation of an ultrasound pulse sequence with dominant period T, centre frequency f_c, peak-positive pressure (PPP), peak-negative pressure (PNP), peak-to-peak pressure (P2P), pulse-repetition period (PRT), and pulse-repetition frequency (PRF).

The power W is by definition the transmitted energy per unit time. Every point in a sound field lies on a surface S on which the intensity $I = W S^{-1}$ is the same. The average intensity is given by [25]:

$$< I >= \frac{{p_A}^2}{2\rho c}, \quad (1)$$

where p_A is the acoustic pressure amplitude, c is the speed of sound of the medium and ρ is the density of the medium.

It should be noted that, in medical ultrasonics, the bulk of the acoustic waves propagate through the human body, whilst only a small portion is scattered on tissue transitions and micro-structures [25].

Although ultrasound is by definition all sound with frequencies greater than 20 kHz, for most medical applications, including physiotherapy [26], ultrasound devices with frequencies greater

than 500 kHz are used. Ultrasound with frequencies of 10–100 MHz is used for biomicroscopy [27], i.e., the non-destructive evaluation of cellular structures [28]. Biomicroscopy does not involve the active response of cells and is therefore excluded from this review.

If the peak-negative acoustic amplitude surpasses a critical threshold, the so-called cavitation threshold, bubbles may form in a liquid [23,29–31]. Inertial cavitation has been associated with the formation of free radicals [32,33], causing harmful biological effects [34,35] but also with applications in drug delivery [36]. These so-called bioeffects have been studied since 1928 [37,38].

An indication of potential mechanical damage due to inertial cavitation is given by the mechanical index (MI):

$$\mathrm{MI} = \frac{\mathrm{PNP}}{\sqrt{f_\mathrm{c}}}, \tag{2}$$

where peak-negative pressure (PNP) is expressed in MPa and f_c is expressed in MHz. The value taken for PNP should be the maximum anywhere in the field, measured in water but reduced by an attenuation of $0.3\,\mathrm{dB\,cm^{-1}\,MHz^{-1}}$.

For mechanical index values between 0.3 and 0.7, slight damage to the neonatal soft tissues such as the lung or intestine may occur [39], whereas ultrasound applied with a mechanical index value greater than 0.7 is considered unsafe for diagnostic applications [40,41]. Mechanical indices have been limited to 1.9 for medical imaging with commercial scanners [42]. A mechanical index of less than 0.3 is recommended for medical diagnostic applications [23].

Although the ultrasound-assisted formation of bubbles in the body is regarded as damaging, and therefore often unwanted, phenomenon in vivo, artificial microbubbles have been injected for diagnostic purposes. These so-called ultrasound contrast agents consist of encapsulated microbubbles with diameters below 6 µm. The microbubbles oscillate, translate, ripen, coalesce, jet, and cluster under the influence of ultrasound [43]. At low MI, their characteristic acoustics make them suitable tracers for perfusion imaging [44]. At high MI, they act as cavitation nuclei, amplifying effects of inertial cavitation. The damaging effects of inertially driven bubbles on cells have been studied intensively [45]. It is however, beyond the scope of this review paper, as its focus is on the influence of ultrasound itself on biological cells.

In the case of bubble presence, the ultrasound predominantly acts to activate the bubbles to interact with the nearest structure, which just may happen to be a biological cell [17]. Studying the interactions of acoustically active bubbles near cells is a field on its own, with the primary purpose of understanding sonoporation [46,47]. Sonoporation is the transient permeation and resealing of a cell membrane with the aid of ultrasound, typically but not necessarily in the presence of an ultrasound contrast agent. Sonoporation allows for the trans-membrane delivery and cellular uptake of macromolecules [48] between 10 kDa and 3 MDa [49], and is therefore of utmost interest for ultrasound-aided drug [50] and gene delivery [51]. Although the mechanical disruption with the aid of ultrasound has been attributed to damaging effects of inertial cavitation [52–55], the increased uptake has also been observed, albeit less frequently, at low acoustic amplitudes, i.e., in acoustic regimes where inertial cavitation is not to be expected and without the presence of microbubbles [56]. Consequently, the studies on sonoporation without the presence of microbubbles have been included in this review, if the acoustic regime applied was below the inertial cavitation threshold. Sonoporation studies with probable microbubble presence have been excluded from this review.

1.3. Mechanical Cell Response to Ultrasound

Let us modify the cell model of Figure 1 to a model with an incompressible nucleus, shown in Figure 3, with the bilayer cell membrane of inner radius R_1 and outer radius R_4 split into an outer monolayer membrane of thickness $(R_4 - R_3)$ and an inner monolayer membrane of thickness $(R_2 - R_1)$, separated by a gaseous void of thickness $(R_3 - R_2)$. It is assumed that $(R_3 - R_2) \ll (R_4 - R_3) = (R_2 - R_1)$ [57,58].

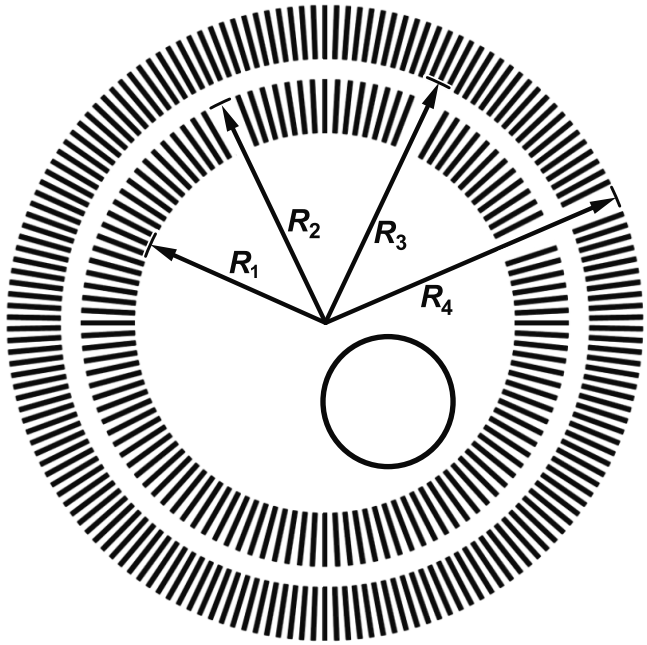

Figure 3. Highly simplified schematic of a cell with an outer monolayer membrane of thickness $(R_4 - R_3)$ and an inner monolayer membrane of thickness $(R_2 - R_1)$, separated by a gaseous void of thickness $(R_3 - R_2)$.

The oscillation dynamics of a spherically symmetric cell with incompressible nucleus an outer Newtonian membrane of finite thickness, surrounded by a Newtonian viscous liquid, are governed by a Rayleigh–Plesset-like equation of the following form [57]:

$$\begin{aligned} \rho R_3 \ddot{R}_3 \left[1 + \left(\tfrac{\rho - \rho_\mathrm{M}}{\rho_\mathrm{M}}\right) \tfrac{R_3}{R_4}\right] \quad & + \rho \dot{R}_3^2 \left[\tfrac{3}{2} + \left(\tfrac{\rho - \rho_\mathrm{M}}{\rho_\mathrm{M}}\right) \left(\tfrac{4R_4^3 - R_3^3}{R_4^3}\right)\right] \\ = \quad & p_{\mathrm{g}0} \left(\tfrac{R_{30}^3 - R_2^3}{R_3^3 - R_2^3}\right)^{\gamma} - \tfrac{2\sigma_3}{R_3} - \tfrac{2\sigma_4}{R_4} - p_0 - P(t) - 4\eta \tfrac{R_3^2}{R_4^3} \dot{R}_3 - 4\eta_\mathrm{M} \tfrac{R_4^3 - R_3^3}{R_3 R_4^3} \dot{R}_3 \,, \end{aligned} \tag{3}$$

where R_n is the instantaneous radius of membrane interface n (*cf.* Figure 3), ρ_M is the membrane density, $p_{\mathrm{g}0}$ is the initial gas pressure inside the void, R_{30} is the initial radius of interface 3, γ is the polytropic exponent of the gas inside the void, σ_n are the surface tensions at the two respective interfaces n of the outer membrane, p_0 is the ambient pressure, $P(t)$ is the acoustic driving pressure as a function of time, η is the viscosity of the medium, and η_M is the membrane viscosity.

Numerical solutions of Equation (3) have shown that, even at low acoustics amplitudes, the void inside the bilayer membrane may have oscillation amplitudes of multiple times its initial thickness. Although these excursions are not enough to permanently damage a human cell [57], they are strong enough to induce physical translation of the cell. To turn bilayer membranes into inertial cavities, acoustic amplitudes would be required greater than the inertial cavitation threshold [57].

A general one-dimensional translation equation for a cell with an incompressible liquid core surrounded by a compressible void subjected to a spatio-temporal pressure field $P(x,t)$ has been derived [59]:

$$m_\mathrm{C} \ddot{x} + \frac{2\pi}{3} \rho \frac{\mathrm{d}}{\mathrm{d}t} (R_4^3 \dot{x}) = -\frac{4\pi}{3} R_4^3 \frac{\partial}{\partial x} P(x,t) + F_\mathrm{d} \,, \tag{4}$$

where m_C is the mass of the cell and F_d is the drag force [60].

To summarise numerical studies on cell translation—in a standing ultrasound field, cells may move to nodes or antinodes of the sound field, owing to primary Bjerknes forces [61,62]. In addition, cells might attract each other, owing to secondary Bjerknes forces. The collision speed of two identical oscillators subjected to mutual secondary Bjerknes forces is proportional to the oscillator size to the power of five and inversely proportional to the squared distance between the oscillators [43]. Given the small volume of the gaseous voids inside cell membranes, the oscillation excursions at safe ultrasound pressures might not be high enough for biological cells to create secondary Bjerknes forces strong enough to attract other cells, unless the cells are already very close to each other. However, Henrietta Lacks (HeLa) cells have been reported to attract ultrasound contrast agent at a low mechanical index, which Delalande et al. attributed to secondary Bjerknes forces [56,63].

2. Overview of Scientific Publications on Cellular Ultrasonics

The following overview of scientific publications on cellular ultrasonics excludes papers on high-intensity focussed ultrasound (HIFU),microbubble-assisted sonoporation, and inertial cavitation. However, in some papers that deal with ultrasound-cell interaction, the acoustic regime has not been properly stated, making the experiments non-repeatable [64] and occasionally implausible [65]. In cases where there was some cause for doubt whether inertial cavitation played a role, it was chosen to include these papers.

2.1. Early Studies

It was chosen to include a few of the earliest papers on cellular acoustics out of historic curiosity, although the acoustic regimes of these papers are most probably beyond the inertial cavitation threshold. The articles in this section are in chronological order.

In a 1964 study, newt larvae were subjected to 5 min of 1 MHz ultrasound at intensities of 8–15 W cm^{-2} [66]. Their notochord cells appeared normal on light microscopy, but the endoplasmic reticulum was seen to be severely disrupted on electron microscopy. By 24 h post sonication, 50% of the endoplasmic reticulum had reverted to a normal structure.

In an early study on chromosome aberrations induced by ultrasound, two commercial foetal ultrasound devices were used [67]. Cultured healthy-donor blood was subjected to ultrasound for 1- and 2-h durations using these devices with manufacturer specifications of 2.25 MHz and maximum power of 30 mW. The cultured cells were examined for chromosomal aberrations after sonication. There was clear evidence of substantially increased chromosomal damage in the sonicated samples compared to controls. In addition, the longer duration produced greater damage. No formal statistical significance test was reported on the results.

As an early study on bioeffects in tissue [68], frog muscle was subjected to sonication at 85 kHz using a vibrating needle machined into a stainless steel acoustic horn. The sound amplitude was expressed in terms of the deviation of the needle tip which ranged from 1–5 μm, with maximum deviation corresponding to a sub-cavitation pressure amplitude of 0.125 atm. The temperature rise was minimal and, at low amplitudes, structures such as the mitochondrial christae showed disruption. At higher amplitudes, disruption to the Z and M lines was demonstrated. Z and M lines are anatomical structures that are evident on microscopy and that relate to the organisation of actin and myosin protein filaments in muscle cells. Actin and myosin are proteins responsible for muscle contraction. The data suggest that the degree of disruption is dependent on duration and amplitude of sonication. These effects were seen after 1 min of sonication. The minimal temperature rise and the sub-cavitation pressure amplitudes suggest a mechanism other than cavitation and thermal effects for the cell disruption. The authors speculate that the changes may be due to acoustic streaming and movement due to radiation forces. They point out that the relatively constrained structures in muscle cells are not expected to be subjected to these forces. However, in the presence of non-uniform sound fields, twisting and stretching of the membranes and filamentous structures may occur, due to viscous stresses.

In succession of studies on plant cells by M.W. Miller [69,70], D.G. Miller subjected *Elodea* cells to ultrasound for 100 s at frequencies ranging from 0.45 to 10 MHz [71]. Intensity thresholds for cell death were found to vary with frequency and ranged from 75 mW cm^{-2} at 0.65 MHz to 180 mW cm^{-2} at 5 MHz. Cell death was attributed to the presence of gas bodies in inside the *Elodea* leaves, modelled in a separate paper [72]. The ultrasound-induced motion of fluids had been reported earlier inside *Elodea* leaves [73] and in a *Curcurbita pepo* hair cell [74].

Discoid platelet suspensions were subjected to ultrasound fields in the 1–10-MHz frequency range at acoustic pressure amplitudes in the range of 0.5–76 kPa [75]. Acoustic streaming was observed and changes in transmitted light intensity were attributed to changing platelet orientation. Platelet disruption had been reported after 5 min of 1-MHz sonication at intensities of 0.2 and 0.6 W cm^{-2} [76]. In the latter study, following sonication, platelet debris were observed and platelet function was impaired. There were qualitative differences between sonicated and non-sonicated specimens in the macroscopic characteristics of the clot.

This concludes the overview of early cellular acoustics studies. Despite the high intensities used, not all phenomena observed are destructive, most notably intracellular streaming.

2.2. Damage

This section gives an overview of cellular acoustics studies that resulted in transient or permanent cell damage. The studies have been treated in chronological order.

Human red blood cells were put in dialysis tubing and exposed to 1 to 2 min of 1-MHz continuous-wave ultrasound at intensities of 0–5 W cm^{-2} spatial peak temporal average [77]. Some of the samples contained ultrasound contrast agent. The degree of cell lysis was found to be intensity-dependent. The maximum lysis was over 50% with ultrasound contrast agent present and 30% without ultrasound contrast agent at an intensity of 3 W cm^{-2}. After this maximum, with increasing intensity, there was some decline in lysis. The degree of lysis was found to be insensitive to the concentration of ultrasound contrast agent but decreased with increasing red blood cell concentrations (haematocrit).

Rendering cell membranes permeable to large molecules such as proteins and deoxyribonucleic acid (DNA) has potential therapeutic applications [78]. The effects of ultrasound on cell membrane permeation was studied by subjecting bovine red blood cells to continuous ultrasound at 24 kHz. A number of incident pressures were used in this study under various conditions and were estimated to range from less than 1 atm to 10 atm. Permeation was determined by measuring the haemoglobin released, which was found to increase as a linear function of incident pressure. It was also found to increase as a function of sonication time, with a threshold for permeation of 100 ms.

A human leukaemia-60 (HL-60) cell line in suspension was exposed to continuous-wave 255-kHz ultrasound at an intensity of 0.4 W cm^{-2} for 30 s [79]. Experiments were performed with and without the photosensitive drug merocyanine 540. Scanning electron microscopy showed that, in the presence of merocyanine 540, there were substantial disruptions to the cell membrane including porosity, dimpling craters, and breaches. In the absence of the drug, however, minimal membrane changes were observed. In addition, inclusion of merocyanine 540 in the ultrasound experiments resulted in a measurable diminution in cell viability which was not seen in the absence of the drug. This study is the reason that sonic cell permeation is referred to as sonoporation.

Belgrader et al. investigated the effect of ultrasound sonication on the spore-forming bacterium *B. subtilis*, which served as an anthrax spore (*B. anthracis*) surrogate [80]. The study aimed at identifying suitable techniques to disrupt anthrax spores, a critical step in achieving rapid and sensitive genetic identification, e.g., polymerase chain reaction (PCR), in cases where *B. anthracis* spores are used as a weapons. These spore-forming bacteria have an outer cortex that is extremely resistant to disruption (lysis) by various physical and chemical techniques, and the goal was to identify a technique that could achieve rapid spore lysis. Spore disruption was achieved by incubating the spores with 106-µm glass beads to enhance the destructive effects of cavitation. Sonication using 60 W at 67 kHz for 2 min,

50 W at 22 kHz for 30 s, and 40 W at 47 kHz for 30 s were tested. In their final design, adequate cell lysis was achieved in 30 s.

In a follow-up study [81], spores of the same bacterium *B. subtilis* were subjected to sonication at 40 kHz in the presence of 106-μm glass beads for 10 to 20 s. The acoustic horn amplitudes used were expressed in its surface displacement, 25 and 38 μm peak-to-peak, and the sonicated liquid was subjected to hydrostatic pressures ranging from 34 to 138 kPa, in an attempt to improve coupling between the horn and the liquid. The ultrasonic energy was transferred from the horn to the fluid via a thin flexible membrane and it was shown that this design avoids cavitation as large pressure drops were absent due to the film separating from the horn. The sonication technique produced effective disruption of bacterial spores as evidenced by scanning electron microscopy. The utility of this technique as a means of releasing DNA from disrupted spores for the purpose of molecular diagnostics was discussed and it was concluded that the efficiency of DNA amplification using PCR increased as a function of the applied hydrostatic pressure.

In a leukaemic cell study [82], therapeutic ultrasound at a frequency of 750 kHz and spatial-peak temporal average intensity levels of 103.7 W cm^{-2} and 54.6 W cm^{-2} was applied to HL-60, K562, U937, and M1/2 leukemia cell line cultures. Lower acoustic amplitudes of 22.4 W cm^{-2} spatial-peak temporal-average intensity were used as a control. Although it is well known that high-intensity ultrasound causes inertial cavitation effects, the authors were able to demonstrate the induction of programmed cell death, i.e., apoptosis, which holds promise for cancer therapy. Interestingly, the effects were similar to those produced by gamma radiation.

Cultured vascular endothelial cells were subjected to eight repetitions of sonication for 1 min each experiment with unspecified high-frequency ultrasound at 2.5 W cm^{-2} in the presence of plasmid DNA with and without an ultrasound contrast agent present [83]. In addition, in-vivo sonication under similar conditions was performed for 2 min on a damaged rat carotid artery in the presence of DNA. In both cases, transfection of DNA into cells was achieved with higher efficiency under sonication, and even more so in the presence of the ultrasound contrast agent. This paper is generally considered as fundamental proof that cells themselves may respond to ultrasound at acoustic conditions below the inertial cavitation threshold.

The cytotoxic effect of low-energy ultrasound at 7 mW mL^{-1} acoustical power was evaluated for various exposure times ranging from 30 min to 5 h at a frequency of 1.8 MHz and on/off cycle of 5.5 ms/3 ms [84]. Normal mononuclear cells, primary leukaemic cells and four leukaemic cell lines were studied. The authors demonstrated that necrosis is significantly diminished while apoptosis is stimulated in leukaemic cells. They also demonstrated that ultrasound exposure is linked to oxidative stress, and that active oxygen scavengers reduce the effect of ultrasound on apoptosis, suggesting a sonochemical mechanism.

A bacterium *E. coli* and a yeast species *S. cerevisiae* were studied under ultrasound sonication with a view to producing cell lysis as a first step in various diagnostic processes [85]. Sonication was achieved using a spherically focussed 1-MHz ultrasound beam in a specially designed sonication chamber. Treatment was at 5.2 W cm^{-2} for 30 s, which resulted in greater than 99% loss in viability of both cell types. However, the yeasts demonstrated a relative resistance to disruption and further chemical techniques were needed to liberate cell contents.

The transfer of DNA into cells has clinical, bio-industrial and environmental applications [86]. This study investigated the use of 40-kHz ultrasound to achieve DNA transfer into a variety of bacterial species. In the centre of the experimental bath used, the estimated intensity was 240 mW cm^{-2}. The optimal duration of sonication was chosen to be 10 s, as an optimal compromise between the competing requirements of efficiency of DNA transfer and minimising ultrasound-induced loss of cell viability. Sonication is the putative mechanism for ultrasound-based DNA transfer and it proved substantially more efficient than the commonly used methods of electroporation and conjugation.

The combined effects of low-intensity pulsed ultrasound and doxorubicin (DOX) on cell killing and apoptosis induction of human myelomonocytic lymphoma U937 cells was investigated in vitro [87].

The experiments were conducted in four groups, including an ultrasound-treated group and a combined ultrasound and DOX-treated group. Cells were exposed to 5 μM DOX for 30 min and sonicated 60 s by 1-MHz pulsed ultrasound with a 100-Hz pulse-repetition frequency and a 10% duty cycle. The acoustic intensities varied between 0.2 and 0.5 W cm^{-2}. No cell killing or induction of apoptosis was observed at 0.2 W cm^{-2}. However, cell killing, induction of apoptosis, and hydroxyl radical formation were detected at intensities equal to and greater than 0.3 W cm^{-2}. More radicals were produced in the combined ultrasound and DOX group than with ultrasound alone. Yoshida et al. hypothesised that DOX treatment weakens cell membranes, so that sonoporation is more successful.

Sonication with 40-kHz ultrasound was shown to inhibit growth of Gram-negative bacteria with species such as *E. coli* showing sufficient sensitivity that they were eradicated in as little as 5 min [88]. Gram-positive bacteria, however, were resistant to sonication. This study shows that inhibition of bacteria by sonication is dependent on a number of factors including species, temperature, and duration of sonication. The results have implications for the management of bacterial infections of prosthetic implants which represent an important cause of morbidity and implant failure.

In a study on the ultrasound-induced inactivation of Gram-negative and Gram-positive bacteria in secondary treated municipal waste water [89], various bacterial species were subjected to 24 kHz of 1500 W L^{-1}, corresponding to 5400 kJ L^{-1} specific nominal energy, for a duration of 60 min in the presence and absence of titanium dioxide particles. Gram-negative bacteria proved to be highly susceptible to inactivation by sonication using this regime, showing a response of greater than 99%. Gram-positive bacteria showed substantially lower inactivation rates. Adding titanium dioxide enhanced the response of both Gram-negative and Gram-positive bacteria to the destructive effect of sonication. However, this enhancement was far more modest in the case of Gram-positive bacteria.

To investigate the effect of diagnostic ultrasound on blue-green algae eradication in a laboratory setup [90], three undamped single-element ultrasound transducers were used, with centre frequencies of 200-kHz, 1-MHz, and a 2.2-MHz, respectively. The transducers were subjected to 16-Vpp square pulses at an 11.8-kHz pulse-repetition rate. Low acoustic amplitudes were used in order to comply with an MI below 0.3. The peak-negative acoustic pressures were 40 kPa for the 1-MHz transducer and 68 kPa for the 2.2-MHz transducer, respectively. The blue-green algae used were of the *Anabaena sphaerica* species. Blue-green algae were forced within minutes to sink at the ultrasonic frequencies studied, thus supporting the hypothesis that heterocysts release gaseous nitrogen during sonication. A similar study had been done on a different cyanobacteria species, *Microcystis aeruginosa* [91]. Beakers were sonicated during 5 min at 25 kHz at 0.32 W mL^{-1}, which inhibited growth. Fourteen days after sonication, the cell concentration was only 14.1% of the control sample.

To investigate the effect of low-intensity ultrasound on DNA [92], 1.0-MHz ultrasound with 100-Hz fixed pulse-repetition frequency and 10% duty cycle was generated during 1 min in culture dishes containing four different leukaemia cell lines, U937, Molt-4, Jurkat, and HL-60, at intensities of 0.1, 0.2, 0.3, and 0.4 W cm^{-2}, corresponding to acoustic pressure amplitudes of 0.061, 0.105, 0.132, and 0.144 MPa, respectively. Only at the two highest intensities were DNA double-strand breaks with all cell lines observed. This damaging effect was attributed to mechanical stress.

A modified experimental setup was used to carry out ultrasound-assisted gene transfection [93]. Sonication was carried out using 1.0-MHz ultrasound at an intensity of 0.3 W cm^{-1} and a 50% duty cycle with a 5-Hz pulse-repetition frequency. Dishes containing HeLa cells in the presence of free plasmid DNA (pDNA) were sonicated immediately after preparation for periods of 30 s or 15 min. The results showed that ultrasound enhances the intracellular trafficking of previously internalised genes when longer sonication periods are applied.

There is a need to have techniques to disrupt (lyse) cells in order to release their contents for the purpose of drug development and other biological research [94]. Detergent-based disruption frequently has unfavourable effects on cells. Ly et al. developed an ultrasonic method to affect this disruption. Medical Research Council cell strain 5 (MRC-5) cells infected with an attenuated Varicella–Zoster virus

were subjected to ultrasound of intensities from 0.1–10 W cm^{-2} and at duty cycles of 0.1–20%. Cell lysis was achieved.

Most experimental studies in this section resulted in lysis. If we regard sonoporation as unsuccessful lysis, we might explain why both phenomena are observed in the same acoustic regimes. Apoptosis is less often observed. This phenomenon is associated with high MI and the formation of free radicals.

The experimental studies with bacteria were performed under unclear conditions. It would be interesting to compare acoustic lysis thresholds for mixtures of desirable and undesirable cells.

2.3. Translation

This section gives an overview of cellular acoustics studies that resulted in the translation of cells. The studies have been treated in chronological order.

To investigate the effects of ultrasound on blood platelets, platelet-rich plasma and washed platelets were treated with 22-kHz ultrasound at intensities ranging from 1 to 8.8 W cm^{-2} over multiple seconds [95]. Sonication of a calcium-containing preparation resulted in intensity- and time-dependent platelet aggregation. This effect, however, was absent in a calcium-free medium. Both the calcium-containing and calcium-free preparations showed a substantial increase in intracellular calcium in response to sonication.

Zourob et al. addressed the need to reliably and sensitively detect bacteria without the time-consuming step of culture [96]. A sonication and detection chamber was constructed. The chamber included an ultrasound-producing piezoelectric transducer and a specially designed optical metal-clad leaky waveguide (MCLW) with immobilised antibodies on the surface which, using optical techniques, served as the bacterial detector. This MCLW detector was created by depositing the cladding on a 1-mm glass slide that served as a half-wavelength ultrasound reflector, resulting in ultrasound standing waves, with a node forming at the detector-water interface at a frequency of 3 MHz. This caused bacterial spores to collect at the detector during sonication through radiation forces. Stepping the ultrasound in 20-kHz increments from 2 to 4 MHz, it was found that 2.94 MHz was a suitable operating frequency as it represented the maximum voltage difference between the water-filled and empty chamber and was assumed to represent a resonance in the water. As the chamber was a quarter wavelength long, only a single node could form. Sonication for 3 min caused the bacterial spores to move efficiently towards the detector and form regular patterns at the detector surface. These patterns varied in their appearance with ultrasound frequency changes as small as 150 kHz. Increasing the applied peak-to-peak voltage, which is proportional to sound pressure, resulted in increased bacterial spore capture at the interface up to a maximum of 4 V, after which the bacterial spore capture diminished due to the formation of aggregates.

In a similar experimental setup as the one used by Mizrahi et al. [97], endothelial cells were subjected to 1-MHz ultrasound with acoustic pressure amplitudes between 50 kPa and 300 kPa and a duration of 5 min at a 20% duty cycle [26]. Endothelial detachment was observed, followed by the geometric reorganisation of the cells according to a periodic pattern, corresponding to nodes or antinodes of the sound field. In addition, sonication caused increased clustering of $\alpha V\beta 3$ integrin, a transmembrane protein. However, sonication did not change the amount of β-actin monomers, which are involved in reshaping of the cell.

The accumulation of cells in the nodes or antinodes of a sound field was also described in a study to separate bacterial *E. coli* cells and yeast cells, sonicated at 1 MHz and 3 MHz [98].

Following an early review on acoustic manipulation [15], several studies were published on devices that use sound to force cells to translate. Optical observations of the clustering behaviour of living cells and several other particles were done in a standing sound field at 1 MHz or 3 MHz continuous-wave ultrasound with peak-to-peak amplitudes between 1 V and 10 V, generated inside a ring transducer [99]. Upon sonication, blood cells were observed to become trapped in the nodes of the ultrasound field owing to primary radiation forces. It was found that red blood cells and hydrophobic particles translate like a particle trapped inside a thin gas shell. In fact, the sonophore

model mentioned treats biological cells in a similar way [58]. Cells have also proven to be responsive to acoustic radiation forces at a frequency much higher than used in the former study [99], making single cell-type-specific cell sorting feasible [100,101]. The latter studies used a device operating with standing waves of 19.4 MHz [100,101]. A similar device for the identification, separation and cell-type specific manipulation of not single but multiple biological cells was also designed and built [102]. Cultured cells in a Petri dish were sonicated at 7-MHz continuous-wave ultrasound for 30 s. After sonication, Chinese hamster ovary (CHO) cells were seen to have formed clusters of packed cells whist human embryonic kidney (HEK) cells did not show cluster formation at all. The experiments were done with separate CHO and HEK cell cultures, and a mixture thereof. In a mixture of both CHO and HEK cell cultures, only the cells of one type cluster. It was concluded that different cell types may behave differently at the same ultrasound frequency.

Most experimental studies resulting in translation were carried out in standing wave fields. Therefore, cell aggregation is the most-observed translation phenomenon. It is interesting to trace cell translation speed as a function of cell bulk modulus. If subtle cell stiffness differences result in a significant speed difference, individual cancer cells or parasite-infested cells might be traced acoustically.

2.4. Proliferation

This section gives an overview of cellular acoustics studies that resulted in changed proliferation of cells. The studies have been treated in chronological order.

Sonication at intensities of up to 2 W cm^{-2} at 70 kHz of three bacterial species, *viz.*, *S. epidermidis*, *E. coli*, and *P. aeruginosa*, demonstrated increased biofilm and planktonic growth compared to the absence of sonication [103]. Greater intensities resulted in inhibition of bacterial adhesion to surfaces. Continuous-wave ultrasound was administered in these experiments except in the case of *P. aeruginosa*, where a 1:5 duty cycle was used and delivered in 100-ms pulses with pulse-repetition every 500 ms for 48 h. The authors propose an enhanced mass transport phenomenon as the basis for the increased bacterial growth.

Cultured bovine aortic endothelial cells were subjected to sonication for 15 and 30 min at intensities 1.2 W cm^{-2} at frequencies of 0.5, 1.0, 3.5, and 5.0 MHz in both pulsed-wave (50% duty cycle) and continuous-wave modes [104]. Increased cell proliferation was evident in the ultrasound-treated cells compared to the non-sonicated controls, with continuous-wave mode having a greater effect on proliferation than pulsed mode. Transmit frequency did not have a statistically significant effect in the range studied, and the proliferation effect became more prominent with elapsed time after sonication up to the 72 h studied. Sonication also produced transient partial disassembly of structures such as actin stress fibres and microtubules. This effect was resolved within a few hours after sonication. This study is thought to have implications for ultrasound-based promotion of wound healing.

Whilst the 2007 study of Hultström et al. describes experiments on acoustic cell trapping in a microfluidic channel, it was found that 30–75 min of sonication with a 3-MHz standing wave field with a pressure amplitude of 0.85 MPa was beneficial to the proliferation of CV-1 in origin simian line 7 (COS-7) cells [105].

The observation that increased proliferation is frequency-independent hints at a temperature-related effect. This is supported by the fact that continuous wave augments proliferation. Null experiments are required at slightly incremented temperatures to determine, whether temperature or vibration is of influence on cell proliferation.

2.5. Internal Changes

This section gives an overview of cellular acoustics studies that resulted in changes inside the cells. The studies have been treated in chronological order.

Rabbit corneas were exposed in vivo to continuous-wave ultrasound at a frequency of 880 kHz and with intensities ranging from 0.19 to 0.56 W cm^{-2} for 5 min [106]. These intensities correspond

to ultrasound pressures of 0.08 to 0.13 MPa and mechanical indices of 0.08 to 0.14. The increasing intensities of sonication caused sodium fluorescein, a hydrophilic dye introduced onto the corneal surface, to appear in the fluid of the anterior eye at higher concentrations than in non-sonicated eyes, with concentration increases over non-sonicated eyes ranging from more than double, to more than 10-fold at the highest intensities. Microscopic and macroscopic examination of the corneas after sonication revealed structural changes in the surface layer of cells including pitts, but not in the deeper layers. These changes reversed after approximately 90 min.

Or et al. proposed that relative oscillatory displacements between intracellular structures may explain the effects of low to medium intensity ultrasound on cells and tissues [107]. Such effects include modulation of action potentials in excitable tissues, modulation of angiogenesis, changes in membrane permeability and modulation of molecular expression. The authors constructed a linear model for a spherical object which is intended to approximate an intracellular structure such as a nucleus embedded within a homogeneous viscoelastic medium. Maximal amplitude vibrations are found in the sub-MHz range with the specific frequencies at which maximum oscillations occur being consistent with resonance phenomena. The authors suggested that the very small intracellular strain associated with these conditions, through a cyclic fatigue-like mechanism may be responsible for the biological effects.

As a first attempt to explain sub-cavitation threshold cellular acoustics [58], studies in which fish epidermis cells had been subjected to both cavitation-inducing 1-MHz, and non-cavitation inducing 3-MHz continuous-wave ultrasound [108] were re-examined. It was shown that there is a graded range of biological effects which includes behaviours that do not involve cavitation. The authors were also able to demonstrate ultrasound-induced changes to cellular organelles. The cellular response to ultrasound was attributed to the formation of gas bubbles inside the bilayer cell membrane, the so-called sonophore hypothesis [58].

In a follow-up study by the same group [97], real-time in-vitro microscopic studies were performed on cells subjected to uniform pulsed 1-MHz ultrasound with a 20% duty cycle and intensities of 1 W cm^{-2} and 2 W cm^{-2}, corresponding to hydrophone-measured acoustic pressure amplitudes of 170 kPa and 290 kPa, respectively. Substantial cytoskeletal changes and remodelling were evident at higher intensities corresponding to remarkably small strain values.

In a very recent study on the effect of low-intensity ultrasound and mesenchymal-epithelial (MET) signaling on cellular motility and morphology [109], continuous-wave low-intensity ultrasound of 200-kPa pressure amplitude at 960 kHz was applied to cells from a Madin–Darby canine kidney (MDCK) cell line. The putative basis for the effects on the MDCK cell membrane is the bilayer sonophore model whereby intramembrane cavitation occurs at moderate acoustic amplitudes. The authors have demonstrated that their setup results in modulation of the so-called MET tyrosine kinase signalling pathway which in turn modifies cell morphology and diminishes critical cancer cell behaviour such as motility. This may form the basis of novel cancer therapies.

The experimental studies in this section were performed at MI <0.3. Low-amplitude sonication causes subtle intracellular effects. Follow-up research must validate the sonophore hypothesis or provide an alternative explanation for the phenomena observed.

3. Conclusions

This article reviews those effects of ultrasound on living cells that do not include inertial cavitation, cellular effects due to the introduction of bubbles, and non-destructive structural evaluation through ultrasonic biomicroscopy.

The main effects witnessed in the publications reviewed in this article have been summarised in Table 1.

Table 1. Overview of publications on cellular ultrasonics in chronological order.

Cell Type	Frequency	Amplitude	Main Effect	Ref.
Newt notochord	1 MHz	8–15 W cm^{-2}	Disruption	[66]
Blood	2.25 MHz	30 mW	Chromosomal damage	[67]
Frog muscle	85 kHz	1–5 µm	Structure disruption	[68]
Elodea	0.45–10 MHz	75–180 mW cm^{-2}	Cell death	[71,72]
Platelets	1–10 MHz	0.5–76 kPa	Streaming	[75]
Platelets	1 MHz	0.2, 0.6 W cm^{-2}	Disruption	[76]
Erythrocytes	1 MHz	0–5 W cm^{-2}	Lysis	[77]
Erythrocytes	24 kHz	100 kPa–1 MPa	Permeation	[78]
HL-60	255 kHz	0.4 W cm^{-2}	Membrane changes	[79]
B. subtilis	22–67 kHz	20–60 W	Lysis	[80]
B. subtilis	40 kHz	25–38 µm	Lysis	[81]
Leukaemic	750 kHz	22.4–103.7 W cm^{-2}	Apoptosis	[82]
Platelets	22 kHz	1–8.8 W cm^{-2}	Aggregation	[95]
Endothelial		2.5 W cm^{-2}	Permeation	[83]
Leukaemic	1.8 MHz	7 mW mL^{-1}	Apoptosis	[84]
E. coli	1 MHz	5.2 W cm^{-2}	Eradication	[85]
S. cerevisiae	1 MHz	5.2 W cm^{-2}	Eradication	[85]
S. epidermidis	75 kHz	2 W cm^{-2}	Proliferation	[103]
E. coli	75 kHz	2 W cm^{-2}	Proliferation	[103]
P. aeruginosa	75 kHz	2 W cm^{-2}	Proliferation	[103]
Cornea	880 kHz	0.19–0.56 W cm^{-2}	Structural changes	[106]
Endothelial	0.5–5 MHz	1.2 W cm^{-2}	Proliferation	[104]
Bacterial spores	2–4 MHz		Translation	[96]
COS-7	3 MHz	0.85 MPa	Proliferation	[105]
Bacteria	40 kHz	240 mW cm^{-2}	Permeation	[86]
U937	1 MHz	0.3–0.5 W cm^{-2}	Apoptosis	[87]
Bacteria	40 kHz		Eradication	[88]
Bacteria	24 kHz	1500 W L^{-1}	Eradication	[89]
Anabaena sphaerica	200 kHz–2.2 MHz	40–68 kPa	Disruption	[90]
Microcystis aeruginosa	25 kHz	0.32 W mL^{-1}	Proliferation	[91]
Fish epidermis	3 MHz	2.2 W cm^{-2}	Organelle changes	[58,108]
HASM	1 MHz	1 W cm^{-2}, 2 W cm^{-2}	Cytoskeletal changes	[97]
Endothelial	1 MHz	50–300 kPa	Translation	[26]
Leukaemic	1 MHz	0.3–0.4 W cm^{-2}	DNA breakage	[92]
HeLa	1 MHz	0.3 W cm^{-2}	Permeation	[93]
MRC-5		0.1–10 W cm^{-2}	Lysis	[94]
Erythrocytes	1 MHz, 3 MHz	1–10 V	Translation	[99]
MCF-7, leukocytes	19.4 MHz	2 W cm^{-2}	Separation	[100,101]
CHO, HEK	7 MHz		Separation	[102]
MDCK	960 kHz	200 kPa	Morphology changes	[109]

Transient and permanent cell disruption dominate Table 1 with 22 out of 40 publications. However, these studies are included because the underlying mechanism for these effects in most cases do not appear to be due to inertial cavitation or to result directly from the introduction of bubbles, or because the nature of the effect is uncertain due to a paucity of information about the acoustic intensities. The remaining 18 papers describe more subtle effects at moderate intensities, such as translation (seven publications), internal changes (five publications), and proliferation (six publications).

Living cells under the influence of ultrasound may experience proliferation, translation, apoptosis, lysis, transient membrane permeation, and oscillation. Cytoskeletal and internal changes have been reported.

Future research will concentrate on finding lysis thresholds of different cell types, with the purpose of eradicating unwanted cells whilst leaving healthy, wanted, cells unharmed. Detectable differences in translation speeds of individual cells might be future acoustic identifiers of cancer or malaria. Cell proliferation is augmented by sonication at any frequency, which means that mechanical effects

are not a probable cause of the proliferation observed. Consequently, combined heating and vibrating of wounded tissue might be investigated as a means for accelerated healing. Moreover, the formation of sonophores needs to be validated or alternative explanations for intracellular changes in low-MI ultrasound fields must be explored. Ultrasound itself can manipulate and damage cells at low acoustic amplitudes. It is therefore worthwhile to develop truly noninvasive ultrasound-based therapeutic methods. The ultimate goal of cellular acoustics is the detection, quantification, manipulation and eradication of individual cells.

Author Contributions: N.A., C.S., J.P., and M.N. contributed; D.M.R. and M.P. wrote the paper.

Funding: This research received no external funding.

Conflicts of Interest: The authors declare no conflict of interest.

Abbreviations

The following abbreviations are used in this manuscript:

CHO	Chinese hamster ovary;
COS-7	CV-1 in origin simian line 7
DNA	deoxyribonucleic acid
DOX	doxorubicin
HASM	human airway smooth muscle
HEK	human embryonic kidney
HeLa	Henrietta Lacks
HIFU	high-intensity focussed ultrasound
HL	human leukaemia
MCF-7	Michigan Cancer Foundation cell line 7
MCLW	metal-clad leaky waveguide
MDCK	Madin–Darby canine kidney
MET	mesenchymal-epithelial
MI	mechanical index
MRC-5	Medical Research Council cell strain 5
PCR	polymerase chain reaction
pDNA	plasmid DNA
PNP	peak-negative pressure
PPP	peak-positive pressure
PRF	pulse-repetition frequency
PRT	pulse-repetition time
P2P	peak-to-peak pressure

References

1. ter Haar, G.R. HIFU tissue ablation: Concept and devices. In *Therapeutic Ultrasound*; Escoffre, J.M., Bouakaz, A., Eds.; Springer: Berlin, Germany, 2016; Volume 880, pp. 3–20. [CrossRef]
2. Eisenmenger, W. The mechanisms of stone fragmentation in ESWL. *Ultrasound Med. Biol.* **2001**, *27*, 683–693. [CrossRef]
3. Dimcevski, G.; Kotopoulis, S.; Bjånes, T.; Hoem, D.; Schjøtt, J.; Gjertsen, B.T.; Biermann, M.; Molven, A.; Sorbye, H.; McCormack, E.; et al. A human clinical trial using ultrasound and microbubbles to enhance gemcitabine treatment of inoperable pancreatic cancer. *J. Control. Release* **2016**, *243*, 172–181. [CrossRef] [PubMed]
4. Kaneko, Y.; Maruyama, T.; Takegami, K.; Watanabe, T.; Mitsui, H.; Hanajiri, K.; Nagawa, H.; Matsumoto, Y. Use of a microbubble agent to increase the effects of high intensity focused ultrasound on liver tissue. *Eur. Radiol.* **2005**, *15*, 1415–1420. [CrossRef] [PubMed]
5. van Wamel, A.; Sontum, P.C.; Healey, A.J.; Kvåle, S.; Bush, N.; Bamber, J.; de Lange Davies, C. Acoustic cluster therapy (ACT) enhances the therapeutic efficacy of paclitaxel and Abraxane for treatment of human prostate adenocarcinoma in mice. *J. Control. Release* **2016**, *236*, 15–21. [CrossRef] [PubMed]

6. van der Windt, D.A.; van der Heijden, G.J.; van den Berg, S.G.; ter Riet, G.; de Winter, A.F.; Bouter, L.M. Ultrasound therapy for musculoskeletal disorders: A systematic review. *Pain* **1999**, *81*, 257–271. [CrossRef]
7. Desmeules, F.; Boudreault, J.; Roy, J.S.; Dionne, C.; Frémont, P.; MacDermid, J.C. The efficacy of therapeutic ultrasound for rotator cuff tendinopathy: A systematic review and meta-analysis. *Phys. Ther. Sport* **2015**, *16*, 276–284. [CrossRef] [PubMed]
8. Harle, J.; Salih, V.; Mayia, F.; Knowles, J.C.; Olsen, I. Effects of ultrasound on the growth and function of bone and periodontal ligament cells in vitro. *Ultrasound Med. Biol.* **2001**, *27*, 579–586. [CrossRef]
9. Lim, K.; Kim, J.; Seonwoo, H.; Park, S.H.; Choung, P.H.; Chung, J.H. In vitro effects of low-intensity pulsed ultrasound stimulation on the osteogenic differentiation of human alveolar bone-derived mesenchymal stem cells for tooth tissue engineering. *BioMed Res. Int.* **2013**, *2013*, 269724. [CrossRef] [PubMed]
10. Nakao, J.; Fujii, Y.; Kusuyama, J.; Bandow, K.; Kakimoto, K.; Ohnishi, T.; Matsuguchi, T. Low-intensity pulsed ultrasound (LIPUS) inhibits LPS-induced inflammatory responses of osteoblasts through TLR4–MyD88 dissociation. *Bone* **2014**, *58*, 17–25. [CrossRef] [PubMed]
11. Schumann, D.; Kujat, R.; Zellner, J.; Angele, M.K.; Nerlich, M.; Mayr, E.; Angele, P. Treatment of human mesenchymal stem cells with pulsed low intensity ultrasound enhances the chondrogenic phenotype in vitro. *Biorheology* **2006**, *43*, 431–443. [PubMed]
12. Dalla-Bona, D.A.; Tanaka, E.; Inubushi, T.; Oka, H.; Ohta, A.; Okada, H.; Miyauchi, M.; Takata, T.; Tanne, K. Cementoblast response to low- and high-intensity ultrasound. *Arch. Oral Biol.* **2008**, *53*, 318–323. [CrossRef] [PubMed]
13. Takeuchi, R.; Ryo, A.; Komitsu, N.; Mikuni-Takagaki, Y.; Fukui, A.; Takagi, Y.; Shiraishi, T.; Morishita, S.; Yamazaki, Y.; Kumagai, K.; et al. Low-intensity pulsed ultrasound activates the phosphatidylinositol 3 kinase/Akt pathway and stimulates the growth of chondrocytes in three-dimensional cultures: A basic science study. *Arthrit. Res. Ther.* **2008**, *10*, R77. [CrossRef] [PubMed]
14. Bazou, D.; Maimon, N.; Munn, L.L.; Gonzalez, I. Effects of low intensity continuous ultrasound (LICU) on mouse pancreatic tumor explants. *Appl. Sci.* **2017**, *7*, 1275. [CrossRef]
15. Wiklund, M. Acoustofluidics 12: Biocompatibility and cell viability in microfluidic acoustic resonators. *Lab Chip* **2012**, *12*, 2018–2028. [CrossRef] [PubMed]
16. O'Brien, W.D., Jr. Ultrasound–biophysics mechanisms. *Prog. Biophys. Mol. Biol.* **2007**, *93*, 212–255. [CrossRef] [PubMed]
17. Wu, J.; Nyborg, W.L. Ultrasound, cavitation bubbles and their interaction with cells. *Adv. Drug Deliv. Rev.* **2008**, *60*, 1103–1116. [CrossRef] [PubMed]
18. Shankar, H.; Pagel, P.S. Potential adverse ultrasound-related biological effects: a critical review. *Anesthesiology* **2011**, *115*, 1109–1124. [CrossRef] [PubMed]
19. Izadifar, Z.; Babyn, P.; Chapman, D. Mechanical and biological effects of ultrasound: A review of present knowledge. *Ultrasound Med. Biol.* **2017**, *43*, 1085–1104. [CrossRef] [PubMed]
20. Tortora, G.J.; Derrickson, B.H. *Principles of Anatomy and Physiology*, 13th ed.; Wiley: Philadelphia, PA, USA, 2008.
21. Yang, T.; Bragheri, F.; Nava, G.; Chiodi, I.; Mondello, C.; Osellame, R.; Berg-Sørensen, K.; Cristiani, I.; Minzioni, P. A comprehensive strategy for the analysis of acoustic compressibility and optical deformability on single cells. *Sci. Rep.* **2016**, *6*, 23946. [CrossRef] [PubMed]
22. Tomlinson, M.J.; Tomlinson, S.; Yang, X.B.; Kirkham, J. Cell separation: terminology and practical considerations. *J. Tissue Eng.* **2013**, *4*, 2041–7314. [CrossRef] [PubMed]
23. Postema, M. *Fundamentals of Medical Ultrasonics*; Spon: London, UK, 2011; ISBN 978-1135-179-36-6.
24. Nowicki, A. *Ultradźwięki w medycynie: wprowadzenie do współczesnej ultrasonografii*; Instytut Podstawowych Problemów Techniki, Polska Akademia Nauk: Warszawa, Poland, 2010.
25. Postema, M.; Kotopoulis, S.; Jenderka, K.V. Basic physical principles of medical ultrasound. In *EFSUMB Course Book on Ultrasound*; Dietrich, C.F., Ed.; EFSUMB: London, UK, 2012; pp. 9–37.
26. Geffen, C.; Kimmel, E. The effect of low intensity ultrasound on adhesion molecules, actin monomers and membrane permeability in endothelial cells. In *Micro-Acoustics in Marine and Medical Research*; Kotopoulis, S., Delalande, A., Godø, O.R., Postema, M., Eds.; Institutt for fysikk og teknologi, Universitetet i Bergen: Bergen, Norway, 2012; pp. 131–170.
27. Dehoux, T.; Abi Ghanem, M.; Zouani, O.F.; Rampnoux, J.M.; Guillet, Y.; Dilhaire, S.; Durrieu, M.C.; Audoin, B. All-optical broadband ultrasonography of single cells. *Sci. Rep.* **2015**, *5*, 8650. [CrossRef] [PubMed]

28. Blase, C.; Bereiter-Hahn, J. Ultrasonic characterization of biological cells. In *Ultrasonic and Electromagnetic NDE for Structure and Material Characterization: Engineering and Biomedical Applications*; Kundu, T., Ed.; CRC: Boca Raton, FL, USA, 2012; pp. 689–722.
29. Silberrad, O. Propeller erosion. *Engineering* **1912**, *33*, 33–35.
30. Brennen, C.E. *Cavitation and Bubble Dynamics*; Oxford: New York, NY, USA, 1995.
31. Young, F.R. *Cavitation*; McGraw-Hill: New York, NY, USA, 1989.
32. Kondo, T.; Fukushima, Y.; Kon, H.; Riesz, P. Effect of shear stress and free radicals induced by ultrasound on erythrocytes. *Arch. Biochem. Biophys.* **1989**, *269*, 381–389. [CrossRef]
33. Riesz, P.; Kondo, T. Free radical formation induced by ultrasound and its biological implications. *Free Radic. Biol. Med.* **1992**, *13*, 247–270. [CrossRef]
34. Carstensen, E.L.; Kelly, P.; Church, C.C.; Brayman, A.A.; Child, S.Z.; Raeman, C.H.; Schery, L. Lysis of erythrocytes by exposure to CW ultrasound. *Ultrasound Med. Biol.* **1993**, *19*, 147–165. [CrossRef]
35. Dalecki, D. Mechanical bioeffects of ultrasound. *Cancer Res.* **2004**, *6*, 229–248. [CrossRef] [PubMed]
36. Rosenthal, I.; Sostaric, J.Z.; Riesz, P. Sonodynamic therapy—a review of the synergistic effects of drugs and ultrasound. *Ultrason. Sonochem.* **2004**, *11*, 349–363. [CrossRef] [PubMed]
37. Harvey, E.N.; Loomis, A.L. High frequency sound waves of small intensity and their biological effects. *Nature* **1928**, *121*, 622–624. [CrossRef]
38. Harvey, E.N.; Harvey, E.B.; Loomis, A.L. Further observations on the effect of high frequency sound waves on living matter. *Biol. Bull.* **1928**, *55*, 459–469. [CrossRef]
39. British Medical Ultrasound Society. Guidelines for the Safe Use of Diagnostic Ultrasound Equipment. *SAGE J.* **2000**, *18*, 52–59.
40. ter Haar, G. Safety and bio-effects of ultrasound contrast agents. *Med. Biol. Eng. Comput.* **2009**, *47*, 893–900. [CrossRef] [PubMed]
41. Postema, M.; Gilja, O.H. Contrast-enhanced and targeted ultrasound. *World J. Gastroenterol.* **2011**, *17*, 28–41. [CrossRef] [PubMed]
42. Voigt, J.U. Ultrasound molecular imaging. *Methods* **2009**, *48*, 92–97. [CrossRef] [PubMed]
43. Postema, M.; van Wamel, A.; Lancée, C.T.; de Jong, N. Ultrasound-induced encapsulated microbubble phenomena. *Ultrasound Med. Biol.* **2004**, *30*, 827–840. [CrossRef] [PubMed]
44. Heppner, P.; Lindner, J.R. Contrast ultrasound assessment of angiogenesis by perfusion and molecular imaging. *Expert Rev. Mol. Diagn.* **2005**, *5*, 447–455. [CrossRef] [PubMed]
45. Prentice, P.; Cuschieri, A.; Dholakia, K.; Prausnitz, M.; Campbell, P. Membrane disruption by optically controlled microbubble cavitation. *Nat. Phys.* **2005**, *1*, 107–110. [CrossRef]
46. Sundaram, J.; Mellein, B.R.; Mitragotri, S. An experimental and theoretical analysis of ultrasound-induced permeabilization of cell membranes. *Biophys. J.* **2003**, *84*, 3087–3101. [CrossRef]
47. Kudo, N.; Okada, K.; Yamamoto, K. Sonoporation by single-shot pulsed ultrasound with microbubbles adjacent to cells. *Biophys. J.* **2009**, *96*, 4866–4876. [CrossRef] [PubMed]
48. Keyhani, K.; Guzmán, H.R.; Parsons, A.; Lewis, T.N.; Prausnitz, M.R. Intracellular drug delivery using low-frequency ultrasound: Quantification of molecular uptake and cell viability. *Pharm. Res.* **2001**, *18*, 1514–1520. [CrossRef] [PubMed]
49. Postema, M.; Gilja, O.H. Ultrasound-directed drug delivery. *Curr. Pharm. Biotechnol.* **2007**, *8*, 355–361. [CrossRef] [PubMed]
50. Lee, N.G.; Berry, J.L.; Lee, T.C.; Wang, A.T.; Honowitz, S.; Murphree, A.L.; Varshney, N.; Hinton, D.R.; Fawzi, A.A. Sonoporation enhances chemotherapeutic efficacy in retinoblastoma cells in vitro. *Investig. Ophthalmol. Vis. Sci.* **2011**, *52*, 3868–3873. [CrossRef] [PubMed]
51. Delalande, A.; Postema, M.; Mignet, N.; Midoux, P.; Pichon, C. Ultrasound and microbubble-assisted gene delivery: recent advances and ongoing challenges. *Therap. Deliv.* **2012**, *3*, 1199–1215. [CrossRef]
52. Kaufman, G.E.; Miller, M.W.; Griffiths, T.D.; Ciaravino, V.; Carstensen, E.L. Lysis and viability of cultured mammalian cells exposed to 1 MHz ultrasound. *Ultrasound Med. Biol.* **1977**, *3*, 21–25. [CrossRef]
53. Brayman, A.A.; Coppage, M.L.; Vaidya, S.; Miller, M.W. Transient poration and cell surface receptor removal from human lymphocytes in vitro by 1 MHz ultrasound. *Ultrasound Med. Biol.* **1999**, *25*, 999–1008. [CrossRef]
54. Firestein, F.; Rozenszajn, L.A.; Shemesh-Darvish, L.; Elimelech, R.; Radnay, J.; Rosenschein, U. Induction of apoptosis by ultrasound application in human malignant lymphoid cells: role of mitochondria-caspase pathway activation. *Ann. N. Y. Acad. Sci.* **2003**, *1010*, 163–166. [CrossRef] [PubMed]

55. Duvshani-Eshet, M.; Machluf, M. Therapeutic ultrasound optimization for gene delivery: A key factor achieving nuclear DNA localization. *J. Control. Release* **2005**, *108*, 513–528. [CrossRef] [PubMed]
56. Delalande, A.; Kotopoulis, S.; Rovers, T.; Pichon, C.; Postema, M. Sonoporation at a low mechanical index. *Bubble Sci. Eng. Technol.* **2011**, *3*, 3–12. [CrossRef]
57. Johansen, K.; Kimmel, E.; Postema, M. Theory of red blood cell oscillations in an ultrasound field. *Arch. Acoust.* **2017**, *42*, 121–126. [CrossRef]
58. Krasovitski, B.; Frenkel, V.; Shoham, S.; Kimmel, E. Intramembrane cavitation as a unifying mechanism for ultrasound-induced bioeffects. *Proc. Natl Acad. Sci. USA* **2011**, *108*, 3258–3263. [CrossRef] [PubMed]
59. Johansen, K.; Postema, M. Lagrangian formalism for computing oscillations of spherically symmetric encapsulated acoustic antibubbles. *Hydroacoustics* **2016**, *19*, 197–208.
60. Shamloo, A.; Boodaghi, M. Design and simulation of a microfluidic device for acoustic cell separation. *Ultrasonics* **2018**, *84*, 234–243. [CrossRef] [PubMed]
61. Leighton, T.G. *The Acoustic Bubble*; Academic: London, UK, 1994.
62. Shi, J.; Ahmed, D.; Mao, X.; Lin, S.C.S.; Lawit, A.; Huang, T.J. Acoustic tweezers: Patterning cells and microparticles using standing surface acoustic waves (SSAW). *Lab Chip* **2009**, *9*, 2890–2895. [CrossRef] [PubMed]
63. Dayton, P.A.; Morgan, K.E.; Klibanov, A.L.; Brandenburger, G.; Nightingale, K.R.; Ferrara, K.W. A preliminary evaluation of the effects of primary and secondary radiation forces on acoustic contrast agents. *IEEE Trans. Ultrason. Ferroelectr. Freq. Control* **1997**, *44*, 1264–1277. [CrossRef]
64. Duckhouse, H.; Mason, T.J.; Phull, S.S.; Lorimer, J.P. The effect of sonication on microbial disinfection using hypochlorite. *Ultrason. Sonochem.* **2004**, *11*, 173–176. [CrossRef] [PubMed]
65. Trampuz, A.; Piper, K.E.; Hanssen, A.D.; Osmon, D.R.; Cockerill, F.R.; Steckelberg, J.M.; Patel, R. Sonication of explanted prosthetic components in bags for diagnosis of prosthetic joint infection is associated with risk of contamination. *J. Clin. Microbiol.* **2006**, *44*, 628–631. [CrossRef] [PubMed]
66. Selman, G.G.; Jurand, A. An electron microscope study of the endoplasmic reticulum in Newt notochord cells after disturbance with ultrasonic treatment and subsequent regeneration. *J. Cell Biol.* **1964**, *20*, 175–183. [CrossRef] [PubMed]
67. Macintosh, I.J.C.; Davey, D.A. Chromosome aberrations induced by an ultrasonic fetal pulse detector. *Br. Med. J.* **1970**, *4*, 92–93. [CrossRef] [PubMed]
68. Ravitz, M.J.; Schnitzler, R.M. Morphological changes induced in the frog semitendinosus muscle fiber by localized ultrasound. *Exp. Cell Res.* **1970**, *60*, 78–85. [CrossRef]
69. Miller, M.W.; Voorhees, S.M.; Carstensen, E.L.; Eames, F.A. An histological study of the effect of ultrasound on growth of Vicia faba roots. *Radiat. Bot.* **1974**, *14*, 201–206. [CrossRef]
70. Miller, M.W. Comparison of micronuclei induction for X-ray and ultrasound exposures of Vicia faba root meristem cells. *Ultrasound Med. Biol.* **1978**, *4*, 267. [CrossRef]
71. Miller, D.L. Cell death thresholds in *Elodea* for 0.45–10 MHz ultrasound compared to gas-body resonance theory. *Ultrasound Med. Biol.* **1979**, *5*, 351–357. [CrossRef]
72. Miller, D.L. A cylindrical-bubble model for the response of plant-tissue gas bodies to ultrasound. *J. Acoust. Soc. Am.* **1979**, *65*, 1313–1321. [CrossRef]
73. Dyer, H.J.; Nyborg, W.L. Ultrasonically-induced movements in cells and cell models. *IRE Trans. Med. Electron.* **1960**, 163–165. [CrossRef]
74. Gershoy, A.; Nyborg, W.L. Perturbation of plant-cell contents by ultrasonic micro-irradiation. *J. Acoust. Soc. Am.* **1973**, *54*, 1356–1367. [CrossRef]
75. Trenchard, P.M. Ultrasound-induced orientation of discoid platelets and simultaneous changes in light transmission: preliminary characterisation of the phenomenon. *Ultrasound Med. Biol.* **1987**, *13*, 183–195. [CrossRef]
76. Williams, A.R.; Sykes, S.M.; O'Brien, W.D., Jr. Ultrasonic exposure modifies platelet morphology and function in vitro. *Ultrasound Med. Biol.* **1977**, *2*, 311–317. [CrossRef]
77. Miller, M.W.; Azadniv, M.; Doida, Y.; Brayman, A.A. Effect of a stabilized microbubble contrast agent on CW ultrasound induced red blood cell lysis in vitro. *Echocardiogr. J.* **1995**, *12*, 1–11. [CrossRef]
78. Liu, J.; Lewis, T.N.; Prausnitz, M.R. Non-invasive assessment and control of ultrasound-mediated membrane permeabilization. *Pharm. Res.* **1998**, *15*. [CrossRef]

79. Tachibana, K.; Uchida, T.; Ogawa, K.; Yamashita, N.; Tamura, K. Induction of cell-membrane porosity by ultrasound. *Lancet* **1999**, *353*, 1409. [CrossRef]
80. Belgrader, P.; Hansford, D.; Kovacs, G.T.A.; Venkateswaran, K.; Mariella, R., Jr.; Milanovich, F.; Nasarabadi, S.; Okuzumi, M.; Pourahmadi, F.; Northrup, M.A. A minisonicator to rapidly disrupt bacterial spores for DNA analysis. *Anal. Chem.* **1999**, *71*, 4232–4236. [CrossRef] [PubMed]
81. Taylor, M.T.; Belgrader, P.; Furman, B.J.; Pourahmadi, F.; Kovacs, G.T.A.; Northrup, M.A. Lysing bacterial spores by sonication through a flexible interface in a microfluidic system. *Anal. Chem.* **2001**, *73*, 492–496. [CrossRef] [PubMed]
82. Ashush, H.; Rozenszajn, L.A.; Blass, M.; Barda-Saad, M.; Azimov, D.; Radnay, J.; Zipori, D.; Rosenschein, U. Apoptosis induction of human myeloid leukemic cells by ultrasound exposure. *Cancer Res.* **2000**, *60*, 1014–1020. [PubMed]
83. Taniyama, Y.; Tachibana, K.; Hiraoka, K.; Namba, T.; Yamasaki, K.; Hashiya, N.; Aoki, M.; Ogihara, T.; Yasufumi, K.; Morishita, R. Local delivery of plasmid DNA into rat carotid artery using ultrasound. *Circulation* **2002**, *105*, 1233–1239. [CrossRef] [PubMed]
84. Lagneaux, L.; Delforge, A.; Dejeneffe, M.; Massy, M.; Moerman, C.; Hannecart, B.; Canivet, Y.; Lepeltier, M.F.; Bron, D. Ultrasonic low-energy treatment: A novel approach to induce apoptosis in human leukemic cells. *Exp. Hematol.* **2002**, *30*, 1293–1301. [CrossRef]
85. Li, G.; Xiao, H.; Glo, M.; Cheg, J. Miniaturized cell lysis device using spherically focused ultrasound. *Tsinghua Sci. Technol.* **2003**, *8*, 487–492.
86. Song, Y.; Hahn, T.; Thompson, I.P.; Mason, T.J.; Preston, G.M.; Li, G.; Paniwnyk, L.; Huang, W.E. Ultrasound-mediated DNA transfer for bacteria. *Nucleic Acids Res.* **2007**, *35*, e129-1–e129-9. [CrossRef] [PubMed]
87. Yoshida, T.; Kondo, T.; Ogawa, R.; Feril, L.B.; Zhao, Q.L.; Watanabe, A.; Tsukada, K. Combination of doxorubicin and low-intensity ultrasound causes a synergistic enhancement in cell killing and an additive enhancement in apoptosis induction in human lymphoma U937 cells. *Cancer Chemother. Pharmacol.* **2008**, *61*, 559–567. [CrossRef] [PubMed]
88. Monsen, T.; Lövgren, E.; Widerström, M.; Wallinder, L. In vitro effect of ultrasound on bacteria and suggested protocol for sonication and diagnosis of prosthetic infections. *J. Clin. Microbiol.* **2009**, *47*, 2496–2501. [CrossRef] [PubMed]
89. Drakopoulou, S.; Terzakis, S.; Fountoulakis, M.S.; Mantzavinos, D.; Manios, T. Ultrasound-induced inactivation of gram-negative and gram-positive bacteria in secondary treated municipal wastewater. *Ultrason. Sonochem.* **2009**, *16*, 629–634. [CrossRef] [PubMed]
90. Kotopoulis, S.; Schommartz, A.; Postema, M. Sonic cracking of blue-green algae. *Appl. Acoust.* **2009**, *70*, 1306–1312. [CrossRef]
91. Zhang, G.; Zhang, P.; Liu, H.; Wang, B. Ultrasonic damages on cyanobacterial photosynthesis. *Ultrason. Sonochem.* **2006**, *13*, 501–505. [CrossRef] [PubMed]
92. Furusawa, Y.; Fujiwara, Y.; Campbell, P.; Zhao, Q.L.; Ogawa, R.; Hassan, M.A.; Tabuchi, Y.; Takasaki, I.; Takahashi, A.; Kondo, T. DNA double-strand breaks induced by cavitational mechanical effects of ultrasound in cancer cell lines. *PLoS ONE* **2012**, *7*, e29012. [CrossRef] [PubMed]
93. Hassan, M.A.; Ahmed, I.S.; Campbell, P.; Kondo, T. Enhanced gene transfection using calcium phosphate co-precipitates and low-intensity pulsed ultrasound. *Eur. J. Pharm. Sci.* **2012**, *47*, 768–773. [CrossRef] [PubMed]
94. Ly, M.; Lu, F.; Maheshwari, G.; Subramanian, S. Microscale acoustic disruption of mammalian cells for intracellular product release. *J Biotechnol.* **2014**, *184*, 146–153. [CrossRef] [PubMed]
95. Samal, A.B.; Adzerikho, I.D.; Mrochek, A.G.; Loiko, E.N. Platelet aggregation and change in intracellular Ca^{2+} induced by low frequency ultrasound in vitro. *Eur. J. Ultrasound* **2000**, *11*, 53–59. [CrossRef]
96. Zourob, M.; Hawkes, J.J.; Coakley, W.T.; Treves Brown, B.J.; Fielden, P.R.; McDonnell, M.B.; Goddard, N.J. Optical leaky waveguide sensor for detection of bacteria with ultrasound attractor force. *Anal. Chem.* **2005**, *77*, 6163–6168. [CrossRef] [PubMed]
97. Mizrahi, N.; Zhou, E.H.; Lenormand, G.; Krishnan, R.; Weihs, D.; Butler, J.P.; Weitz, D.A.; Fredberg, J.J.; Kimmel, E. Low intensity ultrasound perturbs cytoskeleton dynamics. *Soft Matter* **2012**, *8*, 2438–2443. [CrossRef] [PubMed]

98. Hawkes, J.J.; Limaye, M.S.; Coakley, W.T. Filtration of bacteria and yeast by ultrasound-enhanced sedimentation. *J. Appl. Microbiol.* **1997**, *82*, 39–47. [CrossRef] [PubMed]
99. Mazzawi, N.; Postema, M.; Kimmel, E. Bubble-like response of living blood cells and microparticles in an ultrasound field. *Acta Phys. Pol. A* **2015**, *127*, 103–105. [CrossRef]
100. Ding, X.; Peng, Z.; Lin, S.C.S.; Geri, M.; Li, S.; Li, P.; Chen, Y.; Dao, M.; Suresh, S.; Huang, T.J. Cell separation using tilted-angle standing surface acoustic waves. *Proc. Natl Acad. Sci. USA* **2014**, *11*, 12992–12997. [CrossRef] [PubMed]
101. Li, P.; Mao, Z.; Peng, Z.; Zhou, L.; Chen, Y.; Huang, P.H.; Truica, C.I.; Drabick, J.J.; El-Deiry, W.S.; Dao, M.; et al. Acoustic separation of circulating tumor cells. *Proc. Natl Acad. Sci. USA* **2015**, *112*, 4970–4975. [CrossRef] [PubMed]
102. Walther, T.; Postema, M. Device for the Identification, Separation and/or Cell Type-Specific Manipulation of at Least One Cell of a Cellular System. U.S. Patent 14476187, 3 September 2014.
103. Pitt, W.G.; Ross, S.A. Ultrasound increases the rate of bacterial cell growth. *Biotechnol. Prog.* **2003**, *19*, 1038–1044. [CrossRef] [PubMed]
104. Raz, D.; Zaretsky, U.; Einav, S.; Elad, D. Cellular alterations in cultured endothelial cells exposed to therapeutic ultrasound irradiation. *Endothelium* **2005**, *12*, 201–213. [CrossRef] [PubMed]
105. Hultström, J.; Manneberg, O.; Dopf, K.; Hertz, H.M.; Brismar, H.; Wiklund, M. Proliferation and viability of adherent cells manipulated by standing-wave ultrasound in a microfluidic chip. *Ultrasound Med. Biol.* **2007**, *33*, 145–151. [CrossRef] [PubMed]
106. Zderic, V.; Clark, J.I.; Vaezy, S. Drug delivery into the eye with the use of ultrasound. *J. Ultrasound Med.* **2004**, *23*, 1349–1359. [CrossRef] [PubMed]
107. Or, M.; Kimmel, E. Modeling linear vibration of cell nucleus in low intensity ultrasound field. *Ultrasound Med. Biol.* **2009**, *35*, 1015–1025. [CrossRef] [PubMed]
108. Frenkel, V.; Kimmel, E.; Iger, Y. Ultrasound-facilitated transport of silver chloride (AgCl) particles in fish skin. *J. Control. Release* **2000**, *68*, 251–261. [CrossRef]
109. Mazzawi, N.; Kimmel, E.; Tsarfaty, I. The effect of low-intensity ultrasound and met signaling on cellular motility and morphology. *Appl. Acoust.* **2019**, *143*, 1–6. [CrossRef]

PUBLICATION
II

Asymmetric oscillations of endoskeletal antibubbles

N. Kudo, R. Uzbekov, R. Matsumoto, R.-i. Shimizu, C. S. Carlson, N. Anderton, A. Deroubaix, C. Penny, A. T. Poortinga, D. M. Rubin, A. Bouakaz, and M. Postema

Japanese Journal of Applied Physics, vol. 59, no. SK, SKKE02
DOI: 10.35848/1347-4065/ab79e7

Asymmetric oscillations of endoskeletal antibubbles

Nobuki Kudo, Rustem Uzbekov, Ryunosuke Matsumoto, Ri-Ichiro Shimizu, Craig Stuart Carlson, Nicole Anderton, Aurélie Deroubaix, Clement Penny, Albert Thijs Poortinga, David Milton Rubin, et al.

Asymmetric oscillations of endoskeletal antibubbles

Nobuki Kudo[1]*, Rustem Uzbekov[2,3], Ryonosuke Matsumoto[1], Ri-ichiro Shimizu[1], Craig S. Carlson[4], Nicole Anderton[4], Aurélie Deroubaix[5], Clement Penny[5], Albert T. Poortinga[6], David M. Rubin[4], Ayache Bouakaz[7], and Michiel Postema[4]

[1]*Faculty of Information Science and Technology, Hokkaido University, Kita 14 Chome, Nishi 9 Jo, Kita-ku, Sapporo, Hokkaido 060-0814, Japan*

[2]*Department of Microscopy, Faculty of Medicine, University of Tours, 10 Boulevard Tonnellé, 37000 Tours, France*

[3]*Faculty of Bioengineering and Bioinformatics, Moscow State University, ul. Leninskiye Gory 1/73, Moscow 119192, Russia*

[4]*School of Electrical and Information Engineering, University of the Witwatersrand, Johannesburg, 1 Jan Smuts Laan, 2001 Braamfontein, South Africa*

[5]*Department of Internal Medicine, University of the Witwatersrand, Johannesburg, 7 York Road, 2193 Parktown, South Africa*

[6]*Department of Mechanical Engineering, Eindhoven University of Technology, De Zaale, 5600 MB Eindhoven, Netherlands*

[7]*Inserm U1253, Faculty of Medicine, University of Tours, 10 Boulevard Tonnellé, 37000 Tours, France*

Antibubbles have been under investigation as potential vehicles in ultrasound-guided drug delivery. It is assumed that antibubbles can expand unhampered, but cannot contract beyond the size of their inner core. In this study, this hypothesis was tested on endoskeletal antibubbles and reference bubbles. These were subjected to 3-cycle pulses of 1-MHz ultrasound, whilst being recorded with a high-speed camera operating at 10 million frames per second. At low acoustic amplitudes (200 kPa), antibubbles and bubbles oscillated symmetrically. At high acoustic amplitudes (1.00 MPa), antibubbles and bubbles oscillated asymmetrically, but antibubbles significantly more so than bubbles. Furthermore, fragmentation and core release were observed at these amplitudes. This finding may have implications for ultrasound-guided drug delivery using antibubbles.

Ultrasound contrast agents comprise suspensions of micrometer-sized gas bubbles, each surrounded by a stabilising shell.[1)] In ultrasound fields, these so-called microbubbles oscillate, *i.e.*, they subsequently expand and contract, creating a secondary sound field that can be detected with imaging equipment. Consequently, injections of ultrasound contrast agents have been utilised for diagnostic medical imaging.[2–4)] Oscillating microbubbles may interact with living cells and tissue.[5–7)] Therefore, ultrasound contrast agents have also, more recently, been

*E-mail: kudo@ist.hokudai.ac.jp

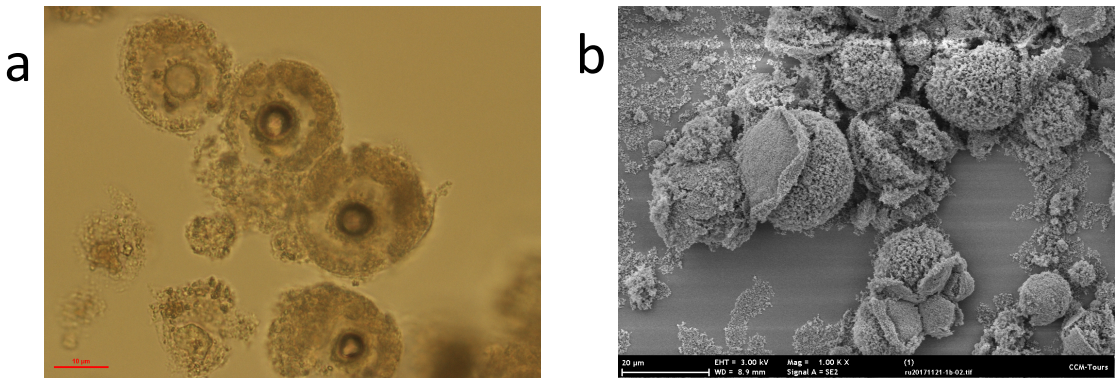

Fig. 1. Brightfield microscopic image of four endoskeletal antibubbles, with approximate inner droplet diameters of 5 μm (a). The scaling bar corresponds to 10 μm. Scanning electron microscope image of an endoskeletal antibubble (b). Ruptured silica membranes reveal skeletal structures underneath. The scaling bar corresponds to 20 μm. This image is a zoomed-out version of Fig. 1 in Ref. 21.

introduced in therapeutic settings.[8–10] One of the most popular ways to study microbubbles subjected to ultrasound is with high-speed photography.[11–14]

Antibubbles are gas bubbles in suspension containing a liquid core droplet. Antibubbles with surfactant interfaces are short-lived, with drainage times within 1000 seconds.[15,16] By adding nanoparticles to the interfaces, antibubbles can be produced with long lifespans.[17,18] Antibubbles have been produced with microfluidics, too.[19] Please note that these droplets are suspending inside the bubbles owing to electrostatic forces. By adding a hydrophobic endoskeleton, the droplets can be fixed in position inside the bubble. Endoskeletal antibubbles have been recently demonstrated.[21] This study follows up by showing full results of endoskeletal antibubble dynamics.

Figure 1a shows a brightfield microscopic image of endoskeletal antibubbles in EPON resin. The top halves of the bubbles had been cut off with a diamond knife without violating the integrity of the antibubbles. Four antibubbles contain a single droplet core of approximately 5-μm diameter. The endoskelotons themselves are shown in Figure 1b. The silica particles on the outer interface have been reported to form a single elastic layer.[22] The same batch of the antibubbles used to create Figure 1 has been used for the experiments described in this paper.

Shortly after the first high-speed camera observation of ultrasonic antibubbles, they were proposed as a vehicle to carry drugs to a region of interest, to be released using clinical ultrasound.[20] Antibubbles have proven to be suitable ultrasound contrast agents for harmonic imaging, as well.[22] The unique harmonic features of antibubbles have been attributed to the assumption that antibubbles can expand unhampered, but cannot contract beyond the size of their inner core.[23] In a simulation study, the outward expansion was shown to surpass that

of bubbles without a core droplet, whilst the contraction of antibubbles is less than that of bubbles without core droplets.[24)]

Antibubbles have a higher resonance frequency than their bubble counterparts.[25)] By modifying eq. (2.2.7) in Ref. 25 to contain the entire volumetric incompressible content V_i and ignoring the presence of an outer elastic shell, the linear resonance frequency f_r of the endoskeletal antibubble becomes:

$$f_\mathrm{r} = \frac{1}{2\pi R_0\sqrt{\rho}}\sqrt{\frac{3\gamma\left(p_0 - p_\mathrm{v} + \frac{2\sigma}{R_0}\right)}{1 - \frac{3V_\mathrm{i}}{4\pi R_0^3}} - \frac{2\sigma}{R_0} - \frac{4\eta^2}{R_0^2\rho}}, \tag{1}$$

where p_0 is the ambient pressure, p_v is the vapour pressure, R_0 is the equilibrium bubble radius, γ is the polytropic exponent of the gas, η is the liquid viscosity, ρ is the liquid density, and σ is the surface tension. Obviously, $0 \leq V_\mathrm{i} < \frac{4}{3}\pi R_0^3$. Thus, the presence of an endoskeleton increases the resonance frequency even more.

Two media containing (anti)bubbles were prepared for evaluation, as previously published.[18,22)] For stabilisation, Aerosil® R972 hydrophobised silica particles (Evonik Industries AG, Essen, Germany) were used.[22)]

For the first medium, hereafter referred to as AB, the aqueous cores were replaced by 2 vol% of hydrophobically modified Zano 10 Plus zinc oxide nanoparticles (Umicore, Brussel, Belgium). Instead of the formation of just droplets inside antibubbles, adding nanoparticles creates an endoskeletal structure with one or multiple voids that can be liquid-filled.[17,18,21)]

The second medium was left without cores, so it contained stabilised bubbles instead of antibubbles. This medium served as reference medium, hereafter referred to as REF.

For each medium, 5 mg of freeze-dried material was deposited into a FALCON® 15 mL High-Clarity Polypropylene Conical Tube (Corning Science México S.A. de C.V., Reynosa, Tamaulipas, Mexico), after which 5 mL of 049-16797 Distilled Water (FUJIFILM Wako Pure Chemical Corporation, Chuo-Ku, Osaka, Japan) was added.

Each emulsion was gently shaken by hand for 1 minute, after which 200 μL was pipetted into the observation chamber of a high-speed observation system.[26)] The observation chamber was placed under an Eclipse Ti inverted microscope (Nikon Corporation, Minato-ku, Tokyo, Japan) with a Plan Apo LWD 40× WI (N.A. 0.8) objective lens. Attached to the microscope was an HPV-X2 high-speed camera (Shimadzu, Nakagyo-ku, Kyoto, Japan), operating at 10 million frames per second.[27)]

During camera recording, the materials were subjected to ultrasound pulses, each comprising 3 cycles with a centre transmitting frequency of 1.00 MHz and a peak-negative pressure

of 200 kPa (1 V input) or 1.00 MPa (5 V input), from a laboratory-assembled single-element transducer.[26,27)]

The transducer was driven by a signal generated by an AFG320 arbitrary function generator (Sony-Tektronix, Shinagawa-ku, Tokyo, Japan) and amplified by a UOD-WB-1000 wide-band power amplifier (TOKIN Corporation, Shiroishi, Miyagi, Japan).

The videos recorded were segmented and analysed using MATLAB® (The MathWorks, Inc., Natick, MA, USA). In the first frame of each video, objects in the field of view were identified. These were then automatically sized throughout the rest of the video, resulting in radius(time) curves. For each radius(time) curve, the equilibrium radius, R_0, the maximum radius during the first cycle, $R_{\max}$, and the first minimum radius after the transient phase, $R_{\min}$, were determined. From these, positive excursion, $\xi^+ = (R_{\max} - R_0)$, and negative excursion, $\xi^- = (-R_{\min} + R_0)$, were determined, yielding the absolute oscillation asymmetry $(\xi^+ - \xi^-) = (R_{\max} + R_{\min} - 2R_0)$. Although $(\xi^+ - \xi^-) = (R_{\max} + R_{\min} - 2R_0)$ is a direct quantifyer of asymmetry, it must be noted that the values measured are greatly influenced by the accuracy of determining R_0.

Brightfield microscope z-stack galleries were captured using the brightfield component of a ZEISS LSM 780 confocal laser scanning microscope with an alpha Plan-Apochromat 63×/1.40 NA Oil CorrM27 objective lens (Carl Zeiss AG, Oberkochen, Germany).

Figure 2 shows a z-stack of brightfield microscopy images of an endoskeletal antibubble. In the focal plane (middle frame) and the planes right above and below focus, droplets of diameters less than 1 μm can be observed, indicated by dark spots, as well as entrapped gas cavities, indicated by white spots. In brightfield microscopy, denser regions appear darker, whilst less dense regions appear brighter.[28)] The space between the hydrophobised zinc oxide endoskeleton and the hydrophobised silica membrane is a gaseous void, shown as a white ring in frames 4–6.

Figure 3 shows the equilibrium radius R_0 versus the maximum expansion $R_{\max}$ and contraction $R_{\min}$ measured from a total of thirty-three high-speed videos with 118 AB and 144 REF, for acoustic pressure amplitudes of 200 kPa and 1.00 MPa. At 200-kPa acoustic amplitude, REF has slightly higher excursions than AB. At 1.00-MPa amplitude, AB has substantially greater expansion ($R_{\max} = 1.5R_0 + 1.5\ \mu$m), whereas REF has greater contraction ($R_{\min} = 0.57R_0 + 0.07\ \mu$m).

l This is even more evident from the difference in least-squares solutions. At 200-kPa amplitude, for both AB and REF, $(\xi^+ - \xi^-) \approx 0$, *i.e.*, both oscillate symmetrically despite occasional asymmetry. However, at 1.00-MPa amplitude, for AB: $(\xi^+ - \xi^-) = 0.30R_0 +$

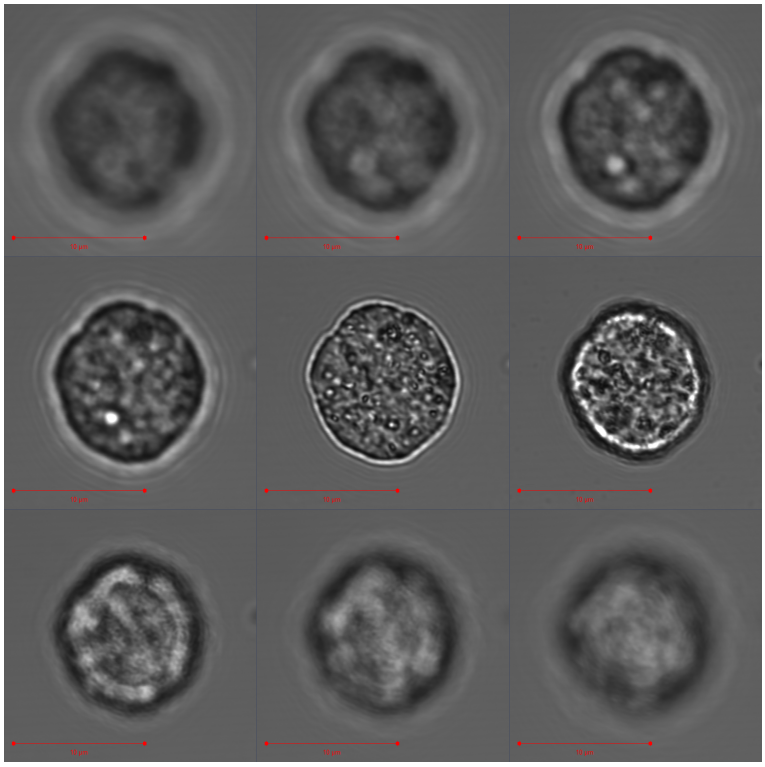

Fig. 2. Brightfield microscopy z-stack gallery of AB, captured over a 24-μm range at 3-μm intervals. The scaling bars correspond to 10 μm. Frames run from left–right, top–bottom.

1.2 μm, whereas for REF, $(\xi^+ - \xi^-) = 0.20R_0 + 1.5\ \mu$m. Thus, although both AB and REF oscillate asymmetrically, AB oscillates significantly more asymmetrically than REF.

It must be noted that the resonance frequency of these endoskeletal antibubbles must be substantially greater than 1 MHz.[23] Consequently, treating the maximum and minimum expansion as a linear case is justified.

Interestingly, in the same high-amplitude regime, the antibubbles can be observed to release their core contents. Figure 4 shows 4 frames selected from 256 frames of a high-speed video with AB sonicated at a 1.00-MPa amplitude. After the first oscillation cycle, the surface instabilities leading to fragmentation can be clearly seen. After sonication, the antibubble fragments were scattered around the remains of a bubble. This bubble remained acoustically active during subsequent pulses (not shown).

While low-amplitude pulses did not change the contents of the antibubble,[21] a short high-amplitude pulse could disrupt antibubbles within three cycles.

The high-speed videos confirm the expansion-only hypothesis at 1-MPa acoustic amplitude at a transmitting frequency of 1 MHz.

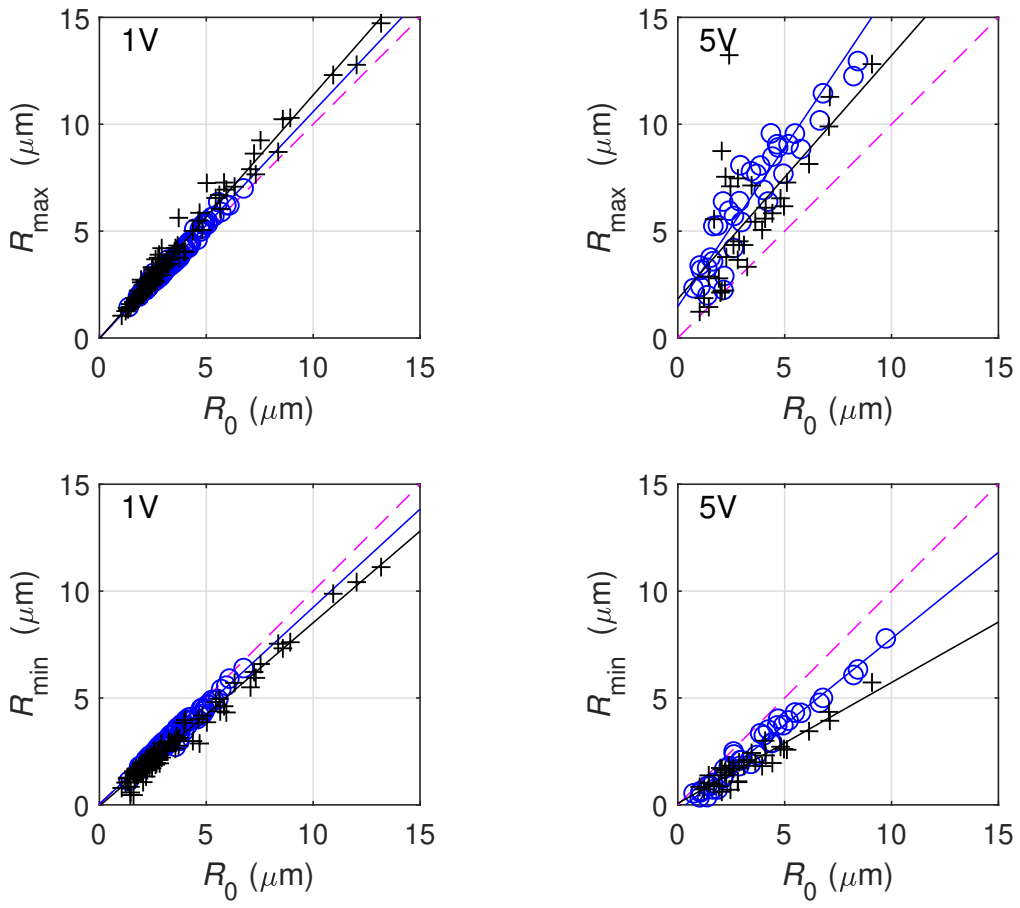

Fig. 3. Equilibrium radius R_0 versus maximum expansion R_{max} (top) and contraction R_{min} (bottom), for acoustic pressure amplitudes of 200 kPa (1V, left) and 1.00 MPa (5V, right). The dashed purple lines correspond to $R_{m*} = R_0$, the blue and black lines represent the least-squares solutions for AB (o) and REF (+), respectively.

One short, high-amplitude pulse appeared to be enough to shatter antibubbles and release their core contents. This finding may have implications for ultrasound-guided drug delivery using antibubbles.

Acknowledgements The scanning electron microscope data were obtained with the aid of the IBiSA Electron Microscopy Facility of the University of Tours and the University Hospital of Tours. Laser scanning confocal microscopy was performed at the Life Sciences Imaging Facility of the University of the Witwatersrand, Johannesburg. This work has been supported by JSPS KAKENHI Grant Number 17H00864.

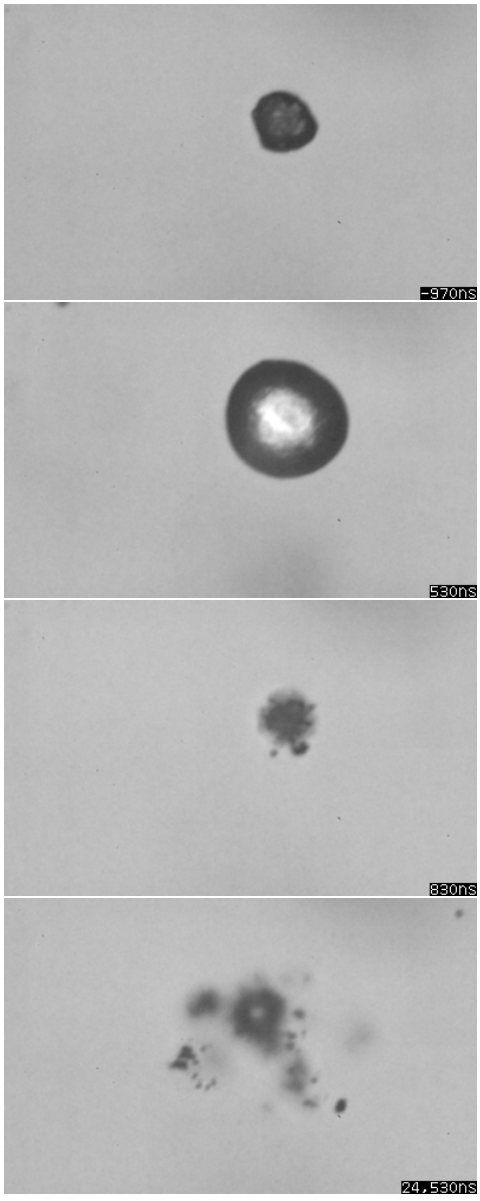

Fig. 4. Four high-speed frames of sonicated AB. Top-bottom: before sonication; during the first rarefactional peak; fragmentation during contraction; after sonication. Each frame width corresponds to 145 μm. Time stamps relative to ultrasound arrival indicate −970 ns, 530 ns, 830 ns, and 24,530 ns.

References

1) V. Paefchen, D. Doleschel, and F. Kiessling, Front. Pharmacol. **6** 197 (2015).
2) S. Ishikura, M. Yoshizawa, N. Tagawa, and T. Irie, Jpn. J. Appl. Phys. **57** 07LF20 (2018).
3) R. R. Wildeboer, R. J. G. van Sloun, P. Huang, H. Wijkstra, and M. Mischi, Ultrasound Med. Biol. **45** 2713 (2019).
4) J. Quan, Y. Hong, X. Zhang, M. Mei, X. You, and P. Huang, Clin. Hemorheol. Microcirc. **72** 293 (2019).
5) R. Oitate, A. Shimomura, H. Wada, T. Mochizuki, K. Masuda, Y. Oda, R. Suzuki, and K. Maruyama, Jpn. J. Appl. Phys. **56** 07JF25 (2017).
6) R. Oitate, T. Otsuka, M. Seki, A. Furutani, T. Mochizuki, K. Masuda, R. Suzuki, and K. Murayama, Jpn. J. Appl. Phys. **57** 07LF10 (2018).
7) T. Sato and K. Ikeda, Jpn. J. Appl. Phys. **57** 07LF16 (2018).
8) S. Kotopoulis, G. Dimcevski, O. H. Gilja, D. Hoem, and M. Postema, Med. Phys. **40** 072902 (2013).
9) R. H. Rahayu, K. Takanashi, T. T. K. Soon, I. Seviaryna, R. Maev, K. Kobayashi, N. Hozumi, and S. Yoshida, Jpn. J. Appl. Phys. **56** 07LF26 (2017).
10) Wang G, Li Q, Chen D, Wu B, Wu Y, Tong W, and Huang P. Theranostics **9** 6191 (2019).
11) M. Postema, A. van Wamel, F. J. ten Cate, and N. de Jong, Med. Phys. **32** 3707 (2005).
12) K. Suzuki, R. Iwasaki, R. Takagi, S. Yoshizawa, and S. Umemura, Jpn. J. Appl. Phys. **56** 07JF27 (2017).
13) N. Okada, M. Shiiba, S. Yamauchi, T. Sato, and S. Takeuchi, Jpn. J. Appl. Phys. **57** 07LE15 (2018).
14) S. Nishitaka, D. Mashiko, S. Yoshizawa, and S. Umemura, Jpn. J. Appl. Phys. **57** 07LF25 (2018).
15) B. Scheid, S. Dorbolo, L. R. Arriaga, and E. Rio, Phys. Rev. Lett. **109** 264502 (2012).
16) Y. Vitry, S. Dorbolo, J. Vermant, and B. Scheid, Adv. Colloid Interface Sci. **270** 73 (2019).
17) A. T. Poortinga, Langmuir **27** 2138 (2011).
18) A. T. Poortinga, Colloid. Surf. A: Physicochem. Eng. Aspects **419** 15 (2013).
19) J. E. Silpe, J. K. Nunes, A. T. Poortinga, and H. A. Stone, Langmuir **29** 8782 (2013).
20) M. Postema, N. de Jong, G. Schmitz, and A. van Wamel, Proc. 2005 IEEE Ultrason. Symp. 977 (2005).
21) N. Kudo, R. Uzbekov, R. Matsumoto, R. Shimizu, C. Carlson, N. Anderton,

A. Deroubaix, C. Penny, A. T. Poortinga, D. M. Rubin, A. Bouakaz, and M. Postema, Proc. 40th Symp. UltraSon. Electron. 2E3-1 (2019).

22) M. Postema, A. Novell, C. Sennoga, A. T. Poortinga, and A. Bouakaz, Appl. Acoust. **137** 148 (2018).

23) K. Johansen and M. Postema, Hydroacoustics **19** 197 (2016).

24) K. Johansen, S. Kotopoulis, A. T. Poortinga, and M. Postema, Physics Procedia **70** 1079 (2015).

25) S. Kotopoulis, K. Johansen, O. H. Gilja, A. T. Poortinga, and M. Postema, Acta Phys. Polon. A **127** 99 (2015).

26) N. Kudo, IEEE Trans. Ultrason. Ferroelect. Freq. Control **64** 273 (2017).

27) S. Imai and N. Kudo, IEEE Int. Ultrason. Symp. **IUS2018** 184 (2018).

28) M. Postema, A. Bouakaz, C. T. Chin, and N. de Jong, IEEE Trans. Ultrason. Ferroelect. Freq. Control **50** 523 (2003).

PUBLICATION III

Determining the influence of endoskeleton friction on the damping of pulsating antibubbles

N. Anderton, C. S. Carlson, V. Aharonson, and M. Postema

Current Directions in Biomedical Engineering, vol. 8, no. 2, pp. 781–784
DOI: 10.1515/cdbme-2022-1199

Nicole Anderton*, Craig S. Carlson, Vered Aharonson, and Michiel Postema

Determining the influence of endoskeleton friction on the damping of pulsating antibubbles

https://doi.org/10.1515/cdbme-2022-1199

Abstract: Recent *in-vivo* work showed the suitability of Pickering-stabilized antibubbles in harmonic imaging and ultrasound-guided drug delivery. To date, however, theoretical considerations of antibubble core properties and their effects on antibubble dynamics have been rather sparse. The purpose of this study was to investigate the influence of skeletal friction on the damping of a pulsating antibubble and the pulsation phase of an antibubble relative to the incident sound wave. Numerical simulations were performed to compute damping terms and pulsation phases of micron-sized antibubbles with thin elastic shells and 30% endoskeleton volume fraction. The simulations showed that the damping owing to skeleton presence dominates the damping mechanism for antibubbles of radii less than 2.5 μm, whilst it is negligible for greater radii. The pulsation phase of such small antibubbles was simulated to have a phase delay of up to $\frac{1}{6}\pi$ with respect to pulsating free gas bubbles. Our findings demonstrate that the presence of an endoskeleton inside a bubble influences pulsation phase and damping of small antibubbles. Antibubbles of radii less than 3 μm are of interest for the use as ultrasound contrast agents.

Keywords: Acoustic driving, ultrasound contrast agent, endoskeleton, antibubble damping modelling, harmonic oscillation.

1 Introduction

Endoskeletal antibubbles comprise gas bubbles with one or more liquid cores. These cores are suspended by a solid skeletal structure consisting of hydrophobic particles [1], as shown in Figure 1.

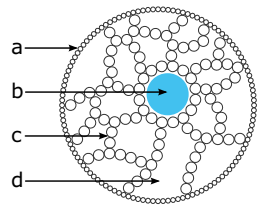

Fig. 1: Microscopic photograph of an endoskeletal antibubble and a schematic representation thereof: (a) shell; (b) liquid core; (c) skeleton; (d) gas.

As free, unencapsulated, antibubbles, are short-lived [2–5], antibubbles are typically stabilized by adsorbing nanoparticles to the liquid–gas interfaces. This process has been referred to as Pickering-stabilizing [6].

When subjected to ultrasound, the presence of an incompressible core allows for asymmetric pulsation excursions, even at modest acoustic driving amplitudes [7]. Consequently, antibubbles have been proposed as ultrasound contrast agents for low-mechanical-index harmonic imaging [8, 9]. If the liquid cores are loaded with therapeutics, antibubbles act as vehicles for ultrasound-guided drug delivery, as shown recently *in vivo* [10].

For diagnostic as well as therapeutic applications, it is highly relevant to predict antibubble dynamics and to quantify the influence of the presence of liquid and solid cores on these dynamics. In this study, we investigated the influence of skeletal friction on the pulsation phase of an antibubble relative to the incident sound wave. The purpose of this investigation was to quantify the core presence from pulsation phase observations.

Pulsation phases of damped oscillators have been analyzed thoroughly for forced mass–spring–dashpot systems [11]. They had been simulated for pulsating ultrasound contrast agent microbubbles with various shell thicknesses [12, 13]. Pulsation phases of antibubbles have not been previously reported on.

Radial pulsations of shell-encapsulated microbubbles have been modeled using adaptations of the Rayleigh-Plesset equation. These have been modified to account for specific

***Corresponding author: Nicole Anderton,** BioMediTech, Faculty of Medicine and Health Technology, Tampere University, Korkeakoulunkatu 3, 33720 Tampere, Finland, e-mail: nicole.anderton@tuni.fi

Craig S. Carlson, Michiel Postema, BioMediTech, Faculty of Medicine and Health Technology, Tampere University, Tampere, Finland and School of Electrical and Information Engineering, University of the Witwatersrand, Johannesburg, Braamfontein, South Africa

Vered Aharonson, School of Electrical and Information Engineering, University of the Witwatersrand, Johannesburg, Braamfontein, South Africa and School of Sciences, University of Central Lancashire — Cyprus, Pyla, Cyprus and Afeka Tel Aviv Academic College of Engineering, Tel Aviv, Israel

properties of the surrounding medium, for high-amplitude acoustic driving [14], for changes in surface tension owing to buckling [15], for the presence of a solid elastic shell [16], a thin lipid shell [17], a viscous or viscoelastic shell [18, 19], for the presence of another oscillator nearby [20], and for tethering [21], just to name a few. Several review articles have been dedicated to comparing the many models [22–24]. In principle, the most basic Rayleigh-Plesset equation suffices for a precise estimation of the radial dynamics of a shell-encapsulated microbubble, provided that the pulsation velocity does not approach the speed of sound, the pulsation excursion amplitude is much less than the resting size, and only few pulsation cycles are taken into account, so that viscous or viscoelastic effects remain negligible. In this study, we were assuming low-amplitude very short-pulsed ultrasound, which justifies our choice for a rather simplistic model.

In previous simulation studies, the combined solid and liquid internal structure had been represented by an incompressible volume $V_c = \varphi V_0$, where $\varphi \in [0,1\rangle$ is the constant volume fraction and V_0 is the volume of the antibubble [7]. Empirical evidence to justify a constant size-independent volume fraction exists in the form of scanning electron microscopy and confocal microscopy images [1].

2 Theory

Let us consider an antibubble of resting radius R_0 with an infinitesimal shell and surrounded by an infinite liquid of density ρ. If the antibubble is forced by a short short pressure pulse $p(\omega t)$ of angular center frequency ω, whose amplitude is so small that that the pulsation amplitude of the antibubble is less than R_0, we may regard this system as a forced damped oscillator with an effective mass $m = 4\pi\rho(R_0+x)^3$ [25], instantaneous excursion x, damping coefficient δ [25, 26], and angular resonance frequency ω_r.

If the amplitude of the driving function function is instantly lessened [27], the damping coefficient of the pulsating entity undergoing damping can then be determined by measuring two consecutive decaying excursion amplitudes x_i and x_{i+1} (*cf.* Figure 2) and substituting them into [11]:

$$\delta = \frac{2\ln\frac{x_i}{x_{i+1}}}{(2\pi)^2 + \left(\ln\frac{x_i}{x_{i+1}}\right)^2} . \tag{1}$$

We propose that, for an endoskeletal antibubble, the damping coefficient consists of five components, four of which are identical to those of shell-encapsulated microbubbles:

$$\delta = \delta_v + \delta_r + \delta_{\textcircled{\scriptsize o}} + \delta_{\textcircled{\scriptsize x}} + \delta_\theta , \tag{2}$$

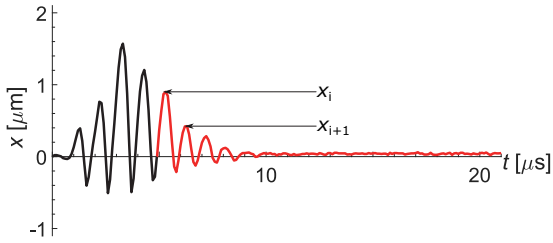

Fig. 2: Antibubble excursion as a function of time, for an antibubble of resting radius $R_0 = 5\,\mu$m, forced by a short pulse. The unforced pulsation part is represented by a red line.

where

$$\delta_v = \frac{4\eta}{\omega\rho\,(R_0+x)^2} \tag{3}$$

is the viscous damping [26], in which η is the dynamic viscosity of the surrounding medium,

$$\delta_r = \frac{\omega\,(R_0+x)}{c} \tag{4}$$

is the damping owing to reradiation [26], in which c is the speed of sound of the surrounding medium,

$$\delta_{\textcircled{\scriptsize o}} = \frac{S_{\textcircled{\scriptsize o}}}{m\,\omega} \tag{5}$$

is the damping owing to friction in the shell, in which $S_{\textcircled{\scriptsize o}}$ is the outer shell friction parameter [28],

$$\delta_{\textcircled{\scriptsize x}} = \varphi^n \frac{S_{\textcircled{\scriptsize x}}}{m\,\omega} \tag{6}$$

is the damping owing to friction in the endoskeleton, in which n is a noninteger power and $S_{\textcircled{\scriptsize x}}$ is a thus-far undefined skeleton friction parameter, and

$$\delta_\theta = \frac{\frac{\sinh X+\sin X}{\cosh X-\cos X} - \frac{2}{X}}{\frac{X}{3(\gamma-1)} + \frac{\sinh X+\sin X}{\cosh X-\cos X}} \left(\frac{\omega_r}{\omega}\right)^2 \tag{7}$$

is the thermal damping, in which $X = \frac{R_0}{l_D}\left(1-\varphi^{\frac{1}{3}}\right) > 1$. The thermal boundary layer thickness is given by Eller [29]:

$$l_D = \sqrt{\frac{K_g}{2\,\omega\,\rho_g C_p}} , \tag{8}$$

where C_p is the specific heat of the gas, K_g is the thermal conductivity of the gas, ρ_g is the density of the gas.

An expression for the linear angular resonance frequency of a shell-encapsulated antibubble has been stated by Kudo [1]. A derivation of the difference in pulsation phase of any base-forced damped oscillator was shown by Attenborough and Postema [11]. A solution for a single bubble structure was presented by Postema and Schmitz [13]:

$$\alpha = \pi + \arctan\left(\frac{\left(\frac{\omega}{\omega_r}\right)\delta}{1-\left(\frac{\omega}{\omega_r}\right)^2}\right) , \tag{9}$$

where α is the phase difference between the antibubble pulsation and the incident sound field.

3 Methods

Numerical solutions of (2)–(9) were computed using MATLAB®. The input parameters were chose such that they simulated experimental situations in antibubble literature: $c = 1480\,\mathrm{m\,s^{-1}}$, $C_\mathrm{p} = 1000\,\mathrm{J\,kg^{-1}\,K^{-1}}$, $K_\mathrm{g} = 0.025\,\mathrm{W\,m^{-1}\,K^{-1}}$, $\eta = 1.00\,\mathrm{mPa}$, $\rho = 998\,\mathrm{kg\,m^{-3}}$, $\rho_\mathrm{g} = 1.00\,\mathrm{kg\,m^{-3}}$, $\sigma = 0.072\,\mathrm{N\,m^{-1}}$, $\omega = 2\pi \times 1.0 \times 10^6\,\mathrm{s^{-1}}$. The outer shell was considered of negligible stiffness $\leq 0.2\,\mathrm{N\,m^{-1}}$.

During our simulations, the expression $\left(S_{\bigcirc} + \varphi^n S_{\otimes}\right)$ was treated as a single variable.

The resting radius was varied from $0.5\,\mu$m to $12\,\mu$m.

4 Results and discussion

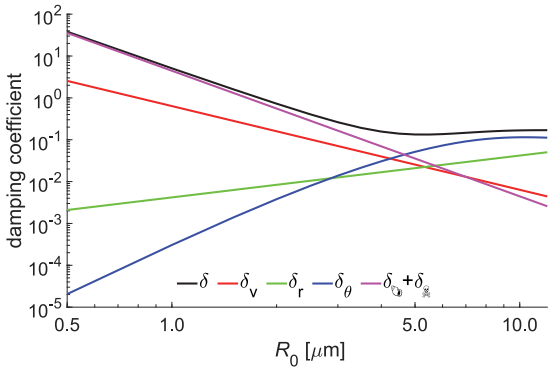

Fig. 3: Dimensionless damping coefficient and its contributing components as a function of antibubble resting radius.

Figure 3 shows the damping coefficient and its contributing components for an antibubble with an endoskeleton of 30% volume fraction. The shell friction and skeleton friction parameters had been chosen conservatively, with equal values of $0.27\,\mu\mathrm{N\,s\,m^{-1}}$, similar to some lipids. For greater values, the damping was observed to be dominated by thermal damping and reradiation. For antibubbles of resting radii less than $2.5\,\mu$m, however, the damping owing to shell and endoskeleton presence was even greater than the viscous damping term. The trade-off size coincided with the resonant size at the driving frequency of 1 MHz. It is noted that antibubbles with greater volume fraction have an even stronger skeleton friction damping term (not shown). As ultrasound contrast agent particles need to have diameters less than those of capillaries, the findings of the smaller antibubbles are most relevant to medical imaging.

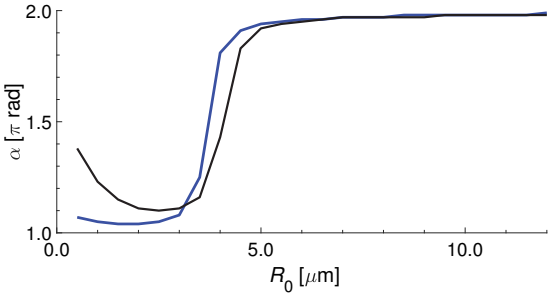

Fig. 4: Pulsation phase with respect to the incident sound field, as a function of resting radius, for an antibubble (black) and a free gas bubble (blue).

Figure 4 shows the pulsation phase of an antibubble and a free gas bubble, with respect to an incident pulse of 1-MHz central driving frequency. At the parameters chosen, only the smaller antibubbles were found to have a substantially different pulsation phase compared tot the free gas bubbles. A phase difference of up to $\frac{1}{6}\pi$ was computed. The finding is useful in optically or acoustically determining whether a bubble is a core-comprising antibubble or an empty gas bubble.

5 Conclusions

Pulsation phases of micron-sized antibubbles differed from those of free gas bubbles. These differences may be attributed to the friction of the antibubble shells and skeletons.

For smaller antibubbles, shell and skeleton friction were found to be the dominant damping mechanisms of pulsating antibubbles driven at frequencies less than their resonance frequencies.

Author statement

Research funding: This work was supported by the National Research Foundation of South Africa, Grant Numbers 97742 and 127102, and by the Academy of Finland, Grant Number 340026. Conflict of interest: Authors state no conflict of interest. Informed consent: Authors state that informed consent is not applicable. Ethical approval: Authors state that no ethical approval was required for this research as no human or animal samples or data were used.

References

[1] Kudo N, Uzbekov R, Matsumoto R, Shimizu R, Carlson CS, Anderton N, et al. Asymmetric oscillations of endoskeletal antibubbles. Jpn J Appl Phys 2020;59:SKKE02.

[2] Dorbolo S, Caps H, Vandewalle N. Fluid instabilities in the birth and death of antibubbles. New J Phys 2003;5:161.

[3] Postema M, ten Cate FJ, Schmitz G, de Jong N, van Wamel A. Generation of a droplet inside a microbubble with the aid of an ultrasound contrast agent: first result. Lett Drug Des Discov 2007;4:74–77.

[4] Vitry Y, Dorbolo S, Vermant J, Scheid B. Controlling the lifetime of antibubbles. Adv Colloid Interfac Sci 2019;270:73–86.

[5] Zou J, Ji C, Yuan BG, Ruan XD, Fu X. Collapse of an antibubble. Phys Rev E 2013;87:061002.

[6] Poortinga AT. Long-lived antibubbles: stable antibubbles through Pickering stabilization. Langmuir 2011;27:2138–2141.

[7] Kotopoulis S, Johansen K, Gilja OH, Poortinga AT, Postema M. Acoustically active antibubbles. Acta Phys Pol A 2015;127:99–102.

[8] Postema M, Novell A, Sennoga C, Poortinga AT, Bouakaz A. Harmonic response from microscopic antibubbles. Appl Acoust 2018;137:148–150.

[9] Panfilova A, Chen P, van Sloun RJG, Wijkstra H, Postema M, Poortinga AT, et al. Experimental acoustic characterization of an endoskeletal antibubble contrast agent: first results. Med Phys 2021;48:6765–6780.

[10] Kotopoulis S, Lam C, Haugse R, Snipstad S, Murvold E, Jouleh T, et al. Formulation and characterisation of drug-loaded antibubbles for image-guided and ultrasound-triggered drug delivery. Ultrason Sonochem 2022;105986.

[11] Attenborough K, Postema M. A pocket-sized introduction to dynamics. Kingston upon Hull: University of Hull 2008.

[12] Postema M, de Jong N, Schmitz G. The physics of nanoshelled microbubbles. Biomed Tech 2005;50(S1):748–749.

[13] Postema M, Schmitz G. Ultrasonic bubbles in medicine: influence of the shell. Ultrason Sonochem 2007;14:438–444.

[14] Frinking P, de Jong N, Cespedes I. Scattering properties of encapsulated gas bubbles at high ultrasound pressures. J Acoust Soc Am 1999;105:1989–1996.

[15] Marmottant P, van der Meer S, Emmer M, Versluis M, de Jong N, Hilgenfeldt S, et al. A model for large amplitude oscillations of coated bubbles accounting for buckling and rupture. J Acoust Soc Am 2005;118:3499–3505.

[16] Church CC. The effects of an elastic solid surface layer on the radial pulsations of gas bubbles. J Acoust Soc Am 1995;97:1510–1521.

[17] Doinikov AA, Dayton PA. Maxwell rheological model for lipid-shelled ultrasound microbubble contrast agents. J Acoust Soc Am 2007;121:3331–3340.

[18] Sarkar K, Shi WT, Chatterjee D, Forsberg F. Characterization of ultrasound contrast microbubbles using in vitro experiments and viscous and viscoelastic interface models for encapsulation. J Acoust Soc Am 2005;118:539–550.

[19] Tsiglifis K, Pelekasis NA. Nonlinear radial oscillations of encapsulated microbubbles subject to ultrasound: the effect of membrane constitutive law. J Acoust Soc Am 2008;123:4059–4070.

[20] Doinikov AA. Equations of coupled radial and translational motions of a bubble in a weakly compressible liquid. Phys Fluids 2005;17:128101.

[21] Maksimov A, Leighton T, Birkin P. Dynamics of a tethered bubble. AIP Conf Proc 2006;838:512.

[22] Vokurka K. Comparison of Rayleigh's, Herring's, and Gilmore's models of gas bubbles. Acustica 1986;59:214–219.

[23] Doinikov AA, Bouakaz A. Review of shell models for contrast agent microbubbles. IEEE Trans Ultrason Ferroelectr Freq Control 2011;58:981–993.

[24] Versluis M, Stride E, Lajoinie G, Dollet B, Segers T. Ultrasound contrast agent modeling: a review. Ultrasound Med Biol 2020;46:2117–2144.

[25] Medwin H. Counting bubbles acoustically: a review. Ultrasonics 1977;15:7–13.

[26] Devin C. Survey of thermal, radiation, and viscous damping of pulsating air bubbles in water. J Acoust Soc Am 1959;31:1654–1667.

[27] Leighton TG, White PR, Morfey CL, Clarke JWL, Heald GJ, Dumbrell HA, Holland KR. The effect of reverberation on the damping of bubbles. J Acoust Soc Am, 2002;112:1366–1376.

[28] de Jong N, Cornet R, Lancée CT. Higher harmonics of vibrating gas-filled microspheres. Part one: simulations. Ultrasonics 1993;32:447–453.

[29] Eller AI. Damping constants of pulsating bubbles. J Acoust Soc Am 1970;47:1469–1470.

PUBLICATION IV

On the rigidity of four hundred Pickering-stabilised microbubbles

N. Anderton, C. S. Carlson, R. Matsumoto, R.-i. Shimizu, A. T. Poortinga, N. Kudo, and M. Postema

Japanese Journal of Applied Physics, vol. 61, no. SG, SG8001
DOI: 10.35848/1347-4065/ac4adc

Japanese Journal of Applied Physics

The Japan Society of Applied Physics

ACCEPTED MANUSCRIPT

On the rigidity of four hundred Pickering-stabilised microbubbles

To cite this article before publication: Nicole Anderton *et al* 2022 *Jpn. J. Appl. Phys.* in press https://doi.org/10.35848/1347-4065/ac4adc

Japanese Journal of Applied Physics **BRIEF NOTE**

On the rigidity of four hundred Pickering-stabilised microbubbles

Nicole Anderton[1]*, Craig S. Carlson[1,2], Ryunosuke Matsumoto[3], Ri-ichiro Shimizu[3], Albert T. Poortinga[4], Nobuki Kudo[3], and Michiel Postema[1,2]

[1]*BioMediTech, Faculty of Medicine and Health Technology, Tampere University, Korkeakoulunkatu 3, 33720 Tampere, Finland*

[2]*School of Electrical and Information Engineering, University of the Witwatersrand, Johannesburg, 1 Jan Smuts Laan, 2001 Braamfontein, South Africa*

[3]*Faculty of Information Science and Technology, Hokkaido University, Kita 14 Jo, Nishi 9 Chome, Kita-ku, Sapporo, Hokkaido 060-0814, Japan*

[4]*Department of Mechanical Engineering, Eindhoven University of Technology, De Zaale, 5600 MB Eindhoven, Netherlands*

This study explores the rigidity of Pickering-stabilised microbubbles subjected to low-amplitude ultrasound. Such microbubbles might be suitable ultrasound contrast agents. Using an adapted Rayleigh-Plesset equation, we modelled the dynamics of microbubbles with a 7.6-N m^{-1} shell stiffness under 1-MHz, 0.2-MPa sonication. Such dynamics were observed experimentally, too, using high-speed photography. The maximum expansions were agreeing with those predicted for Pickering-stabilised microbubbles. Subjecting microbubbles to multiple time-delayed pulses yielded the same result. We conclude that Pickering-stabilised microbubbles remain very stable at low acoustic amplitudes.

Pickering-stabilised bubbles have been of interest as novel ultrasound contrast agents.[1)] This study explores the rigidity of such a Pickering-stabilised ultrasound contrast agent subjected to ultrasound with a low amplitude.

Ultrasound contrast agents comprise microscopic gas bubbles typically stabilised by elastic or viscoelastic shells.[2,3)] These so-called microbubbles oscillate upon sonication.[4,5)] Administered to the blood pool by injection, ultrasound contrast agents were originally intended for diagnostic purposes through harmonic ultrasonic imaging.[6–9)] In addition to diagnostics, these agents have become of therapeutic interest, owing to the discovery of sonoporation.[10–12)] Sonoporation or sonopermeation refers to the transient permeation of cell membranes by means of ultrasound with amplitudes below the cavitation threshold, allowing for the transmembrane delivery of drugs and genes.[13)] The occurrence of sonoporation is drastically amplified by the presence of an ultrasound contrast agent.[14,15)] Even if drugs are administered separately from

*E-mail: nicole.anderton@tuni.fi

an ultrasound contrast agent, whilst a region of treatment is being sonicated, the local drug uptake in the sonicated region might increase. Such sonoporation-assisted drug delivery has been successful in the treatment of human pancreatic cancer.[16)]

It has been proposed by many groups to incorporate therapeutics directly onto or into microbubbles as to create vehicles for ultrasound-assisted drug delivery, as explained in reviews on this topic.[17,18)] Despite several attempts to manufacture such futuristic agents, however, it has not been fully understood under which acoustic conditions the carrier microbubbles are disrupted to release their payload, and what the influence of the microbubble shell is on the disruption process.

Ultrasound contrast agent microbubble disruption has been studied with high-speed photography.[19,20)] The two main mechanisms observed with ultrasound contrast agent microbubble disruption are referred to as sonic cracking and fragmentation.[20)] Sonic cracking occurs during expansion of an oscillating bubble, releasing the gaseous bubble contents through one or more pores or cracks in the shell. It has been exclusively observed with ultrasound contrast agent microbubbles with inflexible shells of thickness greater than 100 nm. Fragmentation occurs when the bubble is contracting. Fragmentation can result from a surplus of kinetic energy over surface energy during contraction or from asymmetric collapse, also known as jetting. It has been exclusively observed with ultrasound contrast agent microbubbles with surfactant shells of a few nanometers thickness. Both sonic cracking and fragmentation results in the formation of free gas bubbles.[20)] Such free gas microbubbles dissolve within milliseconds.[3)]

Instead of being surrounded by a physical shell, a microbubble may have been stabilised by adsorbing colloidal particles at the gas–liquid interface. This process is called Pickering stabilising.[21)] Pickering-stabilised microbubbles are rigid at ambient hydrostatic pressures.[22)] Despite this rigidity, shrinking of Pickering-stabilised microbubbles has been occasionally observed during single-pulse sonication.[1)] Microbubble gas dissolution could be ruled out here, as this is very slow relative to the oscillation times.[3)] A hypothetical explanation might be that the stabilised shell rearranged itself during sonication to take up less surface area.

Having also observed disruption of a Pickering-stabilised antibubble at a high acoustic amplitude,[23)] we hypothesised that ultrasound might influence the shell rigidity. The present study focussed on the rigidity of Pickering-stabilised microbubbles at a low acoustic amplitude. We theoretically modelled and experimentally observed the dynamics of Pickering-stabilised microbubbles with special attention to radial excursions during the first oscillation cycle.

The radial oscillatory motion of bubbles is typically described by a type of Rayleigh-Plesset equation. Over the past 100 years, Rayleigh-Plesset equations have been modified to

incorporate terms to account for the viscosity of the surrounding liquid, dynamic thermal conditions, and the presence of an encapsulating shell, just to name a few.[24–27] As we concentrate on disruption in the paper, we are less interested in the accuracy of the model beyond the first two cycles. Therefore, we may use a rather simple model, whose derivation we presented earlier,[28] whilst ignoring any solid potentially present inside the microbubble and by adding damping terms and a shell stiffness parameter.[25,29]

For an encapsulated microbubble driven by an acoustic wave, the fundamental equation is then given by

$$\begin{aligned} R\ddot{R} + \tfrac{3}{2}\dot{R}^2 = \frac{1}{\rho}\Bigg[&\left(p_0 - p_\mathrm{v} + \frac{2\sigma}{R_0}\right)\left(\frac{R_0}{R}\right)^{3\gamma} \\ &+ p_\mathrm{v} - \frac{2\sigma}{R} - 2\chi\left(\frac{1}{R_0} - \frac{1}{R}\right) \\ &- \frac{4\eta\dot{R}}{R} - \delta\omega\rho R\dot{R} - p_0 - p(t)\Bigg] \quad , \end{aligned} \tag{1}$$

where $p(t)$ is the time-dependent acoustic driving function, p_0 is the ambient pressure, p_v is the vapour pressure, R is the instantaneous radius, R_0 is the initial radius, γ is the ratio of specific heats, δ is the damping coefficient, η is the liquid viscosity, ρ is the liquid density, σ is the surface tension, χ is the shell stiffness, and ω is the angular driving frequency.

As the viscous damping has been directly included in (1), δ only comprises the damping owing to reradiation and the thermal damping, yielding $\delta \approx kR + \frac{3}{5}(\gamma - 1)$, where $k = \frac{\omega}{c}$ is the wave number, in which c is the speed of sound.

During expansion, a Pickering-stabilised interface is regarded frictionless and of constant surface tension. The latter assumption has been confirmed experimentally.[30] As fragmentation typically occurs during the onset of collapse, we may ignore any effects typical for contraction, provided that simulations after the first collapse phase are disregarded.

On the time interval $[-10\,\mu\mathrm{s}, 10\mu\mathrm{s}]$, a driving function was defined by

$$p(t) = \begin{cases} A\sin\omega t & \forall \quad t \in [0\,\mu\mathrm{s}, 3\,\mu\mathrm{s}] \\ 0 & \forall \quad t \notin [0\,\mu\mathrm{s}, 3\,\mu\mathrm{s}] \end{cases} \quad , \tag{2}$$

where the acoustic amplitude $A = 1.0\,\mathrm{MPa}$ and $\omega = 2\pi \times 10^6\,\mathrm{rad\,s^{-1}}$. This driving function corresponded to a three-cycle pulse of 1-MHz centre frequency.

Numerical solutions of (1) were computed using the `ode45` differential equation solver of MATLAB® (The MathWorks, Inc., Natick, MA, USA), assuming the following parameters constant: $k = 4.23\times10^3\,\mathrm{m^{-1}}$, $p_0 = 101\,\mathrm{kPa}$, $p_\mathrm{v} = 2.33\,\mathrm{kPa}$, $\gamma = 1.4$, $\eta = 1.00\,\mathrm{mPa\,s}$, $\rho = 998\,\mathrm{kg\,m^{-3}}$, and $\sigma = 0.072\,\mathrm{N\,m^{-1}}$. For free or released gas microbubbles χ must be zero.

The $R(t)$ curves computed were automatically cut off after the first oscillation cycle, after which the maximum expansion radius $R_{\max}$ was determined. The combined outcome of the simulations were two curves $R_{\max}(R_0)$, one for Pickering-stabilised microbubbles, the other for free gas microbubbles. These were to be compared with experimental footage of microbubble expansion. A small subset of these data has been presented as controls in a different study.[31)]

The Pickering-stabilised air-comprising microbubbles studied had been produced as previously published,[32)] without core material present. For Pickering-stabilisation, Aerosil® R 972 hydrophobised silica particles (Evonik Industries AG, Essen, Germany) had been added, with diameters less than 30 nm. Microbubble populations stabilised with these hydrophobised silica particles had been studied as controls at low acoustic amplitudes.[33)] These populations had been measured to have a mean radius of 3 μm. Panfilova et al. estimated the bulk resonance frequency near 1 MHz.[33)]

A quantity of 5 mg of freeze-dried material was deposited into a FALCON® 15 mL High-Clarity Polypropylene Conical Tube (Corning Science México S.A. de C.V., Reynosa, Tamaulipas, Mexico), after which 5.0 mL of 049-16787 Distilled Water (FUJIFILM Wako Pure Chemical Corporation, Chuo-Ku, Osaka, Japan) was added. The emulsion was shaken gently by hand for 1 minute. For each experiment, 0.2 mL was pipetted into the observation chamber of a high-speed observation system.[34)]

The experimental procedure for collecting high-speed video footage of Pickering-stabilised microbubbles under high-amplitude sonication was almost identical to the procedure used to collect footage from antibubbles.[31)] The observation chamber was placed under an Eclipse Ti inverted microscope (Nikon Corporation, Minato-ku, Tokyo, Japan) with a Plan Apo LWD 40×WI (N.A. 0.8) objective lens. Attached to the microscope was an HPV-X2 high-speed camera (Shimadzu, Nakagyo-ku, Kyoto, Japan), operating at frame rates equal to ten million frames per second.[35)] The exposure time corresponded to 0.10 μs per frame. Each frame corresponded to a 145×91-μm^2 area.

During each video recording, the observation chamber was subjected to one ultrasound pulse from a laboratory-assembled focussed single-element transducer.[34,35)] Each pulse had a centre frequency of 1.0 MHz. The voltage amplitude of the pulse was 1 V. In a running wave field, this voltage corresponded to a peak-negative acoustic pressures of 0.20 MPa. The transmitted pulse started with the compression phase. The signal fed into the transducer was generated by an AFG320 arbitrary function generator (Sony-Tektronix, Shinagawa-ku, Tokyo, Japan) and amplified by a UOD-WB-1000 wide-band power amplifier (TOKIN Corporation, Shiroishi, Miyagi, Japan).

A total number of 400 microbubbles subjected to 1-V pulses was analysed. Only events were selected in which the distances between microbubbles were much greater than the maximum excursions. Each video sequence consisted of 256 frames. The video sequences were stored on a personal computer and processed offline using a method previously published.[28] The first oscillation cycle was taken into account to determine $R_{\max}$. The outcome of the processing were $R(t)$ curves for all 400 microbubbles, and their respective $R_{\max}$ values.

The experiments done served to determine the shell stiffness of the Pickering-stabilised bubbles. The estimated value for χ was obtained as follows. Excursion amplitudes were taken from bubbles sonicated at a 1-V pulse amplitude. A least-squares fit through the measured excursion amplitudes yielded $R_{\max} = 1.082R_0$. Iterating through (1) using 0.1-N m^{-1} increments for $\chi \in [1.0, 20.0]$ N m^{-1}, $R_{\max}(R_0)$ curves were created through which $y = ax$ least-squares fits were computed. The fit with a closest to 1.082 corresponded to $\chi = 7.6$ N m^{-1}. Hence, the stiffness determined for the Pickering-stabilised shell is approximately equal to that of a rigid albumin-shelled ultrasound contrast agent.[36]

We performed a stability analysis by subjecting six individual bubbles to three consecutive 1-minute delayed pulses. The respective bubble dynamics were observed to be the same for each pulse, as illustrated by the event shown in Figure 1. It was observed that microbubbles Pickering-stabilised with hydrophobised silica were not disrupted at these low acoustic amplitudes.

The Pickering-stabilised microbubbles were observed to contract and expand subsequently. As an example, Figure 2 shows the radial dynamics during the first oscillation cycle of a Pickering-stabilised microbubble of 4.6-μm initial radius, measured from high-speed videos. In addition, $R(t)$ curves simulated for an encapsulated microbubble and for a free microbubble have been included. The measured data correspond to the first cycle of the simulated $R(t)$ curve of a microbubble with shell stiffness $\chi = 7.6$ N m^{-1} and clearly do not correspond to the much greater expansion of a free microbubble.

The Pickering-stabilised microbubble whose dynamics are shown in Figure 2 did not appear to have undergone gas release. From this observation, we deduct, that stabilising particles must have been present on the interface during expansion. As the experimental data matched the $R(t)$ curves, we conclude that the disruption did not take place during these first oscillation cycles.

By definition, the initial internal pressure, $p_0 - p_v + \frac{2\sigma}{R_0}$, cannot be lower than the hydrostatic pressure. Hence, the assumption that sonic cracking should have resulted in gas escape observations was justified.

Figure 3 shows an overview of $R_{\max}$ as a function of R_0. More than 90% of the microbubble excursions fitted the simulated $R_{\max}(R_0)$ curve at $\chi = 7.6\,\mathrm{N\,m^{-1}}$. Consequently, the shell stiffness computed is a good representation for the stiffness of the Pickering-stabilised shell.

Follow-up studies will need to answer, whether ultrasound-assisted Pickering-stabilised shell disruption can be predicted at high acoustic amplitudes.

Following equations (8)–(10) by Doinikov et al.,[26] it was found that at 1-MHz sonication the resonant radius of Pickering-stabilised bubbles must be 9.6 μm, for $\chi = 7.6\,\mathrm{N\,m^{-1}}$. Microbubbles of initial radii greater than 5.0 μm were excluded from this study, as they are not of clinical relevance.

In summary, the maximum radial expansions observed were agreeing with the maxima predicted by the model of Pickering-stabilised microbubbles. These observations support the previous assumption that the rigidity of Pickering-stabilised shells is high. Gas release from these disrupted microbubbles was not observed, indicating that the particle structuring remained on the interface during radial oscillation. Subjecting microbubbles to multiple time-delayed pulses yielded the same result. We conclude that Pickering-stabilised microbubbles remain very rigid at low acoustic amplitudes.

Acknowledgements

This work was supported by JSPS KAKENHI, Grant Numbers JP17H00864 and JP20H04542, by the National Research Foundation of South Africa, Grant Number 127102, and by the Academy of Finland, Grant Number 340026.

References

1) N. Anderton, C. S. Carlson, R. Matsumoto, R. Shimizu, A. T. Poortinga, N. Kudo, and M. Postema, Proc. 42nd UltraSonic Electronics Symp., 2021, 2E4-4.
2) M. Chan and K. Soetanto, Jpn. J. Appl. Phys. **37**, 3078 (1998).
3) K. Yoshida, M. Ebata, C. Kaneko, Y. Zhang, Y. Shibata, K. Saito, T. Toyota, H. Hayashi, and T. Yamaguchi, Jpn. J. Appl. Phys. **60**, SDDE10 (2021).
4) Y. Yamakoshi and M. Koganezawa, Jpn. J. Appl. Phys. **44**, 4583 (2005).
5) K. Kawabata, R. Asami, T. Azuma, and S. Umemura, Jpn. J. Appl. Phys. **49**, 9 (2010).
6) S. Tano, N. Ueno, T. Tomiyama, and K. Kimura, Clin. Radiol. **52**, 41 (1997).
7) K. Kawabata, N. Sugita, H. Yoshikawa, T. Azuma, and S. Umemura, Jpn. J. Appl. Phys. **44**, 4548 (2005).
8) H. Yoshikawa, T. Azuma, K. Sasaki, K. Kawabata, and S. Umemura, Jpn. J. Appl. Phys. **45**, 4754 (2006).
9) M. Tanabe, K. Okubo, N. Tagawa, and T. Moriya, Jpn. J. Appl. Phys. **47**, 4149 (2008).
10) K. Tachibana and S. Tachibana, Jpn. J. Appl. Phys. **38**, 3014 (1999).
11) L. B. Feril Jr., T. Kondo, Y. Tabuchi, R. Ogawa, Q.-L. Zhao, T. Nozaki, T. Yoshida, N. Kudo, and K. Tachibana, Jpn. J. Appl. Phys. **46**, 4435 (2007).
12) Y. Yamakoshi, T. Miwa, N. Yoshizawa, H. Inoguchi, and D. Zhang, Jpn. J. Appl. Phys. **49**, 07HF17 (2010).
13) S. M. Nejad, H. Hosseini, H. Akiyama, and K. Tachibana, Theranostics **6**, 446 (2016).
14) K. Okada, N. Kudo, K. Niwa, and K. Yamamoto, J. Med. Ultrasonics **32**, 3 (2005).
15) N. Kudo, K. Okada, and K. Yamamoto, Biophys. J. **96**, 4866 (2009).
16) G. Dimcevski, S. Kotopoulis, T. Bjånes, D. Hoem, J. Schjøtt, B. T. Gjertsen, M. Biermann, A. Molven, H. Sorbye, E. Mc Cormack, M. Postema, and O. H. Gilja, J. Control. Release **243**, 172 (2016).
17) M. Postema and O. H. Gilja, Curr. Pharm. Biotechnol. **8**, 355 (2007).
18) J. Rich, Z. Tian, and T. J. Huang, Adv. Mater. Technol. 2100885 (2021).
19) N. Kudo, T. Miyaoka, K. Kuribayashi, and K. Yamamoto, J. Acoust. Soc. Am. **108**, 2547 (2000).
20) M. Postema, A. van Wamel, C. T. Lancée, and N. de Jong, Ultrasound Med. Biol. **30**, 827 (2004).
21) A. T. Poortinga, Langmuir **27**, 2138 (2011).
22) Z. Du, M. P. Bilbao-Montoya, B. P. Binks, E. Dickinson, R. Ettelaie, and B. S. Murray,

Langmuir **19**, 3106 (2003).

23) N. Anderton, C. S. Carlson, N. Kudo, A. T. Poortinga, and M. Postema, Jpn. J. Appl. Phys. **60**, 128001 (2021).
24) I. C. Macedo and W.-J. Yang, Jpn. J. Appl. Phys. **11**, 1124 (1972).
25) N. de Jong, R. Cornet, and C. T. Lancée, Ultrasonics **32**, 447 (1994).
26) A. A. Doinikov, J. F. Haac, and P. A. Dayton, Ultrasonics **49**, 263 (2009).
27) W. Soliman, T. Nakano, N. Takada, and K. Sasaki, Jpn. J. Appl. Phys. **49**, 116202 (2010).
28) C. S. Carlson, R. Matsumoto, K. Fushino, M. Shinzato, N. Kudo, and M. Postema, Jpn. J. Appl. Phys. **60**, SDDA06 (2021).
29) P. J. A. Frinking and N. de Jong, Ultrasound Med. Biol. **24**, 523 (1998).
30) H. Wang and P. R. Brito-Parada, J. Colloid Interface Sci. **587**, 14 (2021).
31) N. Kudo, R. Uzbekov, R. Matsumoto, R. Shimizu, C. S. Carlson, N. Anderton, A. Deroubaix, C. Penny, A. T. Poortinga, D. M. Rubin, A. Bouakaz, and M. Postema, Jpn. J. Appl. Phys. **59**, SKKE02 (2020).
32) A. T. Poortinga, Colloids Surf. A: Physicochem. Eng. Aspects **419**, 15 (2013).
33) A. Panfilova, P. Chen, R. J. G. van Sloun, H. Wijkstra, M. Postema, A. T. Poortinga, and M. Mischi, Med. Phys. **48**, 6765 (2021).
34) N. Kudo, IEEE Trans. Ultrason. Ferroelect. Freq. Control **64**, 273 (2017).
35) S. Imai and N. Kudo, Proc. IEEE Int. Ultrason. Symp., 2018, p. 184.
36) N. de Jong, PhD Thesis, Erasmus Univ. Rotterdam, 1993.

List of figures

Fig. 1. Radius measured as a function of time for a Pickering-stabilised microbubble of initial radius $R_0 = 4.9\,\mu$m, subjected to three consecutive ultrasound pulses. The response owing to the first pulse is shown in black, to the second pulse in dark purple, and to the third pulse in bottle green.

Fig. 2. Radius measured as a function of time for a Pickering-stabilised microbubble (○), simulated $R(t)$ curves of a free (—) and a shell-stabilised (**—**) microbubble of $R_0 = 4.6\,\mu$m, and inlays extracted from high-speed video footage. Each inlay corresponds to a 15-μm diameter.

Fig. 3. Scatter plot of maximum microbubble expansion measured as a function of initial radius (○), overlain with simulated $R_{\max}(R_0)$ curves of free (—) and Pickering-stabilised (**—**) microbubbles.

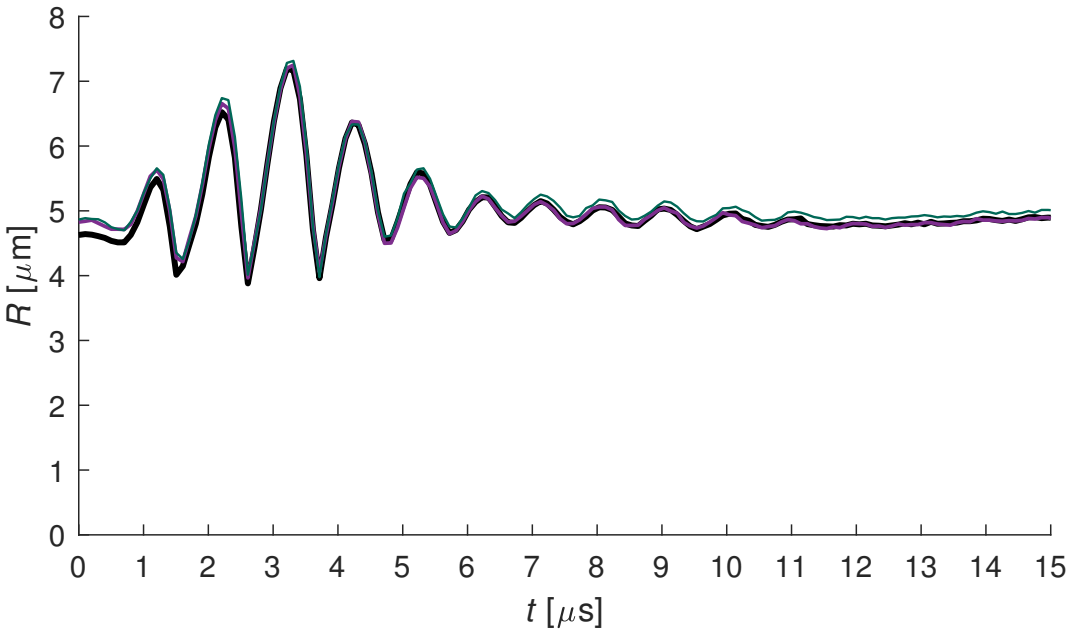

Fig. 1. Radius measured as a function of time for a Pickering-stabilised microbubble of initial radius $R_0 = 4.9\ \mu$m, subjected to three consecutive ultrasound pulses. The response owing to the first pulse is shown in black, to the second pulse in dark purple, and to the third pulse in bottle green.

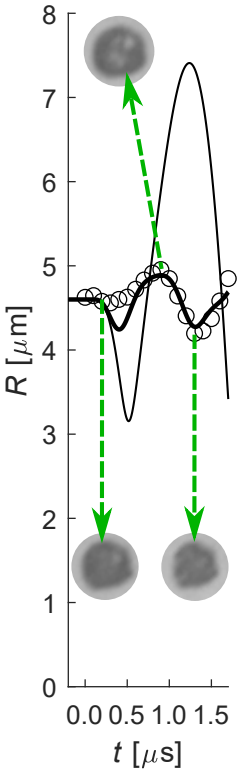

Fig. 2. Radius measured as a function of time for a Pickering-stabilised microbubble (○), simulated $R(t)$ curves of a free (—) and a shell-stabilised (**—**) microbubble of $R_0 = 4.6\ \mu$m, and inlays extracted from high-speed video footage. Each inlay corresponds to a 15-μm diameter.

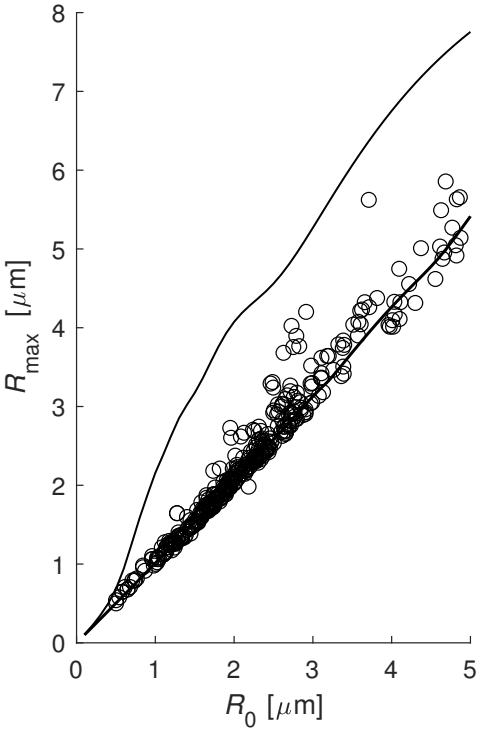

Fig. 3. Scatter plot of maximum microbubble expansion measured as a function of initial radius (○), overlain with simulated $R_{max}(R_0)$ curves of free (—) and Pickering-stabilised (**—**) microbubbles.

PUBLICATION V

First-cycle oscillation excursions of Pickering-stabilised microbubbles subjected to a high-amplitude ultrasound pulse

N. Anderton, C. S. Carlson, R. Matsumoto, R.-i. Shimizu, A. T. Poortinga, N. Kudo, and M. Postema

Current Directions in Biomedical Engineering, vol. 8, no. 2, pp. 30–32
DOI: 10.1515/cdbme-2022-1009

Nicole Anderton*, Craig S. Carlson, Ryunosuke Matsumoto, Ri-ichiro Shimizu, Albert T. Poortinga, Nobuki Kudo, and Michiel Postema

First-cycle oscillation excursions of Pickering-stabilised microbubbles subjected to a high-amplitude ultrasound pulse

https://doi.org/10.1515/cdbme-2022-1009

Abstract: Pickering stabilisation is a manufacturing process involving the adsorption of colloidal particles at gas–liquid interfaces. It is used to create the shells of stable, long-lived ultrasound contrast agent microbubbles. The purpose of the present study is to determine whether high-amplitude sonication influences the integrity of Pickering-stabilised shells. To this purpose, Pickering-stabilised microbubbles were subjected to high-speed photography at 10 million frames per second during 1-MHz, 1-MPa sonication. In addition, radial excursions as a function of time were simulated using the Rayleigh-Plesset equation for free gas microbubbles and microbubbles encapsulated by Pickering-stabilised shells of 7.6-N m^{-1} stiffness. The maximum expansions observed from camera recordings were either agreeing with those computed for Pickering-stabilised microbubbles or corresponding to greater values. The results indicate that optically identical microbubbles may undergo shell disruption of different severity. We conclude that the disruption occurs during sonication and not prior to it. These findings may aid in the development of Pickering-stabilised agents that facilitate ultrasound-triggered release.

Keywords: Acoustic cavitation, ultrasound contrast agent, shell stiffness, microbubble oscillation modelling, high-speed photography.

***Corresponding author: Nicole Anderton,** BioMediTech, Faculty of Medicine and Health Technology, Tampere University, Korkeakoulunkatu 3, 33720 Tampere, Finland, e-mail: nicole.anderton@tuni.fi

Craig S. Carlson, Michiel Postema, BioMediTech, Faculty of Medicine and Health Technology, Tampere University, Tampere, Finland and School of Electrical and Information Engineering, University of the Witwatersrand, Johannesburg, Braamfontein, South Africa

Ryunosuke Matsumoto, Ri-ichiro Shimizu, Nobuki Kudo, Faculty of Information Science and Technology, Hokkaido University, Sapporo, Hokkaido, Japan

Albert T. Poortinga, Department of Mechanical Engineering, Eindhoven University of Technology, Eindhoven, Netherlands

1 Introduction

Ultrasound contrast agents comprising gas microbubbles surrounded by stabilising elastic or viscoelastic shells are commonly used in diagnosis [1, 2]. Their highly nonlinear oscillation behaviour makes them suitable aides for harmonic ultrasonic imaging [3]. The dynamics of individual ultrasound contrast agent microbubbles under sonication has traditionally been studied with high-speed photography setups [4, 5]. The manufacturing process of more stable, very long-lived microbubbles involves the adsorption of colloidal particles at the interfaces, a process which is called Pickering stabilisation [6]. This process has been extensively used to stabilise emulsions, albeit rarely in combination with acoustics [7–9]. Pickering-stabilised microbubbles and antibubbles have been observed to generate a harmonic acoustic response, even at modest transmission amplitudes [10]. Therefore, Pickering-stabilised ultrasound contrast agents may be of interest in contrast-enhanced ultrasonic imaging [10, 11]. In a previous study, we determined the shell stiffness of Pickering-stabilised microbubbles from oscillation excursion data using low-amplitude sonication [11]. The stiffness was found to be 7.6 N m^{-1} [11]. The purpose of the present study is to determine whether high-amplitude sonication influences the integrity of the Pickering-stabilised shell.

2 Materials and methods

Pickering-stabilised microbubbles were produced with Aerosil® R972 hydrophobised silica particles (Evonik Industries AG, Essen, Germany) as a stabilising agent, identical to the procedure in our previous studies [10, 11]. A 0.2-ml volume of microbubble suspension was pipetted into the observation chamber of a high-speed observation system, which was placed under an Eclipse Ti inverted microscope (Nikon Corporation, Minato-ku, Tokyo, Japan) with a Plan Apo LWD 40× WI (N.A. 0.8) objective lens. The microscope was coupled to an HPV-X2 high-speed camera (Shimadzu, Nakagyo-ku, Kyoto, Japan), operating at a recording speed of 10 million

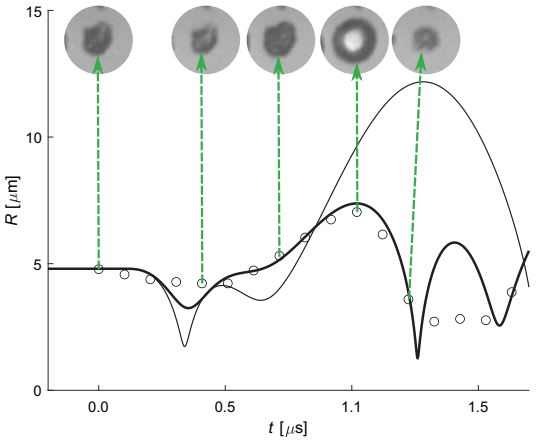

Fig. 1: Radius measured as a function of time for a Pickering-stabilised microbubble (○), simulated $R(t)$ curves of a free (—) and a shell-stabilised (—) microbubble of R_0=4.8 μm, and inlays extracted from high-speed video footage. Each inlay corresponds to a 22-μm diameter.

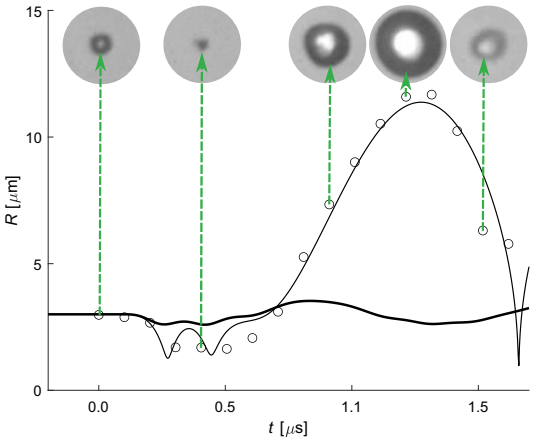

Fig. 2: Radius measured as a function of time for a Pickering-stabilised microbubble (○), simulated $R(t)$ curves of a free (—) and a shell-stabilised (—) microbubble of R_0=3.0 μm, and inlays extracted from high-speed video footage. Each inlay corresponds to a 22-μm diameter.

frames per second with exposure times of 100 ns per frame. High-speed videos were recorded during sonication. A burst comprised a 3-cycle sine pulse with a centre frequency of 1 MHz and a peak-negative pressure of 1.0 MPa, which corresponds to a high mechanical index of 1.0. The frames were clipped, segmented, and analysed using MATLAB® (The MathWorks, Inc., Natick, MA, USA). A total number of one hundred different microbubbles was included in this study. In addition, radius as a function of time, $R(t)$, curves were computed from the Rayleigh-Plesset equation [12], using the ode45 differential equation solver of MATLAB®, for free gas microbubbles and for microbubbles encapsulated by shells with a 7.6-N m^{-1} stiffness [11]. The latter can be explained if shell disruption took place during the first oscillation cycle.

3 Results and discussion

Figure 1 shows the radial dynamics during the first oscillation cycle of a Pickering-stabilised microbubble of 4.8-μm initial radius. The measured data correspond to the first cycle of the simulated $R(t)$ curve of a microbubble with shell stiffness of 7.6 N m^{-1} and clearly do not correspond to the much greater expansion of a free microbubble. The microbubble did not appear to have undergone disruption during its first expansion. Figure 2 shows the radial dynamics during the first oscillation cycle of a Pickering-stabilised microbubble of 3.0-μm initial radius. The measured data correspond to the first cycle of the simulated $R(t)$ curve of a free microbubble and clearly do not correspond to the almost negligible expansion of a microbubble with shell stiffness 7.6 N m^{-1}. The microbubble whose dynamics are shown in Figure 2 did not appear to have undergone gas release. From this observation, we deduct, that stabilising particles must have been present on the interface during expansion. From the large expansion, however, we conclude that, if indeed stabilising particles were present on the interface, these did not form a uniform stabilising shell.

Figure 3 shows an overview of measured first-cycle oscillation amplitudes, $R_{\max}$, as a function of initial radius, R_0. Some 40% of the microbubbles had expanded to excursions computed for microbubbles with a shell stiffness of 7.6 N m^{-1}. The remaining microbubbles had expanded to greater excursions, with only three microbubbles reaching free-gas bubble excursions. Microbubbles of the same initial radius were observed to expand to different maxima. This could indicate that optically identical microbubbles may have different shell properties. However, that would also mean that maximum excursions at lower acoustic amplitudes should be different for optically identical bubbles, which they are not [11]. A different explanation for the observed excursion amplitudes is that optically identical microbubbles may undergo shell disruption of different severity. Although disruption prior to sonication might be possible, we rule it out for an explanation based on the consistency of excursion observations at low acoustic amplitudes [11]. In the absence of other mechanisms observed, we hold the explanation that the disruption occurs during first expansion for most plausible.

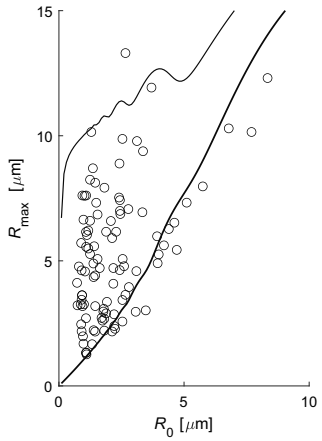

Fig. 3: Scatter plot of maximum microbubble expansion measured as a function of initial radius (○), overlain with simulated $R_{max}(R_0)$ curves of free (—) and Pickering-stabilised (—) microbubbles.

4 Conclusions

In summary, the maximum radial expansions observed were either agreeing with the maxima predicted by the model of Pickering-stabilised microbubbles or corresponding to greater values. These observations support the hypothesis that the rigidity of Pickering-stabilised shells is affected by sonication. Nevertheless, gas release from these disrupted microbubbles was not observed, indicating that the particle structuring remained on the interface during radial oscillation. The results indicate that optically identical microbubbles may undergo shell disruption of different severity. We conclude that the disruption occurs during sonication and not prior to it.

These findings may aid in the development of Pickering-stabilised agents that facilitate ultrasound-triggered release.

Author statement

Research funding: This work was supported by JSPS KAKENHI, Grant Numbers JP17H00864 and JP20H04542, by the National Research Foundation of South Africa, Grant Number 127102, and by the Academy of Finland, Grant Number 340026. Conflict of interest: Authors state no conflict of interest. Informed consent: Authors state that informed consent is not applicable. Ethical approval: Authors state that no ethical approval was required for this research as no human or animal samples or data were used.

References

[1] Park S, Yoon H, Emelianov S, Aglyamov S. Fluid flow measurement for diagnosis of ventricular shunt malfunction using nonlinear responses of microbubbles in the contrast-enhanced ultrasound imaging. Jpn J Appl Phys 2017;56:07JF10.

[2] Kikuchi Y, Kanagawa T. Weakly nonlinear theory on ultrasound propagation in liquids containing many microbubbles encapsulated by viscoelastic shell. Jpn J Appl Phys 2021;60:07JF10.

[3] Mleczko M, Postema M, Schmitz G. Nonlinear modeling of ultrasound contrast agents with Wiener series. Gemeinsame Jahrestagung der Deutschen, Österreichischen und Schweizerischen Gesellschaft für Biomedizinische Technik 2006:#V77.

[4] Postema M, Mleczko M, Schmitz G. Experimental setup for synchronous optical and acoustical observation of contrast microbubbles. Gemeinsame Jahrestagung der Deutschen, Österreichischen und Schweizerischen Gesellschaft für Biomedizinische Technik 2006:#V75.

[5] Postema M, Schmitz G. Messung und Modellierung physikalischer Eigenschaften von Kontrastmitteln. In: Langer S, Scholl W, Wittstock V, editors. Fortschritte der Akustik: Plenarvorträge und Fachbeiträge der 32. Deutschen Jahrestagung für Akustik DAGA '06, Braunschweig. Berlin: DEGA 2006:37–38.

[6] Poortinga AT. Long-lived antibubbles: stable antibubbles through Pickering stabilization. Langmuir 2011;27:2138–2141.

[7] Melle S, Lask M, Fuller GG. Pickering emulsions with controllable stability. Langmuir 2005, 21, 2158–2162.

[8] Chevalier Y, Bolzinger M-A. Emulsions stabilized with solid nanoparticles: Pickering emulsions. Colloids Surf. A: Physicochem. Eng. Asp. 2013;439:23–34.

[9] Wu J, Ma G-H. Recent studies of pickering emulsions: particles make the difference. Small 2016;12:4633–4648.

[10] Kudo N, Uzbekov R, Matsumoto R, Shimizu R, Carlson CS, Anderton N, et al. Asymmetric oscillations of endoskeletal antibubbles. Jpn J Appl Phys 2020;59:SKKE02.

[11] Anderton N, Carlson CS, Matsumoto R, Shimizu R, Poortinga AT, Kudo N, et al. On the rigidity of four hundred Pickering-stabilised microbubbles. Jpn J Appl Phys 2022;61:ac4adc.

[12] Postema M, de Jong N, Schmitz G. The physics of nanoshelled microbubbles. Biomed Tech 2005;50(S1):748–749.

PUBLICATION VI

Fragmentation thresholds simulated for antibubbles with various infinitesimal elastic shells

N. Anderton and M. Postema

Current Directions in Biomedical Engineering, vol. 8, no. 2, pp. 73–76
DOI: 10.1515/cdbme-2022-1020

Nicole Anderton* and Michiel Postema

Fragmentation thresholds simulated for antibubbles with various infinitesimal elastic shells

https://doi.org/10.1515/cdbme-2022-1020

Abstract: Antibubbles are small gas bubbles comprising one or multiple liquid or solid cores, typically surrounded by stabilising shells. Acoustically active microscopic antibubbles have been proposed for use as theranostic agents. For clinical applications such as ultrasound-guided drug delivery and flash-echo, it is relevant to know the fragmentation threshold of antibubbles and the influence of the stabilising shells thereon. For antibubbles with an infinitesimal frictionless elastic shell of constant surface tension, we simulated ultrasound-assisted fragmentation by computing radial pulsation as a function of time using an adapted Rayleigh-Plesset equation, and converting the solutions to time-variant kinetic energy of the shell and time-variant surface energy deficit. By repetition over a range of pressure amplitudes, fragmentation thresholds were found for antibubbles of varying size, core volume, shell stiffness, and driving frequency. As backscattering increases with scatterer size, and as drug delivery would require vehicles just small enough to pass through capillaries with a relatively large payload, we chose to present typical results for antibubbles of resting diameter 6 μm with a 90% incompressible core. At a driving frequency of 13 MHz, the fragmentation threshold was found to correspond to a mechanical indices less than 0.4, irrespective of shell stiffness. This mechanical index is not considered unsafe in diagnosis. That means that antibubbles acting as drug-carrying vehicles could release their payload under diagnostic conditions.

Keywords: Acoustic fragmentation, ultrasound contrast agent, shell stiffness, antibubble oscillation modelling, Rayleigh-Plesset equation.

***Corresponding author: Nicole Anderton,** BioMediTech, Faculty of Medicine and Health Technology, Tampere University, Korkeakoulunkatu 3, 33720 Tampere, Finland, e-mail: nicole.anderton@tuni.fi

Michiel Postema, BioMediTech, Faculty of Medicine and Health Technology, Tampere University, Tampere, Finland and School of Electrical and Information Engineering, University of the Witwatersrand, Johannesburg, Braamfontein, South Africa

1 Introduction

Ultrasound contrast agents are used both in diagnosis and therapy, and are therefore referred to as theranostic agents [1]. They comprise microscopic gas bubbles surrounded by stabilising shells [2]. The pulsation dynamics of a spherically symmetric microbubble surrounded by an elastic shell has been modelled with a Rayleigh-Plesset equation, adjusted for the presence of a shell by introducing a shell stiffness parameter [2–5]. Knowing under which conditions ultrasound contrast agent microbubbles fragment might be of interest in echography and ultrasound-guided drug delivery [6, 7]. Shell-encapsulated microbubbles, called parents, subjected to pressures below the inertial cavitation threshold have been observed to typically fragment into eight or more so-called daughter microbubbles [8]. The number of fragments depends on the energy subjected to the parent [8]. The presence of a shell has been found to be of influence on the fragmentation threshold of such microbubbles [7].

Antibubbles are small gas bubbles comprising one or multiple liquid or solid cores [9]. If a surrounding shell is absent, an antibubble is very short-lived [10–12]. The presence of an encapsulating shell or an endoskeleton drastically increases the antibubble lifetime [13–16]. Fluids comprising antibubbles have been proposed for the use as theranostic agents [11, 15, 17, 18].

The dynamic response of microscopic antibubbles by stabilising shells subjected to ultrasound has been studied *in silico* [19, 20], *in vitro* [16, 18, 21], and, more recently, *in vivo* [22]. The simulations and experiments of most of these preliminary studies concentrated on the radial pulsations of antibubbles and the accompanying generation of harmonics. These studies were highly relevant for potential applications of antibubbles in diagnostic harmonic imaging. For potential therapeutic applications of antibubbles, however, it is more relevant to know under which acoustic conditions the core material is released [22]. Ultrasound-assisted disruption of microscopic antibubbles had been demonstrated by high-speed camera footage [21, 22]. From such footage, the fragment size distribution could be predicted [23].

The purpose of this study was to simulate the fragmentation threshold of microscopic antibubbles with infinitesimal

shells of different biomaterial composition. The outcomes of this study may aid in the development of novel theranostic antibubble agents.

2 Methods

An infinite viscous fluid was assumed to surround a perfectly spherical shell-encapsulated antibubble containing one or multiple incompressible cores, subjected to a sound pulse whose wavelength is much greater than the antibubble size. The shell was considered homogeneous, of infinitesimal thickness, elastic, frictionless, and of constant surface tension. For modelling purposes, we replaced the total core volume inside the antibubble by an equivalent core radius. Following a prior derivation [24] but incorporating damping and shell stiffness terms [25], the resulting fundamental pulsation equation used in this study is then given by

$$R\ddot{R}+\tfrac{3}{2}\dot{R}^2=\frac{1}{\rho}\left[\left(p_0-p_\mathrm{v}+\frac{2\sigma R_0}{R_0^2-R_\mathrm{c}^2}\right)\left(\frac{R_0^3-R_\mathrm{c}^3}{R^3-R_\mathrm{c}^3}\right)^{\gamma}+p_\mathrm{v}-\frac{2\sigma R}{R^2-R_\mathrm{c}^2}-2\chi\left(\frac{1}{R_0}-\frac{1}{R}\right)-\frac{4\eta\dot{R}}{R}-\delta\omega\rho R\dot{R}-p_0-p(t)\right]\ , \tag{1}$$

where $p(t)$ is the time-dependent acoustic driving function, p_0 is the ambient pressure, p_v is the vapour pressure, R is the instantaneous radius, R_0 is the initial radius, R_c is the equivalent core radius, γ is the ratio of specific heats, δ is the damping coefficient, η is the liquid viscosity, ρ is the liquid density, σ is the surface tension, χ is the shell stiffness, and ω is the angular driving frequency. The viscous damping had been directly included in (1). Therefore, the damping coefficient δ only comprised the damping owing to reradiation and the thermal damping, $\delta\approx\frac{\omega R}{c}+\frac{3}{5}(\gamma-1)$, where c is the speed of sound of the medium. The angular resonance frequency of a shell-encapsulated antibubble was found by adjusting the resonance frequency of a free-surface antibubble [21] for the surface pressure components in (1) and for the presence of an infinitesimal elastic shell [7]:

$$\omega_\mathrm{r}=\frac{1}{R_0\sqrt{\rho}}\sqrt{\frac{3\gamma\left(p_0-p_\mathrm{v}+\frac{2\sigma R_0}{R_0^2-R_\mathrm{c}^2}\right)}{1-\frac{R_\mathrm{c}{}^3}{R_0^3}}-\frac{2\sigma R_0}{R_0^2-R_\mathrm{c}^2}+\frac{4\eta^2}{R_0^2\rho}+\frac{2\chi}{R_0}}\ . \tag{2}$$

The fragmentation threshold pressure was defined as the acoustic pressure amplitude at which the kinetic energy of the parent surface [26]

$$E_\mathrm{k}\approx 2\pi\rho R^3\dot{R}^2 \tag{3}$$

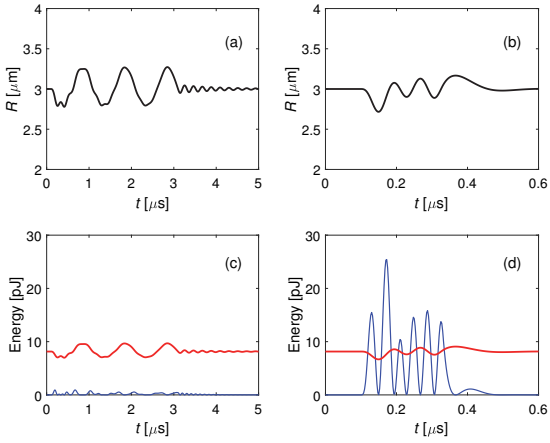

Fig. 1: Radius and instantaneous energies as a function of time simulated for an antibubble of initial radius $R_0=3\,\mu$m with a 90% core radius and shell stiffness $\chi=7.6\,\mathrm{N\,m^{-1}}$ driven with a 0.6-MI pulse of centre frequency 1 MHz (a,c) and 13 MHz (b,d). Instantaneous kinetic energies are indicated by blue lines and surface energy deficits by red lines.

surpassed the difference in surface energy between the parent entity and at least eight daughters [6, 7],

$$\Delta E_\mathrm{s}\approx 4\pi R^2\sigma\ , \tag{4}$$

here referred to as energy deficit.

Numerical solutions of (1) were computed using the `ode45` differential equation solver of MATLAB® (The MathWorks, Inc., Natick, MA, USA). The three-cycle sinoidal acoustic driving function was defined by $p(\omega t)=A\sin\omega t\ \forall\ \omega t\in[0,6\pi]\ \wedge\ p(\omega t)=0\ \forall\ \omega t\notin[0,6\pi]$, in which A was varied to find the fragmentation pressure threshold. The following parameters were chosen in the simulations: $c=1568\,\mathrm{m\,s^{-1}}$, representing saline [27], $p_0=1.00$ atm, $p_\mathrm{v}=2.33\,$kPa, $\gamma=1.4$, $\eta=1.00\,$mPa s, $\rho=998\,\mathrm{kg\,m^{-3}}$, $\sigma=0.072\,\mathrm{N\,m^{-1}}$. Values of R_0, R_c, χ, and ω were variables. Throughout this paper, R_c is expressed as a percentage of R_0. The $R(t)$ curves computed and their time derivatives were converted to kinetic energy and surface energy deficit vectors. Fragmentation pressure thresholds were expressed in mechanical index,

$$\mathrm{MI}=\frac{A\,[\mathrm{MPa}]}{\sqrt{\frac{\omega}{2\pi}\,[\mathrm{MHz}]}}\ , \tag{5}$$

for interpreting the clinical relevance of the findings. An MI$\leq$0.7 is not considered unsafe [28]. Through iteration in MI steps of 0.005, the fragmentation threshold was determined automatically as a function of the variables of choice. The size range was limited to radii small enough to pass through capillaries. The range of shell stiffnesses was limited to those com-

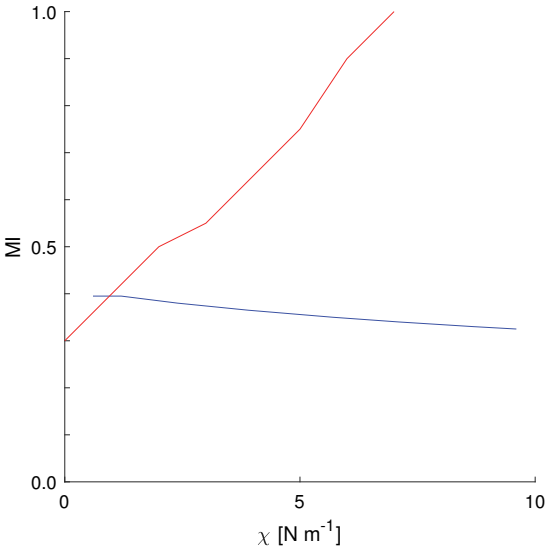

Fig. 2: Fragmentation threshold in MI as a function of shell stiffness χ, simulated for a 3-μm radius antibubble with a 90% core radius, subjected to a pulse of centre frequency 1 MHz (red) and 13 MHz (blue).

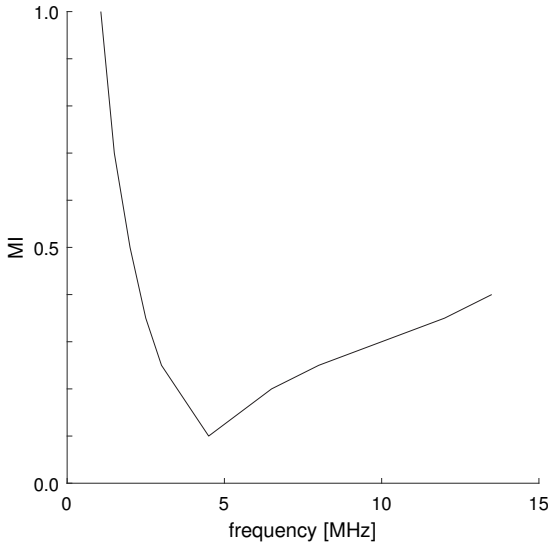

Fig. 3: Fragmentation threshold in MI as a function of driving frequency, simulated for a 3-μm radius antibubble with a 90% core radius and a 7.6-N m^{-1} shell stiffnes.

mon in biomaterials. The frequency range was limited to those common in commercial probes.

3 Results and discussion

Two representative $R(t)$ curves and their corresponding instantaneous energies are shown in Figure 1, for an antibubble of 3-μm initial radius with a 90% core radius, subjected to a 0.6-MI pulse. At a 1-MHz driving frequency, the kinetic energy simulated was too low to cause fragmentation. At a 13-MHz driving frequency, however, the kinetic energy clearly surpassed the surface energy deficit to cause fragmentation.

Figure 2 shows the fragmentation threshold for 3-μm radius antibubbles as a function of shell stiffness at two different sonication frequencies. At a 1-MHz driving frequency, the fragmentation threshold was found to increase with shell stiffness. Here, antibubbles with a shell stiffness less than 7 N m^{-1} were simulated to fragment at an MI$\leq$1. At a 13-MHz driving frequency, however, the fragmentation threshold was found to decrease with shell stiffness. Here, for each stiffness simulated, antibubbles fragmented at an MI$<$0.4. A straightforward explanation of this counterintuitive result is that the resonance frequency of an antibubble increases with its shell stiffness. Consequently, the difference between antibubble resonance and driving frequency may increase or decrease with shell stiffness. The fragmentation threshold should be lowest at resonance. The size of the antibubble core was observed to be only of minor influence on the fragmentation threshold (data not shown).

Figure 3 shows the fragmentation threshold for 3-μm radius antibubbles with shells of 7.6-N m^{-1} stiffness and a 90% equivalent core radius as a function of driving frequency. For driving frequencies greater than 1.5 MHz, the fragmention thresholds corresponded to MI < 0.7. The fragmentation threshold had a minimum of MI = 0.1 at a driving frequency of 4.5 MHz. From (2), it followed that the resonance frequency of such an antibubble is 4.54 MHz. Hence, the driving frequency at the simulated minimum corresponded to the resonance frequency.

Even at a core radius of 90% of the antibubble radius, the fragmentation threshold at 13-MHz driving corresponded to an MI of less than 0.4, which is not considered unsafe in diagnosis. As a consequence, antibubbles acting as drug-carrying vehicles would release their payload under diagnostic conditions.

4 Conclusions

Our simulations show that at lower driving frequencies, the shell stiffness is of major influence on antibubble fragmentation, whilst at higher driving frequencies, the shell mate-

rial is hardly of influence. At 13-MHz driving, stiff-shell-encapsulated antibubbles were simulated to fragment at acoustic amplitudes that are not considered unsafe in diagnosis. These findings imply that drug-loaded antibubbles, stabilised by rigid shells, could be forced to release their contents using diagnostic ultrasound. This research is of interest in flash-echo and ultrasound-guided drug delivery.

Author statement

Research funding: This work was supported by the National Research Foundation of South Africa, Grant Number 127102, and by the Academy of Finland, Grant Number 340026. Conflict of interest: Authors state no conflict of interest. Informed consent: Authors state that informed consent is not applicable. Ethical approval: Authors state that no ethical approval was required for this research as no human or animal samples or data were used.

References

[1] Duan L, Yang L, Jin J, Yang F, Liu D, Hu K, et al. Micro/nanobubble-assisted ultrasound to enhance the EPR effect and potential theranostic applications. Theranostics 2020;10:462–483.
[2] de Jong N, Cornet R, Lancée CT. Higher harmonics of vibrating gas-filled microspheres. Ultrasonics 1994;32:447–453.
[3] Church CC. The effects of an elastic solid surface layer on the radial pulsations of gas bubbles. J Acoust Soc Am 1995;97:1510–1521.
[4] Postema M, de Jong N, Schmitz G. The physics of nanoshelled microbubbles. Biomed Tech 2005;50(S1):748–749.
[5] Mehrem AM. Theoretical study of microbubble dynamics under the action of ultrasound fields. MSc Diss, Universitat Politècnica de València 2013.
[6] Postema M, Schmitz G. Ultrasonic fragmentation of microbubbles: a theoretical approach of the flash in flash-echo. Proc IEEE Eng Med Biol Annu Conf 2005;27:4023–4026.
[7] Postema M, Schmitz G. Ultrasonic bubbles in medicine: influence of the shell. Ultrason Sonochem 2007;14:438–444.
[8] Postema MAB. Medical bubbles. PhD Thesis, University of Twente 2004.
[9] Johansen K, Kotopoulis S, Postema M. Introduction to antibubbles. In: Korneliussen RJ, editor. Proceedings of the 38th Scandinavian Symposium on Physical Acoustics, Geilo 1–4 February 2015. Bergen: CMR; 2015:1–6.
[10] Dorbolo S, Caps H, Vandewalle N. Fluid instabilities in the birth and death of antibubbles. New J Phys 2003;5:161.
[11] Vitry Y, Dorbolo S, Vermant J, Scheid B. Controlling the lifetime of antibubbles. Adv Colloid Interface Sci 2019;270:73–86.
[12] Zou J, Ji C, Yuan BG, Ruan XD, Fu X. Collapse of an antibubble. Phys Rev E 2013;87:061002.
[13] Poortinga AT. Long-lived antibubbles: stable antibubbles through Pickering stabilization. Langmuir 2011;27:2138–2141.
[14] Poortinga AT. Micron-sized antibubbles with tunable stability. Colloids Surf A 2013;419:15–20.
[15] Shen Y, Hu L, Chen W, Xie HH, Fu X. Drop encapsulated in bubble: a new encapsulation structure. Phys Rev Lett 2018;120:054503.
[16] Panfilova A, Chen P, van Sloun RJG, Wijkstra H, Postema M, Poortinga AT, et al. Experimental acoustic characterization of an endoskeletal antibubble contrast agent: first results. Med Phys 2021;48:6765–6780.
[17] Postema M, ten Cate FJ, Schmitz G, de Jong N, van Wamel A. Generation of a droplet inside a microbubble with the aid of an ultrasound contrast agent: first result. Lett Drug Des Discov 2007;4:74–77.
[18] Postema M, Novell A, Sennoga C, Poortinga AT, Bouakaz A. Harmonic response from microscopic antibubbles. Appl Acoust 2018;137:148–150.
[19] Kotopoulis S, Johansen K, Gilja OH, Poortinga AT, Postema M. Acoustically active antibubbles. Acta Phys Pol A 2015;127:99–102.
[20] Johansen K, Postema M. Lagrangian formalism for computing oscillations of spherically symmetric encapsulated acoustic antibubbles. Hydroacoustics 2015;19:197–207.
[21] Kudo N, Uzbekov R, Matsumoto R, Shimizu R, Carlson CS, Anderton N, et al. Asymmetric oscillations of endoskeletal antibubbles. Jpn J Appl Phys 2020;59:SKKE02.
[22] Kotopoulis S, Lam C, Haugse R, Snipstad S, Murvold E, Jouleh T, et al. Formulation and characterisation of drug-loaded antibubbles for image-guided and ultrasound-triggered drug delivery. Ultrason Sonochem 2022;105986.
[23] Anderton N, Carlson CS, Kudo N, Poortinga AT, Postema M. The ultrasound-triggered explosion of an endoskeletal antibubble yields a predictable fragment size distribution. Jpn J Appl Phys 2021;60:128001.
[24] Carlson CS, Matsumoto R, Fushino K, Shinzato M, Kudo N, Postema M. Nucleation threshold of carbon black ultrasound contrast agent. Jpn J Appl Phys 2021;60:SDDA06.
[25] Anderton N, Carlson CS, Matsumoto R, Shimizu R, Poortinga AT, Kudo N, et al. On the rigidity of four hundred Pickering-stabilised microbubbles. Jpn J Appl Phys 2022;61:ac4adc.
[26] Doinikov AA, Dayton PA. Spatio-temporal dynamics of an encapsulated gas bubble in an ultrasound field. J Acoust Soc Am 2006;120:661–669.
[27] Carlson CS, Deroubaix A, Penny C, Postema M. On the attenuation of pure black tattoo ink. SAIEE Afr Res J 2021;112:24–31.
[28] ter Haar G. Safety and bio-effects of ultrasound contrast agents. Med Biol Eng Comput 2009;47:893–900.

PUBLICATION VII

The ultrasound-triggered explosion of an endoskeletal antibubble yields a predictable fragment size distribution

N. Anderton, C. S. Carlson, N. Kudo, A. T. Poortinga, and M. Postema

Japanese Journal of Applied Physics, vol. 60, no. 12, 128001
DOI: 10.35848/1347-4065/ac3184

Japanese Journal of Applied Physics

The Japan Society of Applied Physics

ACCEPTED MANUSCRIPT

The ultrasound-triggered explosion of an endoskeletal antibubble yields a predicable fragment size distribution

To cite this article before publication: Nicole Anderton *et al* 2021 *Jpn. J. Appl. Phys.* in press https://doi.org/10.35848/1347-4065/ac3184

Japanese Journal of Applied Physics **BRIEF NOTE**

The ultrasound-triggered explosion of an endoskeletal antibubble yields a predicable fragment size distribution

Nicole Anderton[1], Craig S. Carlson[1,2], Nobuki Kudo[3], Albert T. Poortinga[4], and Michiel Postema[1,2]*

[1]*BioMediTech, Faculty of Medicine and Health Technology, Tampere University, Korkeakoulunkatu 3, 33720 Tampere, Finland*

[2]*School of Electrical and Information Engineering, University of the Witwatersrand, Johannesburg, 1 Jan Smuts Laan, 2001 Braamfontein, South Africa*

[3]*Faculty of Information Science and Technology, Hokkaido University, Kita 14 Jo, Nishi 9 Chome, Kita-ku, Sapporo, Hokkaido 060-0814, Japan*

[4]*Department of Mechanical Engineering, Eindhoven University of Technology, De Zaale, 5600 MB Eindhoven, Netherlands*

Recently, the first high-speed video of a fragmenting antibubble was published. Nonetheless, this fragmentation process was not fully understood. Owing to a recent study on fragmenting glass, we can now conclude that an antibubble under tensile stress undergoes an exponential fragmentation process. This note gives a brief theoretical explanation and the first experimental data of a fragmenting antibubble. This is a highly relevant finding, as the fragmentation predictability of acoustically active antibubbles is required for their potential use in ultrasound-guided drug delivery.

Recently, the first high-speed video of a fragmenting antibubble was published in Ref. 1. Nonetheless, this fragmentation process was not fully understood. Owing to a recent study on fragmenting glass, we would like add a brief explanation on the fragmentation process of the antibubble. A very recent study by Kooij et al. showed that explosive fragmentation of Dutch tears leads to a predictable fragment size distribution.[2)] In addition, the study showed that an increased stress regime of millimeter- to centimeter-size glass-like materials results in an exponential, rather than a power-law distribution of the fragments. Kooij et al. did not draw conclusions on the scale-invariance of this exponential process or whether microscopic materials might yield similar fragment distributions.

We hypothesised that this elegant explanation holds for the size distribution of explosively fragmenting microscopic silica-comprising endoskeletal antibubbles during sonic smashing.[1)]

*E-mail: michiel.postema@tuni.fi

This would be a highly relevant finding, as the fragmentation predictability of acoustically active antibubbles is required for their potential use in ultrasound-guided drug delivery.[3)]

Antibubbles are by definition gas bubbles containing at least one liquid core. Although antibubbles are typically highly unstable structures,[4,5)] they may be stabilised by adsorbing colloidal particles at the interfaces, which is referred to as Pickering stabilisation.[6)] The colloidal particles may form a solid skeleton structure, fixating the liquid core, as demonstrated with the aide of confocal microscopy and scanning electron microscopy.[1)] Stabilised antibubbles have been proposed as theranostic agents.[4,5,7)]

We investigated an antibubble of 20-μm diameter comprising a solid skeleton and shell of agglomerated zinc oxide and fumed silica, whose dynamic fragmentation behaviour had been observed by us,[1)] but had not been properly understood. A still frame of the antibubble is shown in Fig. 1a. A scanning electron microscopy image of similar endoskeletal antibubbles has been shown by Kudo et al.[1)]

To cause an explosion, the antibubble (Fig. 1a) had been subjected to a three-cycles pulse of 1-MHz, 1-MPa ultrasound, whilst recorded at ten million frames per second.[1)] As antibubble fragmentation has been associated with inertial cavitation, the medium was allowed to settle and released gas allowed to diffuse or buoy for an additional minute before a still frame was recorded, shown in Fig. 1b. The 56 antibubble skeleton fragments visible in this still frame were measured using MATLAB® (The MathWorks, Inc., Natick, MA, USA). Fig. 1c shows the size distribution of these fragments, with the same representation as Kooij et al.

Following the methodology of Kooij et al., an exponential curve

$$P(d) = Ce^{d/d_1} \tag{1}$$

was fitted through the fragment size distribution. This curve-fitting yielded the distribution parameter $d_1 = 0.9\,\mu$m. The scalar value $C = 7$ is an indicator for the number of fragments included in the distribution and therefore of less interest than d_1.

Our results presented in Fig. 1c are remarkably similar to the results for tempered glass presented by Kooij et al.[2)] We attribute the overrepresentation of fragments $\frac{d}{d_c} > 3$ to the fact that a two-dimensional microscopic representation of a volumetric distribution automatically results in an overrepresentation of particles greater than the depth of field.

The exponential fit indicates that the antibubble was under tensile stress during fragmentation. We approximated the tensile stress during fragmentation by rearranging the equation relating tensile stress to characteristic length in Kooij et al.[2)] and substituting parameter values

from literature:[8,9]

$$\sigma_t = \kappa_{Ic}\sqrt{\frac{15\sqrt{3}(1+\nu)}{4\,d_c}} \approx 0.0008\,[\mathrm{MPa\,m^{\frac{1}{2}}}]\sqrt{\frac{15\sqrt{3}(1+0.2)}{4\cdot 2.5\,[\mu\mathrm{m}]}} \approx 1\,\mathrm{MPa}\,, \qquad (2)$$

where κ_{Ic} is the mode-I fracture toughness, ν is Poisson's ratio, and σ_t the tensile stress. Using conservative values when computing the tensile stress, it is clear that the stress is caused by the ultrasound field, rather than the Laplace pressure of $< 15\,\mathrm{kPa}$.

The fragmentation of the antibubble can be characterised by a single parameter, namely the distribution parameter d_1. For sonic micromaterials smashing, this parameter is a more objective descriptor than the number of fragments or their geometric spread, since microscopic images only reveal a minute slice of the full event.

One might wonder, whether the droplet core inside an antibubble is of influence on the fragment size distribution. Although endoskeletal microbubbles without cores have not been produced, we may assume that their Laplace pressure is even lower than droplet-containing endoskeletal antibubbles.[10] Assuming no other tensile stress components of relevance and assuming identical acoustic conditions, the resulting fragment distribution should be exponential then, too. As the characteristic length follows from the solid material characteristics and the tensile stress applied, the characteristic diameter of an endoskeletal microbubbles should be on the same order as an endoskeletal antibubble. This is not necessarily the case, however, for the distribution parameter, as this parameter might be influenced by the exact geometry of the structure undergoing fragmentation.

Whilst Kooij et al. performed fragmentation experiments not only under tensile stress but also in absence thereof, demonstrating the influence of the tensile stress applied on the type of size distribution,[2] we could only fragment endoskeletal antibubbles under sonication. The strength of Pickering-stabilised microbubbles has thus far prevented them from being smashed at non-stress conditions. Therefore, there remains a need for control experiments to establish, whether the fragmentation distribution under such conditions would be a power distribution, indeed. In addition, it would be of great interest to investigate why Pickering-stabilised microstructures, notoriously hard to crack under isostatic conditions, are apt to fragmentation when applying moderate dynamic pressure amplitudes.

Since Kooij et al. used glass and sugar, it is most interesting to extend this research to applications of these materials that require a known fragment size distribution. These may include the controlled smashing of sugar-coated pills for consistence checks,[11] the production of less-than-6-μm theranostic particles, and the controlled re-sizing of calibration microspheres. Furthermore, other brittle materials need to be included in such studies, such

as kidney or salivary stones.

In conclusion, the characterisation method proposed by Kooij et al. has been shown to hold for a silica-comprising antibubble. Whilst Kooij et al. found that macroscopic materials under tension yield an exponential fragment size distribution, we showed that a microscopic material under sonication yields an exponential fragment size distribution, as well.

Owing to this study, we are closer in understanding endoskeletal antibubble fragmentation and, with it, ultrasound-guided drug release from them.

Acknowledgements

This work was supported by JSPS KAKENHI, Grant Numbers JP17H00864 and JP20H04542, by the National Research Foundation of South Africa, Grant Number 127102, and by the Academy of Finland, Grant Number 340026.

Figures

Fig. 1: Fragment size distribution of an antibubble: **a** an inlay showing a still frame of the antibubble before sonication; **b** an inlay showing a still frame of the antibubble skeleton fragments 1 minute after sonication; **c** the size distribution normalised by the characteristic diameter $d_c = 2.5\,\mu$m. An exponential distribution fit $P(d) = Ce^{d/d_1}$ is indicated by a bold line.

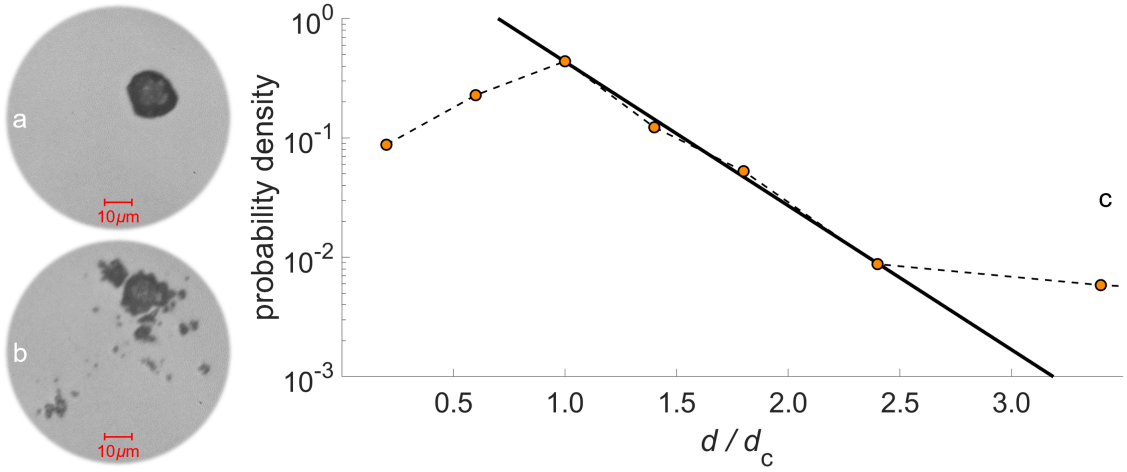

Fig. 1. Fragment size distribution of an antibubble: **a** an inlay showing a still frame of the antibubble before sonication; **b** an inlay showing a still frame of the antibubble skeleton fragments 1 minute after sonication; **c** the size distribution normalised by the characteristic diameter $d_c = 2.5\,\mu$m. An exponential distribution fit $P(d) = Ce^{d/d_1}$ is indicated by a bold line.

References

1) N. Kudo et al., Jpn. J. Appl. Phys. **59**, SKKE02 (2020).
2) S. Kooij, G. van Dalen, J.-F. Molinari, and D. Bonn, Nat. Commun. **12**, 2521 (2021).
3) M. Postema and A. Bouakaz, Appl. Acoust. **140**, 152 (2018).
4) Y. Vitry, S. Dorbolo, J. Vermant, and B. Scheid, Adv. Colloid Interface Sci. **270**, 73 (2019).
5) Y. Shen, L. Hu, W. Chen, H. Xie, H., and X. Fu, Phys. Rev. Lett. **120**, 054503 (2018).
6) A. T. Poortinga, Langmuir **27**, 2138 (2011).
7) M. Postema, A. Novell, C. Sennoga, A. T. Poortinga, and A. Bouakaz, Appl. Acoust. **137**, 148 (2018).
8) J. Phalippou, T. Woignier, and R. Rogier, J. Phys. Colloques **50**, C4-191 (1989).
9) S. P. Patil, A. Rege, S. Sagardas, M. Itskov, and B. Markert, J. Phys. Chem. B **121**, 5660 (2017).
10) C. S. Carlson, R. Matsumoto, K. Fushino, M. Shinzato, N. Kudo, and M. Postema, Jpn. J. Appl. Phys. **60**, SDDA06 (2021).
11) M. Postema and A. J. Smith, Int. Patent Appl. WO 2010/055337 A1 (2010).

PUBLICATION VIII

Sonic disruption of wood pulp fibres aided by hydrophobic cavitation nuclei

N. Anderton, C. S. Carlson, A. T. Poortinga, H. Xinyue, N. Kudo, and M. Postema

Japanese Journal of Applied Physics, vol. 62, no. 1, 018001
DOI: 10.35848/1347-4065/acaadd

Japanese Journal of Applied Physics

The Japan Society of Applied Physics

ACCEPTED MANUSCRIPT

Sonic disruption of wood pulp fibres aided by hydrophobic cavitation nuclei

To cite this article before publication: Nicole Anderton *et al* 2022 *Jpn. J. Appl. Phys.* in press https://doi.org/10.35848/1347-4065/acaadd

Japanese Journal of Applied Physics **BRIEF NOTE**

Sonic disruption of wood pulp fibres aided by hydrophobic cavitation nuclei

Nicole Anderton[1], Craig S. Carlson[1,2]*, Albert T. Poortinga[3], Hu Xinyue[4], Nobuki Kudo[4], and Michiel Postema[1,2]

[1]*BioMediTech, Faculty of Medicine and Health Technology, Tampere University, Korkeakoulunkatu 3, 33720 Tampere, Finland*

[2]*School of Electrical and Information Engineering, University of the Witwatersrand, Johannesburg, 1 Jan Smuts Laan, 2001 Braamfontein, South Africa*

[3]*Department of Mechanical Engineering, Eindhoven University of Technology, De Zaale, 5600 MB Eindhoven, The Netherlands*

[4]*Faculty of Information Science and Technology, Hokkaido University, Kita 14 Jo, Nishi 9 Chome, Kita-ku, Sapporo, Hokkaido 060-0814, Japan*

For paper manufacturing and biofuel production, the controlled deformation of wood pulp is of interest, provided that the integrity of the fibre structure remains intact. Conventional ultrasonic pretreatment in the near-audible range has been observed to cause uncontrolled inertial cavitation damage in the wood pulp fibres. To prevent internal damage, we proposed to subject wood pulp mixed with hydrophobic particles to 1-MHz short pulses above the nucleation threshold of the particles but below the Blake threshold, and to observe the interaction of pulsating cavities and wood pulp fibres assisted by high-speed photography. Our 1-MHz results showed the interaction of a collapsing bubble with a wood pulp fibre wall to form a liquid jet hitting the fibre, without apparent destruction of the structure, whilst our 20-kHz controls confirmed previously observed structural destruction. This study shows the feasibility of controlled wood fibre deformation at a high ultrasound frequency.

Wood pulp is used for making paper, but also of interest in the production of biofuel.[1,2)] The controlled deformation of wood pulp fibres is desired in processes where the cells need to be accessed by chemical agents and enzymes.[1)] In numerous independent studies, inertial cavitation generated during ultrasonic pretreatment of wood pulp fibres has been shown to not only increase the permeability of the cell walls, but also to disintegrate the structure of the fibres.[3–6)] Cavitation-induced permeation was recently confirmed in solid wood, as well.[7)] Whilst permeation is desirable in industrial processes, structural disintegration is not.[1)] As for the experimental settings in these prior studies, the inertial cavitation-generating ultrasonic

*E-mail: craig.carlson@tuni.fi

apparatus used were operating in the near-audible frequency range, whilst sonication was varied from minutes to hours.[3–6] Such acoustic conditions have been associated with the unwanted production of free radicals and deposition of heat.[8–11] Pretreatment with steam has also been shown to lead to disruptive effects, such as the visible destruction of so-called boarded pits.[12]

Under less powerful, clinical diagnostic sonication conditions, movement and permeation of cultured human and animal cells have been observed, too, but with less unwanted bioeffects.[13–17] This type of ultrasound-assisted cell permeation requires the presence of microbubbles or cavitation nuclei in or near the cells under sonication.[18–20] The asymmetric collapse of a pulsating microbubble near an interface has been observed to cause liquid jets impacting and penetrating the interface.[21] As the interaction between cavitation nuclei and cells may happen within an ultrasound cycle, experimental optical observations are typically done aided by high-speed photography through a microscope system.[22–24] We hypothesised that such a procedure would aid in the observation of wood pulp cell permeation, provided that the nucleation location is controlled to be outside the fibre rather than inside.

The purpose of this study was to subject wood pulp mixed with hydrophobic particles to ultrasound pulses of high enough acoustic amplitudes to cause the particles to nucleate but of low enough acoustic amplitude to prevent spontaneous inertial cavitation in different parts of the mixture.

At acoustic amplitudes high enough to generate inertial cavitation, microbubble-based nuclei are typically very short-lived, due to fragmentation processes.[25,26] As an alternative to these rapidly destroyed nuclei, zinc oxide hydrophobic particles have been proposed for longer lasting nucleation.[27] It has been observed, that the nucleation threshold of hydrophobic particles, but also of hydrophilic particles, is lower than the so-called Blake cavitation threshold.[28–30]

Let us assume a perfectly spherical hydrophobic core comprising one or multiple particles surrounded by a bubble of a size proportional to this hydrophobic core and in suspension in an infinite liquid. Following the derivation steps previously presented,[28] but including an additional damping term,[31] the fundamental equation of radial hydrophobic particle dynamics can be stated as

$$R\ddot{R} + \tfrac{3}{2}\dot{R}^2 = \frac{1}{\rho}\left[\left(p_0 - p_\mathrm{v} + \frac{2\sigma R_0}{R_0^2 - R_\mathrm{h}^2}\right)\left(\frac{R_0^3 - R_\mathrm{h}^3}{R^3 - R_\mathrm{h}^3}\right)^{\gamma} + p_\mathrm{v} - \frac{2\sigma R}{R^2 - R_\mathrm{h}^2} - \frac{4\eta\dot{R}}{R} - \delta\omega\rho R\dot{R} - p_0 - p(t)\right] , \tag{1}$$

where $p(t)$ is the time-dependent acoustic driving function, $p_0 = 101\,\mathrm{kPa}$ is the ambient pressure, $p_\mathrm{v} = 2.33\,\mathrm{kPa}$ is the vapour pressure, R is the instantaneous bubble radius, R_0 is the initial bubble radius, $R_\mathrm{h} \approx 0.1R_0$ is the incompressible hydrophobic core radius, $\gamma = 1.4$ is the ratio of specific heats, δ is the nonviscous part of the damping coefficient,[31] η is the liquid viscosity, $\rho = 998\,\mathrm{kg\,m^{-3}}$ is the liquid density, $\sigma = 0.072\,\mathrm{N\,m^{-1}}$ is the surface tension, and $\omega = 2\pi \times 10^6\,\mathrm{rad\,s^{-1}}$ is the angular driving frequency. We used a hydrophone recording of a single pulse of five ultrasonic cycles and peak-negative pressure amplitude 1.3 MPa as a driving function. This pulse had been recorded in a separate water container, with a hydrophone positioned along the central axis of the transducer and the hydrophone tip in the acoustic focus. The peak-negative pressure of the pulse was measured to be 1.3 MPa, whilst the peak-positive pressure was measured to surpass 7.4 MPa. As the inertial cavitation threshold is related to the rarefaction of a nucleus, only the peak-negative pressure was taken into account throughout the remainder of this study. It must be noted that (1) only applies until the moment that bubbles undergo surface harmonics or other asymmetries.

Bubble collapse close to an interface may result in a liquid jet protruding from the distal part towards and through the interface.[32] The asymmetric collapse causes the part of the bubble distal to the interface to exceed the velocity of the proximal part to the interface. To conserve the impulse of the system, the liquid distal to the bubble is accelerated and focussed during collapse, leading to the formation of a liquid jet directed to and protruding through the interface.[32] The protrusion may have a destructive effect on biomaterials.[21] The radius of liquid jets has been empirically observed to relate to the collapsing bubble radius:[33]

$$\frac{R_\mathrm{j}}{R_\mathrm{c}} \approx 0.1\,, \tag{2}$$

where R_c is the spherically symmetric pulsating bubble radius on the verge of collapse and R_j is the radius of the liquid jet. In addition, the length of the jet can be estimated from the following empirical relation:[34]

$$\frac{l_\mathrm{j}}{R_\mathrm{c}} \approx 3\,, \tag{3}$$

where l_j is the full travel path of the liquid jet. It should be noted that the full liquid jet is rarely visible, because only the beginning of the protrusion, where gaseous components are drawn into the jet, has an optical refraction index different from the surrounding liquid medium.

Never dried unbleached softwood kraft pulp from a Scandinavian paper mill with a κ number of 85 was washed until a neutral pH was reached. The pulp was stored at 7 °C.

Prior to experiments, polypropylene conical tubes of 15-ml inner volume were filled with

5 ml of reverse-osmosis ultrapure (Type 1) water. To half of the tubes, 5 mg of Zano 10 Plus zinc oxide coated with octyl triethoxy silane (Umicore, Brussel, Belgium) was added. These hydrophobic particles had specified diameters of 50 nm. Although individual particles were too small for visual observation, microbubbles containing clusters of zinc oxide particles were visible. In each tube, 100 mg of wood pulp was deposited, after which the mixture was gently stirred for 1 minute.

An amount of 0.2 ml wood pulp mixture was pipetted into the observation chamber of a high-speed observation system,[23] shown in Fig. 1a. The observation chamber was placed on top of an Eclipse Ti inverted microscope (Nikon Corporation, Minato-ku, Tokyo, Japan) with a Plan Apo 10×/0.45 WD 4.0 objective lens. An HPV-X2 high-speed camera (Shimadzu, Nakagyo-ku, Kyoto, Japan) was connected to the microscope. This camera was operating at a frame rate of ten million frames per second. The exposure time was 50 ns per frame. During camera recording, the material was subjected to one ultrasound pulse.

A laboratory-assembled single-element transducer produced focussed ultrasound pulses.[23] Each pulse had a centre frequency of 1.0 MHz. The voltage amplitude of a pulse was 5.0 V. The signal fed into the transducer was generated by an AFG320 arbitrary function generator (Sony-Tektronix, Shinagawa-ku, Tokyo, Japan) and amplified by a UOD-WB-1000 wide-band power amplifier (TOKIN Corporation, Shiroishi, Miyagi, Japan). The pulse used as a driving function in the simulations had been created with these devices.

A total number of thirteen high-speed video sequences was recorded. Each video sequence consisted of 256 frames. These frames were imported into the matrix laboratory MATLAB® (The Mathworks, Inc., Natick, MA, USA). Nuclei sizes were measured and plotted as a function of time. The modified Rayleigh-Plesset equation (1) was numerically evaluated using the `ode45` differential equation solver of MATLAB® for various liquid viscosities $\eta \in \langle 10^0, 10^2 \rangle$ mPa s. The liquid viscosities used in the simulations included those stated in TAPPI standard 230 om-99. The simulated nucleation curves were superimposed on the measured nucleation plots.

In addition to high-speed photography experiments at 1-MHz sonication, near-audible controls were performed under literature settings, with and without zinc oxide present near wood pulp fibres. These control experiments served to rule out that any deviation with respect to experiments described in literature might be caused by the specific wood pulp sample or by the presence of zinc oxide.

For each near-audible control experiment, a conical tube was clamped such that its base was 12 mm below an FB4417 2-mm microtip (Thermo Fisher Scientific, Waltham, MA, USA)

with measured 1.6-mm diameter that was attached to a CL-334 ultrasound converter (Thermo Fisher Scientific) of an FB705 Sonic Dismembrator (Thermo Fisher Scientific), as shown in Fig. 1b. Each sample was sonicated at a frequency of 20 kHz for 5 min at an operating power of 700 W. The acoustic amplitude of this geometry corresponded to a mechanical index conservatively estimated to be at least twenty times the cavitation threshold. The temperature before and after sonication was measured using a mercury thermometer.

From each sonicated wood pulp mixture, two samples were extracted using tweezers, placed on microscope slides, and preserved with coverslips. Five regions of interest on each slide were optically evaluated using a Leica DMIL LED inverted microscope (Leica Microsystems, Wetzlar, Germany) with an N PLAN 20× (NA 0.40, WD 0.39 mm) objective lens (Leica).

Representative controls in the near-audible frequency range are shown in Fig. 2. The controls demonstrated that under literature conditions, wood pulp fibres were disrupted. Visible disruption was observed both in presence and absence of zinc oxide. Under both conditions, boarded pits had deformed to noncircular geometries. These controls confirmed that the wood pulp sample was behaving similar under high-amplitude low-frequency sonication as described prior in literature. In addition, the presence of zinc oxide was not observed to alter the disruption caused by the near-audible ultrasound.

High-speed footage showed subsequent pulsation cycles of hydrophobic particles. The bubbles surrounding the particles were observed to have expanded to radii beyond 10 μm. Fig. 3a shows a representative example of the radial excursion of hydrophobic zinc oxide near a wood pulp fibre as a response to the pressure pulse shown in Fig. 3b. Numerical solutions of (1) for a bubble of initial radius 2.9 μm with a 10% incompressible core are shown in the same frame. The simulated outward excursions during the first cycles matched those of the experimental data points closest when choosing a liquid viscosity of 45 mPa s. The influence of surface tension or core size on the radial excursions were found to be negligible. Thus, the pulsations of the hydrophobic nuclei in our experiments were dominated by the viscous properties of the wood pulp.

From the fourth pulsation cycle on, radially asymmetric bubble oscillations were observed with a maximum radius of 30 μm. At time stamp 11.2 μs, an asymmetry was observed in the collapsing bubble, which may be interpreted as a jet protruding towards the wood pulp fibre interface, shown in Fig. 3c. The jet radius was estimated to be 2 μm. Following (2), $R_c \approx 20\,\mu$m. According to (3), $l_j \approx 60\,\mu$m, which is well within the fibre. This empirical jet length is an indicator that the wood pulp fibre must have been disrupted following presumed

jet impact. It was noted that the boarded pits visible in the image sequence remained visibly intact in this event and the other experiments at 1 MHz. After the impact of the presumed jet, material was observed to stream near where the jet may have impacted (not shown), indicating successful jet penetration.

In conclusion, our 1-MHz results showed a collapsing bubble near a wood pulp fibre form a liquid jet hitting the fibre, without destruction of the structure, whilst our 20-kHz controls confirmed previously observed structural destruction. This study shows the feasibility of controlled wood fibre deformation at a high ultrasound frequency. To our knowledge, this paper presents the first photographic observation of ultrasound-assisted jet formation near a wood pulp fibre.

Acknowledgements

This work was supported by JSPS KAKENHI, Grant Numbers JP17H00864 and JP20H04542, by the National Research Foundation of South Africa, Grant Number 127102, and by the Academy of Finland, Grant Number 340026.

References

1) K. Nyholm, P. Ander, S. Bardage, and G. Daniel, Nord. Pulp Paper Res. J. **16**, 376 (2001).
2) L. Zhang, A. Larsson, A. Moldin, and U. Edlund, Ind. Crops Prod. **187**, 115432 (2022).
3) T. Aimin, Z. Hongwei, C. Gang, X. Guohui, and L. Wenzhi, Ultrason. Sonochem. **12** 467 (2005).
4) Y. Xu, Y. Yan, X. Yue, Z. Zhu, D. Zhang, and G. Hou, TAPPI J. **13**, 37 (2014).
5) S. Zhou, Y. Li, L. Huang, L. Chen, Y. Ni, and Q. Miao, Cellulose **26**, 9287 (2019).
6) J. Qian, F. Zhao, J. Gao, L. J. Qu, Z. He, and S. Yi, Ultrason. Sonochem. **77**, 105672 (2021).
7) T. Tuziuti and K. Yasui, Ultrason. Sonochem. **88**, 106084 (2022).
8) J. Sostaric and L. K. Weavers, Ultrason. Sonochem. **17**, 1021 (2010).
9) T. Aikawa and N. Kudo, Jpn. J. Appl. Phys. **51**, SDDD13 (2021).
10) T. Moriyama, S. Yoshizawa, and S. Umemura, Jpn. J. Appl. Phys. **51**, 07GF27 (2012).
11) N. Obara, S. Umemura, and S. Yoshizawa, Jpn, J. Appl. Phys. **60**, SDDE04 (2021).
12) H. Dashi, A. Tarmian, M. Faezipour, S. Hedjazi, and M. Shahverdi, BioResources **7**, 1907 (2012).
13) L. B. Feril Jr., T. Kondo, Y. Tabuchi, R. Ogawa, Q.-L. Zhao, T. Nozaki, T. Yoshida, N. Kudo, and K. Tachibana, Jpn. J. Appl. Phys. **46**, 4435 (2007).
14) Y. Yamakoshi, T. Miwa, N. Yoshizawa, H. Inoguchi, and D. Zhang, Jpn. J. Appl. Phys. **49**, 07HF17 (2010).
15) R. Oitate, A. Shimomura, H. Wada, T. Mochizuki, K. Masuda, Y. Oda, R. Suzuki, and K. Murayama, Jpn. J. Appl. Phys. **56**, 07JF25 (2017).
16) R. Oitate, T. Otsuka, M. Seki, A. Furutani, T. Mochizuki, K. Masuda, R. Suzuki, and K. Murayama, Jpn. J. Appl. Phys. **57**, 07LF16 (2018).
17) D. M. Rubin, N. Anderton, C. Smalberger, J. Polliack, M. Nathan, and M. Postema, Fluids **3**, 82 (2018).
18) K. Tachibana and S. Tachibana, Jpn. J. Appl. Phys. **38**, 3014 (1999).
19) H. Yoshikawa, T. Azuma, K. Sasaki, K. Kawabata, and S. Umemura, Jpn. J. Appl. Phys. **45**, 4754 (2006).
20) B. Krasovitski, V. Frenkel, S. Shoham, and E. Kimmel, Proc. Natl Acad. Sci. **108**, 3258 (2011).
21) P. Prentice, A. Cuschieri, K. Dholakia, M. Prausnitz, and P. C. Campbell, Nat. Phys. **1**, 107 (2005).

22) K. Suzuki, R. Iwasaki, R. Takagi, S. Yoshizawa, and S. Umemura, Jpn. J. Appl. Phys. **56**, 07JF27 (2017).
23) N. Kudo, IEEE Trans. Ultrason. Ferroelect. Freq. Control **64**, 273 (2017).
24) N. Okada, M. Shiiba, S. Yamauchi, T. Sato, and S. Takeuchi, Jpn. J. Appl. Phys. **57**, 07LE15 (2018).
25) J. E. Chomas, P. Dayton, D. May, and K. Ferrara, J. Biomed. Opt. **6** 141 (2001).
26) N. Kudo et al., Jpn. J. Appl. Phys. **59**, SKKE02 (2020).
27) M. Postema, R. Matsumoto, R. Shimizu, A. T. Poortinga, and N. Kudo, Jpn. J. Appl. Phys. **59**, SKKD07 (2020).
28) C. S. Carlson, R. Matsumoto, K. Fushino, M. Shinzato, N. Kudo, and M. Postema, Jpn. J. Appl. Phys. **60**, SDDA06 (2021).
29) S. I. Madanshetty and R. E. Apfel, J. Acoust. Soc. Am. **90**, 1508 (1991).
30) T. Tuziuti, K. Yasui, M. Sivakumar, Y. Iida and N. Miyoshi, J. Phys. Chem. A **109**, 4869 (2005).
31) N. Anderton, C. S. Carlson, V. Aharonson, and M. Postema, Curr. Dir. Biomed. Eng. **8**, 781 (2022).
32) A. Philipp and W. Lauterborn, J. Fluid Mech. **361**, 75 (1998).
33) T. Kodama and K. Takayama, Ultrasound Med. Biol. **24**, 723 (1998).
34) C. D. Ohl and E. Ory, Phys. Rev. Lett. **90**, 214502 (2003).

List of Figures

Fig. 1. Experimental high-speed photography setup (a), comprising a 1-MHz single-element focussed ultrasound transducer (i), a water-filled container (ii), an observation chamber (iii), and an objective lens (iv); experimental setup for near-audible controls (b), comprising a microtip (v), a conical tube (vi), a clamp (vii), and a dismembrator (viii).

Fig. 2. Wood pulp fibres before near-audible sonication (a), after 5-min sonication (b); wood pulp fibres mixed with zinc oxide, whose clusters are indicated by dashed green circles, before sonication (c) and after 5-min sonication (d).

Fig. 3. Radial response (a) of a hydrophobic core subjected to a pressure pulse whose peak-negative pressure was 1.3 MPa (– –) and whose peak-positive pressure surpassed 7.4 MPa (b), measured from high-speed video footage of hydrophobically modified zinc oxide (○) and simulated for a bubble of radius $R_0 = 2.9\,\mu$m with a 10% incompressible core in a medium with 45-mPa s viscosity. Inlays extracted from high-speed video footage each correspond to a 100-μm diameter. A zinc oxide cluster is highlighted by a dashed green circle. Selected high-speed footage (c) of an area corresponding to $150 \times 150\,\mu\text{m}^2$ with schematics overlain show a bubble at its maximum (i), its collapse to form a liquid jet (ii), and a composite image of both frames (iii).

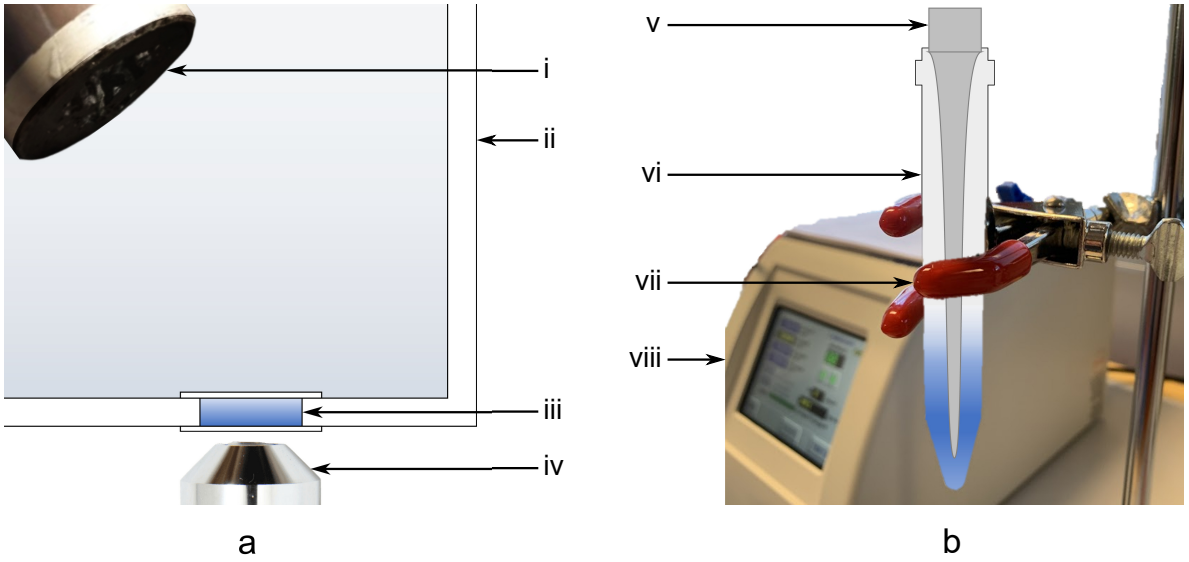

Fig. 1. Experimental high-speed photography setup (a), comprising a 1-MHz single-element focussed ultrasound transducer (i), a water-filled container (ii), an observation chamber (iii), and an objective lens (iv); experimental setup for near-audible controls (b), comprising a microtip (v), a conical tube (vi), a clamp (vii), and a dismembrator (viii).

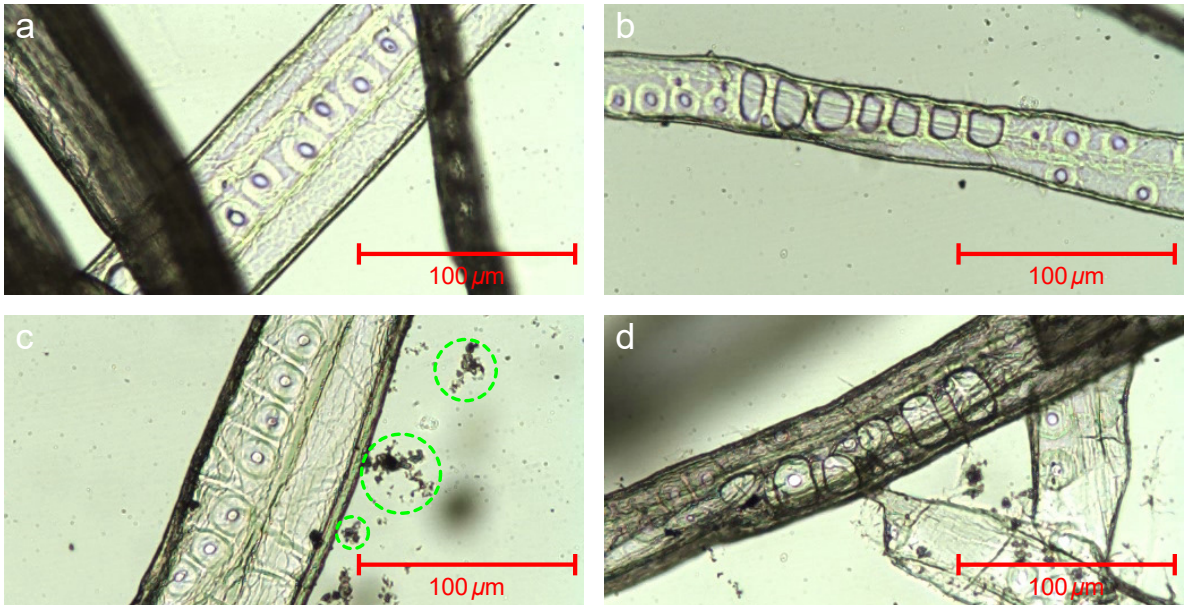

Fig. 2. Wood pulp fibres before near-audible sonication (a), after 5-min sonication (b); wood pulp fibres mixed with zinc oxide, whose clusters are indicated by dashed green circles, before sonication (c) and after 5-min sonication (d).

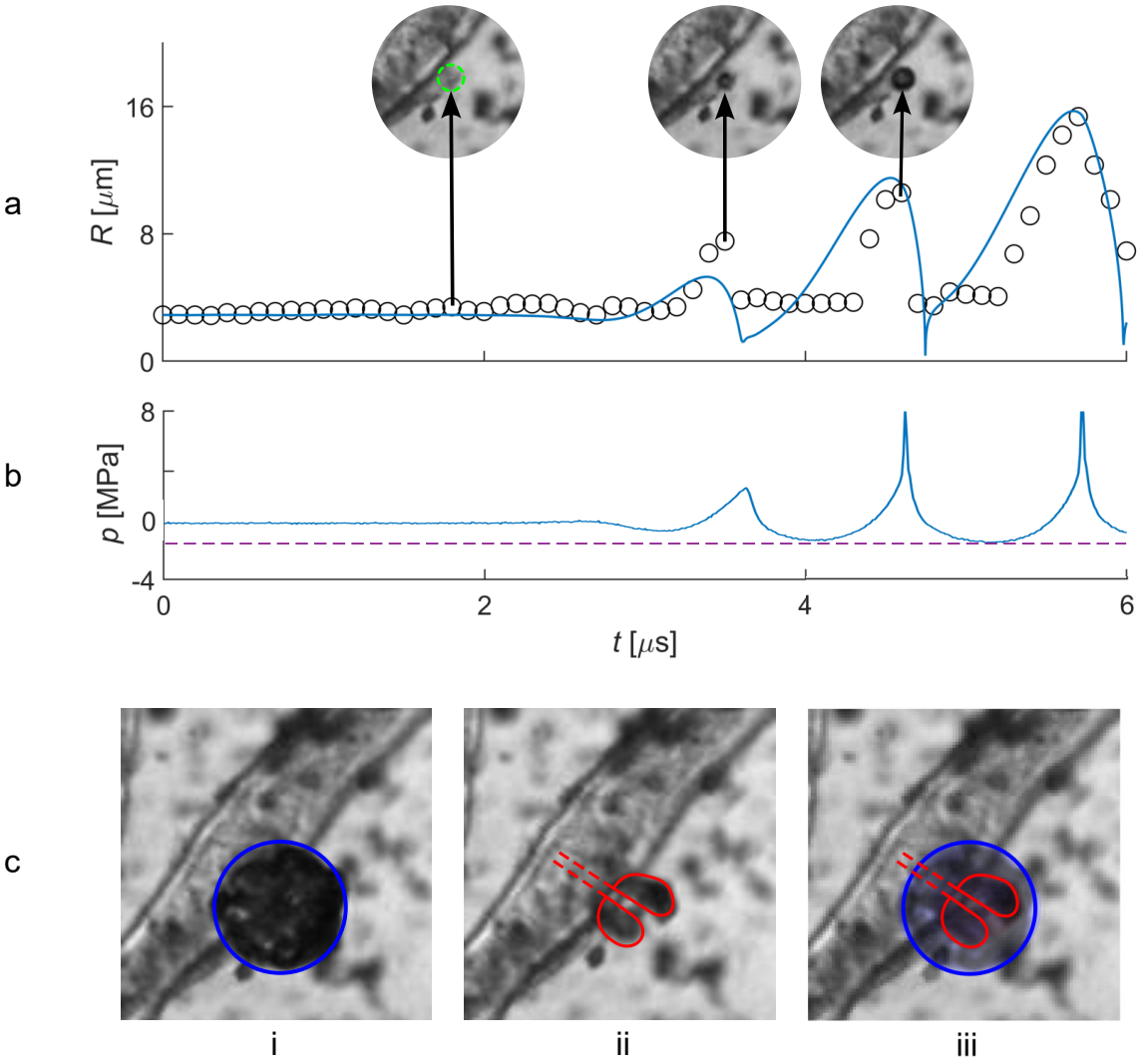

Fig. 3. Radial response (a) of a hydrophobic core subjected to a pressure pulse whose peak-negative pressure was 1.3 MPa (– –) and whose peak-positive pressure surpassed 7.4 MPa (b), measured from high-speed video footage of hydrophobically modified zinc oxide (○) and simulated for a bubble of radius $R_0 = 2.9\,\mu$m with a 10% incompressible core in a medium with 45-mPa s viscosity. Inlays extracted from high-speed video footage each correspond to a 100-μm diameter. A zinc oxide cluster is highlighted by a dashed green circle. Selected high-speed footage (c) of an area corresponding to $150 \times 150\,\mu\text{m}^2$ with schematics overlain show a bubble at its maximum (i), its collapse to form a liquid jet (ii), and a composite image of both frames (iii).